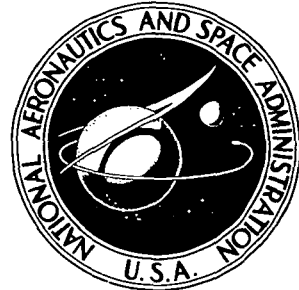


NASA TECHNICAL
MEMORANDUM

NASA TM X-3470



NASA TM X-3470

CASE 71-
COPY

PRESSURE DISTRIBUTIONS INDUCED
BY ELEVON DEFLECTIONS ON
SWEPT WINGS AND ADJACENT
END-PLATE SURFACES AT MACH 6

Louis G. Kaufman II and Charles B. Johnson

*Langley Research Center
Hampton, Va. 23665*

NATIONAL AERONAUTICS AND SPACE ADMINISTRATION • WASHINGTON, D. C. • APRIL 1977

1. Report No. NASA TM X-3470	2. Government Accession No.	3. Recipient's Catalog No.	
4. Title and Subtitle PRESSURE DISTRIBUTIONS INDUCED BY ELEVON DEFLECTIONS ON SWEPT WINGS AND ADJACENT END-PLATE SURFACES AT MACH 6		5. Report Date April 1977	
7. Author(s) Louis G. Kaufman II and Charles B. Johnson		6. Performing Organization Code	
9. Performing Organization Name and Address NASA Langley Research Center Hampton, VA 23665		8. Performing Organization Report No. L-11090	
12. Sponsoring Agency Name and Address National Aeronautics and Space Administration Washington, DC 20546		10. Work Unit No. 505-11-31-02	
15. Supplementary Notes Louis G. Kaufman II: Research Department, Grumman Aerospace Corporation, Bethpage, New York.		11. Contract or Grant No.	
16. Abstract Surface pressure distributions are presented for regions where three-dimensional separated flow effects are prominent on swept-wing-elevon-end-plate models of 0°, 50°, and 70° sweepback, and with 0°, 10°, 20°, and 30° elevon deflections. Surface-oil-flow photographs and pressure distributions on the flat-plate wing, elevon, and end-plate surfaces are presented for numerous geometric variations, including various spacings between the elevon and the end plate, with and without a tip fin. The data, for a free-stream Mach number of 6 and a wing-root-chord Reynolds number of 20×10^6 , reveal considerably larger regions of elevon induced loads on the adjacent end-plate surface than would be anticipated by using inviscid flow analyses.			
17. Key Words (Suggested by Author(s)) Viscid-inviscid interaction Turbulent boundary layer Hypersonic flow Separation	18. Distribution Statement Unclassified - Unlimited	Subject Category 34	
19. Security Classif. (of this report) Unclassified	20. Security Classif. (of this page) Unclassified	21. No. of Pages 122	22. Price* \$5.50

* For sale by the National Technical Information Service, Springfield, Virginia 22161

PRESSURE DISTRIBUTIONS INDUCED BY ELEVON DEFLECTIONS ON SWEPT WINGS

AND ADJACENT END-PLATE SURFACES AT MACH 6

Louis G. Kaufman II* and Charles B. Johnson
Langley Research Center

SUMMARY

Detailed surface pressure distributions are presented for regions where three-dimensional separated flow effects are prominent on a model representative of the fuselage-wing-elevon portions of hypersonic airplanes. The basic configuration model was composed of a sharp-leading-edge flat-plate wing of 0° , 50° , or 70° sweepback with a trailing-edge elevon of 0° , 10° , 20° , or 30° deflection. The model had an attachable outboard tip plate (representative of a tip fin) and an attachable inboard end plate (representative of an aft fin or fuselage section). Surface-oil-flow photographs and pressure distributions on the flat-plate wing, the elevon surface, and the end-plate surface are presented for numerous geometric variations, including various spacings between the elevon and the end plate, for a free-stream Mach number of 6 and a wing-root-chord Reynolds number of 20×10^6 . The data reveal considerably larger regions of elevon induced loads on the adjacent end-plate surface than would be anticipated by using inviscid flow analyses. For comparable flow conditions, the data can guide analyses of wing-sweep, elevon-deflection-angle, tip-plate, and end-plate effects on portions of hypersonic airplanes similar to the wing-elevon model used herein.

INTRODUCTION

Loads on high-speed aircraft surfaces can be altered greatly when shock waves impinge on the boundary-layer flows over these surfaces. Frequently, shock waves cause boundary-layer separation. The resulting surface pressure distributions are far different from those anticipated when shock-wave boundary-layer interaction is neglected. These interactions are well recognized as an important problem area in the design of high-speed aircraft and have prompted many investigations of shock-induced separated flows (refs. 1 and 2). The investigations have resulted in an understanding of some features of two-dimensional separated flows, but there are still many unanswered questions pertaining to three-dimensional flow separation (ref. 3). The problem has eluded theoretical solutions, because of its complexity, but is of great practical importance and has attracted much attention (refs. 1 to 4). An improved understanding of three-dimensional flow separation is needed for the efficient design of high-speed aircraft such as the shuttle, the advanced supersonic transport, and other high-speed vehicles.

The particular problem addressed herein is flow separation caused by elevon deflections on high-speed aircraft. Even small elevon deflections cause

*Research Department, Grumman Aerospace Corporation, Bethpage, New York.

shock waves that can impinge on adjacent fuselage and tip-fin surfaces. The interaction of the shock wave with the boundary layers on these surfaces can result in extensive regions of separated flow and can induce substantial pressure and thermal loads on the surfaces (refs. 3, 5, and 6). These increased loads can compromise an aircraft design. Although these effects are of vital importance to high-speed aircraft design, there are, unfortunately, very few experimental data of general applicability to three-dimensional separated flows, and no satisfactory analytical methods for predicting the interaction effects (refs. 7 to 9).

The character of the boundary layer is one of the most important factors influencing shock-wave boundary-layer interactions (ref. 10). Unfortunately, wind-tunnel models of complete flight configurations usually have laminar or transitional boundary layers whereas the actual flight configurations will have predominately turbulent boundary-layer flows over their surfaces. This discrepancy, caused by size limitations of the model in a hypersonic wind tunnel, makes questionable the validity of extrapolating small-scale model data to full-scale flight vehicles.

An experimental program was designed to augment a much needed base of empirical data applicable to elevon induced separation on high-speed flight vehicles. Instead of using a complete flight configuration, a simple "wing-elevon" model was used to simulate the wing and aft fuselage portion of a typical hypersonic flight configuration. (See fig. 1 and refs. 11 to 14.) The chord of the wing-elevon model could be made several times larger than the wing chord for a model of a complete configuration (for the same wind tunnel). Thus, more detailed data could be obtained in the interaction flow region. Further, chord-length Reynolds numbers comparable to those anticipated for flight vehicles could be achieved; consequently, the character of the boundary layer on the model will be similar to that on the flight vehicle. Fundamental shapes were chosen to insure general applicability of the data and to enhance the usefulness of the data in guiding theoretical analyses. Many geometric parameters were varied to provide data for determining effects of elevon deflection angles, wing sweep, and the presence of tip fins and adjacent fuselage surfaces.

Experiments were conducted in the Langley 20-inch Mach 6 tunnel for root-chord Reynolds numbers of approximately 20×10^6 . Pressure and heating-rate distributions were obtained, as well as oil-flow and schlieren photographic data, for numerous model configurations. Because of the timely need for the data for current systems projects, the pressure data are presented essentially in their entirety in the present paper, with a minimum of analysis and comparison with other pertinent data.

SYMBOLS

g width of gap between end plate and inboard edge of elevon, cm

M Mach number

P ratio of surface pressure to free-stream pressure, p/p_∞

p pressure, Pa

R_c Reynolds number based on free-stream conditions and length (64.14 cm) of wing root chord

T temperature, K

x streamwise distance measured along surface of wing and elevon from wing apex (wing leading edge for unswept wing), cm

y spanwise distance measured outboard from inboard edge of elevon, cm

z distance measured on end plate upward from wing surface, cm

ϵ elevon deflection angle, deg

θ elevon shock-wave angle, deg

Λ wing sweepback angle, deg

Subscripts:

inv value calculated inviscidly, neglecting separation

t stagnation conditions of free-stream tunnel flow

1 local undisturbed flow conditions

2 local flow conditions behind oblique shock wave

∞ free-stream flow conditions

Abbreviations:

HL hinge line

L.E. leading edge

typ typical

EXPERIMENTAL PROGRAM

Model

A "wing-elevon" portion of a typical high-speed flight configuration was used instead of testing a particular, complete, winged flight configuration. This approach has the advantage that, for a given test facility, the wing chord can be several times larger than the corresponding wing chord for a complete winged configuration. Therefore, more detailed data may be obtained in the interaction region. Furthermore, because of the larger wing chord, the root-chord Reynolds number is larger and can be made comparable to the Reynolds

number anticipated for flight configurations. The character of the boundary layer will therefore more closely approximate that anticipated for full-scale flight vehicles. By using fundamental wing-elevon geometries, the data generated are of general applicability and can be used to guide theoretical analyses of interaction flow regions with a minimum of extraneous effects. Outlines of a typical hypersonic flight configuration (refs. 11 to 13) and a wing-elevon model are sketched in figure 1.

Several investigators (e.g., ref. 15) have noted that boundary-layer transition on swept wings with sharp leading edges occurs in a region parallel to the leading edge and that, for zero angle of attack, the flow over the wing is nearly streamwise. Therefore, at an elevon hinge line, the boundary layer may be characteristically turbulent inboard but laminar outboard (ref. 16). Because the character of the boundary layer strongly affects flow separation (ref. 10), wing sweep effects can be an important factor influencing separation ahead of an elevon. In order to investigate these effects, wings having sweep-back angles of 0° , 50° , and 70° were fabricated (fig. 2). The wings had machined sharp leading edges and a partial-span trailing-edge elevon that could be set at a 0° , 10° , 20° , or 30° (flow compression) deflection angle. In order to obtain fundamental data, the elevon was sealed to the wing surface to prevent any air flow between the wing and the elevon.

The model had an attachable end plate to simulate, in fundamental form, an aft fuselage section. (However, the end plate did not have the upstream boundary-layer growth that the flight-vehicle fuselage would have.) Thus, data may be obtained in the absence of end-plate effects, as for the lower wing surface of the flight configuration outlined in figure 1, or with effective inboard end plating, as for the upper wing surface. As indicated in figure 2(b), the model also had an attachable tip plate. When attached to the wing surface, the tip plate was sealed to the elevon to prevent air flow between the tip plate and the elevon.

In order to investigate the effects of air flow between an elevon and aft fuselage section, the end plate is attachable in different spanwise positions on the wings. The resulting gaps between the elevon and end plate can be varied from zero (end plate sealed to elevon) to 1.27 cm (fig. 2). A photograph of the unswept wing with a 30° elevon and with the end plate and tip plate attached and sealed to the elevon is shown in figure 3.

As indicated in figure 4, the wing, elevon, and end-plate surfaces have dense rectangular arrays of pressure taps in the anticipated interaction flow region. Five separate tunnel runs were required to measure and record pressures at all of the pressure orifice locations shown in figure 4. For many model configurations, the pressures were measured and recorded at only selected pressure tap locations.

Test Conditions

The experiments were conducted in the Langley 20-inch Mach 6 tunnel. This is a blowdown wind tunnel with an approximately 50.8-cm square test section (refs. 17 and 18). The tunnel has a model injection system in a vacuum tight

chamber directly beneath the test section. A photograph of the tunnel test section is shown in figure 5. The model, strut mounted to the injection system beneath the tunnel test section, is visible in the photograph.

In order to obtain as large a Reynolds number as possible, and the most accurate pressure data, the tunnel was operated near its maximum stagnation pressure operating conditions for all of the subject test runs. Nominal values of the stagnation pressure p_t and temperature T_t are shown in table I, along with the free-stream Mach number M_∞ and the free-stream Reynolds number R_c , based on the model root-chord length of 64.14 cm. Inboard, the boundary layer is turbulent well upstream of the hinge line; however, the boundary-layer character may well be transitional near the hinge line on the outboard portion of the 70° swept wing. The types of data presented in this paper for various model configurations are indicated in table II. No schlieren photographs were taken with the end plate attached to the model. Unless otherwise indicated in table II for the configuration with the end plate attached to the model, data were obtained only for a zero gap width (end plate sealed to elevon).

Test Procedures and Data Reduction

For each tunnel run, the tunnel flow was first started and established. The model was then injected into the tunnel flow, and selected pressure orifices were monitored on strip-type recorders. When the monitored pressures had stabilized, the pressure data were recorded on an analog-digital system. Up to 19 pressures were recorded at one time, while the remaining pressure tubes were pinched closed. The first bank of pressure tubes was then pinched closed, and a second bank of 19 pressures was recorded. Nineteen transducers and 3 pinch bars allow recording up to 57 pressures during any one tunnel run. The tunnel total temperature, total pressure, and model wall temperature remained essentially invariant from one bank of pressure tube recordings to the next during any one tunnel run. After all the pressure data were recorded, the model was ejected from the tunnel flow. Schlieren flow photographs were taken for selected configurations while the pressure data were being measured. As described in the following section, a repeat run was made for a selected configuration (30° elevon on unswept wing with end plate attached); and the repeatability of the measured pressures was found to be excellent.

The oil-flow technique was used to ascertain the location of separation and reattachment on the wing, elevon, and end-plate surfaces. The same model was used, but the inserts with the pressure orifices were replaced with silicone rubber inserts. The resulting model wall temperature was negligibly different. The model surfaces were prerubbed with silicone oil (Dow Corning® 550 fluid). A random pattern of varying size oil drops was then splattered on the model surfaces by using a mixture of 10 ml of the same oil, 10 ml of titanium dioxide, and 1 ml of oleic acid. The tunnel flow was started, and the model was injected into the established tunnel flow. The oil flow was observed (with TV camera), and top and side motion pictures (10 frames per second) of the oil flow were obtained during the tunnel run. Once the oil-flow pattern was firmly established and there was no further apparent oil droplet movement, the model was ejected from the tunnel flow and then the tunnel flow was stopped. Next, still photographs of the model were taken. The length of

separated flow ahead of the elevon (as indicated by the oil accumulation line, ref. 16) was measured directly on the wing surface, and the apparent location of reattachment was measured directly on the elevon surface after each oil-flow tunnel run. Prior to each oil-flow tunnel run, a rectangular grid was placed on the model, and the model was photographed in the test section with motion-picture cameras. The grid served as a reference for scaling the oil-flow motion-picture frames.

Profile schlieren flow photographs were taken when neither the end plate nor the tip plate was attached to the model (table II). Finally, strip recorders were used to record the tunnel-flow total pressure and total temperature during each tunnel run.

PRESENTATION OF RESULTS

The experimental results are presented for the unswept wing in figures 6 to 45, for the 50° swept wing in figures 46 to 60, and for the 70° swept wing in figures 61 to 105. For each wing, data are presented for undeflected elevon configurations, and for configurations with 10°, 20°, and 30° elevon deflection. For each elevon deflection, data on the wing and elevon surfaces (including profile schlieren flow photographs) are presented before data for the end-plate surface.

Pressures measured on the model surfaces are nondimensionalized by using the free-stream static pressure (calculated from p_t and the calibrated tunnel Mach number of 6 for the subject-test total pressure) for each tunnel run. The resulting ratios $P = p/p_\infty$ are insensitive to minor variations in the tunnel-flow free-stream pressure from run to run. Pressure ratios on the wing, elevon, and end-plate surfaces are listed adjacent to their pressure tap locations in carpet plots (e.g., fig. 8) for nearly all model configurations. For selected configurations (e.g., fig. 10), streamwise distributions of the pressure ratios are plotted in addition to the carpet plots. In both types of plots, x is the surface streamwise distance; a true view of the elevon surface is depicted in the carpet plots instead of the projection of the tap locations in the plane of the wing.

The hinge-line location and inviscid-flow value of the pressure ratio on the elevon surface are indicated (e.g., fig. 10) in the streamwise plots of the pressure ratios. The inviscid-flow value of pressure ratio is calculated in the following manner. The average measured pressure ratio on the wing surface for no elevon deflection (p_1/p_∞) and a free-stream Mach number of 6 are used in oblique-shock relations (ref. 19) to obtain M_1 , the Mach number of the undisturbed flow over the wing surface. This Mach number and the elevon deflection angle are used in oblique-shock relations to obtain the pressure rise (p_2/p_1) on the elevon surface. This pressure rise is multiplied by the pressure ratio of the undisturbed flow on the wing surface to yield the inviscid-flow value of the pressure ratio on the elevon surface ($P = p_2/p_\infty$).

On the end-plate surface, the elevon location is indicated by a solid line (e.g., fig. 14) when the elevon is sealed to the end plate and by a dashed line (e.g., fig. 41) when there is a gap between the elevon and the end plate. The

location of the inviscid-flow shock wave generated by the elevon is indicated by a dotted line (e.g., fig. 14) on the end-plate surface.

Profile schlieren flow photographs showing the aft portion of the model are presented for model configurations having neither the end plate nor the tip plate attached. The elevon hinge-line location is indicated by HL (e.g., fig. 7) when there is no elevon deflection.

Frames from profile and planform surface-oil-flow motion pictures are presented for selected configurations. Flow-separation line locations on the model surfaces are indicated by oil accumulation lines in these photographs (e.g., fig. 15).

DISCUSSION OF EXPERIMENTAL RESULTS

Wing and Elevon Surfaces

Elevon deflection angle of 0°.— Pressure ratios on the wing and elevon surfaces for $\epsilon = 0^\circ$ vary randomly about the value 1.08 for both the unswept and 50° swept wings; the ratios are slightly less ($P = 1.05$) for the 70° swept wing. In all cases, the variation in P about the mean value is approximately 0.04. Considering all cases, there is no consistent spanwise or streamwise trend in the values, and the pressure ratios are unaffected by attaching the end plate to the wing (compare, e.g., fig. 6 with fig. 8 and fig. 61 with fig. 63). The apparent boundary-layer thicknesses at the hinge location, scaled from schlieren flow photographs, are 0.79 cm for $\Lambda = 0^\circ$, 0.78 cm for $\Lambda = 50^\circ$, and 0.77 cm for $\Lambda = 70^\circ$ (e.g., figs. 7 and 62). Surface-oil-flow motion pictures indicate purely streamwise flow. No corner-flow or edge-flow effects are noticeable in the instrumented region of the model with or without the end plate and/or tip plate attached to the wing.

Elevon deflection angle of 10° .— Surface-oil-flow and schlieren flow photographs give no indication of any flow separation from the wing surfaces ahead of the 10° elevons (e.g., figs. 12 and 67). For all three wings, the profile schlieren flow photographs indicate shock waves emanating from the elevon hinge lines; boundary-layer thicknesses at the hinge-line location are unaffected by the 10° elevons. The pressures on the unswept wing surface, including those adjacent to the hinge line, are unaffected by a 10° elevon deflection (fig. 11). However, for the most highly swept wing ($\Lambda = 70^\circ$), the pressures start to rise (most notably outboard) at the tap locations on the wing adjacent to the hinge line (fig. 66).

The pressure ratios on the elevon surfaces rise to values approaching the inviscid values $P_{inv} = 3.96$ for $\Lambda = 0^\circ$ and 50° and $P_{inv} = 3.81$ for $\Lambda = 70^\circ$. (P_{inv} is calculated by using the experimental p_1/p_∞ and the calculated M_1 just upstream of the hinge line.) The measured pressures attain their maximum values, which are approximately 5 percent less than the values calculated for inviscid flow, at approximately the midchord location of the elevon. For the 70° swept wing, the pressure rise is steepest along the farthest outboard line of pressure taps. For the unswept

wing, there is a small spanwise dropoff in the pressure on the elevon surface near the trailing edge (fig. 11).

Attaching the end plate does not affect the pressure ratios on the wing and 10° elevon surfaces (e.g., figs. 13 and 68). Examination of planform surface-oil-flow motion pictures for all three wings reveals purely streamwise flow with no flow separation when the end plate is attached, with or without the tip plate attached.

Elevon deflection angle of 20°.- Planform surface-oil-flow motion pictures give no evidence of separation ahead of the 20° elevons for any of the three wings. However, for the 70° swept wing, there is some evidence of a small region of reduced shear force on the elevon surface immediately downstream of the hinge line. Profile schlieren flow photographs for 20° elevons are similar whether the wing is unswept (fig. 18) or swept 50° or 70° (figs. 49 and 73). The schlieren photographs indicate shock waves emanating from within the boundary-layer flow over the wing surfaces just upstream of the 20° elevons, but the schlieren photographs do not indicate any region of separated flow upstream of the elevon hinge lines. The boundary-layer thicknesses at the hinge-line location remain unaffected by the 20° elevons.

Pressure ratios on the wing surfaces are unaffected by the 20° elevons except for the tap locations adjacent to the hinge lines; at these locations the pressure ratios are approximately 10 percent larger than the undisturbed-pressure-ratio values (figs. 17, 48, and 72). The pressure ratios on the elevon surfaces increase to values approximately equal to the inviscid values $P_{inv} = 9.81$ for $\Lambda = 0^\circ$ and 50° and $P_{inv} = 9.61$ for $\Lambda = 70^\circ$ (P_{inv} is again calculated by using p_1/p_∞ and M_1); the measured pressures attain these values at approximately the 40-percent elevon chord location (e.g., figs. 16, 47, and 71). For the 70° wing, the pressure rise is steepest along the farthest outboard line of pressure taps (fig. 72). For the 50° wing, the pressure rise is somewhat steeper along the farthest outboard line of taps (fig. 50). For all three wings, there is a small spanwise dropoff in pressure on the elevon surface near the trailing edge (figs. 17, 48, and 72).

Pressures on the 20° elevon surfaces are increased slightly when the end plate is attached to the wings and, as expected, the end plate prevents the inboard spanwise dropoff in pressure near the elevon trailing edge (figs. 19, 50, and 74). The outboard spanwise dropoff in pressure on the elevon surface is prevented when the tip plate is attached to the unswept wing (fig. 20). Attaching the tip plate to the 70° wing results in increased pressures along the farthest outboard line of pressure taps (figs. 74 and 75). Leaving a gap between the elevon and the end plate on the 70° wing does not affect substantially the pressure ratios on the wing and elevon surfaces (figs. 75 and 76). Planform surface-oil-flow motion pictures do not indicate any significant regions of separated flow on the wing and elevon surfaces when the end plate is attached to the wings, with or without the tip plate attached.

Elevon deflection angle of 30°.- Streamwise distributions of pressure ratios on the wing and 30° elevon surfaces resemble those typical of turbulent boundary-layer separation ahead of ramps (ref. 10). The pressures start to rise approximately 2 cm upstream of the hinge lines, there are knees in the

pressure-ratio distributions at the hinge-line locations, and then the pressure ratios continue to increase to values somewhat larger than those calculated for the inviscid flows $P_{inv} = 18.76$ for $\Lambda = 0^\circ$ and 50° and $P_{inv} = 18.34$ for $\Lambda = 70^\circ$ (P_{inv} is once more calculated by using p_1/p_∞ and M_1). The pressure ratios attain their maximum values around the 30-percent elevon chord location and then decay towards the inviscid values (figs. 24, 53, and 81). Profile schlieren flow photographs are similar for the three wings (figs. 26, 55, and 84). The photographs indicate regions of separated flow with shock waves emanating within the boundary-layer flows over the wing surfaces at locations approximately 2 cm upstream of the elevon hinge lines. Just upstream of the hinge lines, however, the apparent boundary-layer thicknesses based on schlieren photographs (fig. 26) are essentially the same as those for the wings with no elevon deflection. In the photographs, there is an apparent necking down of the viscous flow over the elevon surface in the region where the flow reattaches. The pressure ratios attain their largest values near this region (figs. 24, 26, 53, 55, 81, and 84).

Examination of planform surface-oil-flow motion pictures reveals a steady location of the oil accumulation lines ahead of the 30° elevons. These lines, apparent in the motion-picture frames shown in figures 27, 56, and 83, indicate the location of flow separation ahead of the elevons. Separation lengths, scaled from the surface-oil-flow motion pictures, agree with those obtained from the schlieren flow photographs and streamwise pressure-ratio distributions. The apparent locations of separation and reattachment, obtained by scaling the oil-flow pictures, agree well with those measured directly on the model surface immediately after each surface-oil-flow tunnel run.

The carpet plot of pressure ratios on the unswept wing indicates a reduced extent of separation along the inboard and outboard lines of pressure taps. This is corroborated by the corresponding surface-oil-flow photograph (figs. 25 and 27). For the 50° and 70° swept wings, the extent of separation is reduced along the outboard lines of pressure taps (figs. 54, 56, 82, and 83). The pressure rise is particularly steep along the farthest outboard line of pressure taps on the 70° swept wing. The steep pressure rise and reduced extent of separation can be attributed to the boundary layer being thinner on the outboard portion of the wing surface than on the inboard portion.

With either the tip plate or end plate attached, the pressures in the separated flow region ahead of the elevon are generally increased, except at the tap locations farthest away from the added plate. Considering the streamwise pressure gradient over the separated-flow region, this is probably indicative of a somewhat larger region of separated flow near the attached plate, rather than an increased pressure level throughout the entire separated-flow region. The attached plate prevents venting of the vortical separated flow and thus results in a greater extent of separated flow on the side adjacent to the attached plate (figs. 27, 31, 32, 56, 58, 83, and 86). Because of the thinness of the boundary layer on the outboard portion of the 70° swept wing, the effect of the tip plate in increasing the extent of separation is minimal for the 70° wing (figs. 86 and 91).

On the 30° elevon surface, with no plates attached to the model, there is a spanwise decrease in pressure near the elevon trailing edge. The magnitude

of the spanwise decrease in P is diminished when the tip plate and/or the end plate are/is attached to the model. These plates prevent some of the pressure loss on the elevon surface at the locations closest to the attached plate (figs. 25, 28, 29, 30, 54, 57, 82, 85, and 90). The 30° elevon aspect ratio is sufficiently large so that, for these test conditions, the tip-plate and end-plate effects are independent of one another.

The effects of gaps between the elevon and the end plate on the distributions of pressure ratios on the wing and elevon surfaces can be gleaned by examining figures 33 to 36 (cf. fig. 29) and figures 92 to 95 (cf. fig. 90). As expected, increasing the gap size slightly relieves the pressure on the inboard portion of the elevon surface. Surface-oil-flow photographs indicate a small decrease in the inboard extent of separation for the larger gap sizes (a 10-percent decrease for the largest gap size). (A repeat tunnel run, made for the configuration with the largest gap between the elevon and end plate (fig. 36), revealed that the pressure ratio values repeated within 0.5 percent, an indication of the repeatability of the pressure-ratio data.)

End-Plate Surface

Pressures measured on the end-plate surface were used in obtaining carpet plots of pressure ratios P over the surface. Profile surface-oil-flow motion pictures were reviewed to ascertain regions of disturbed flow on the end-plate surface. For all tunnel runs, once the surface-oil-flow pattern becomes established, it does not vary during the remainder of the run. Locations of oil accumulation lines are very steady throughout each tunnel run.

Pressure ratios on the end-plate surface for undisturbed flows (no elevon deflections) vary slightly about the values $P = 1.06$ for $\Lambda = 0^\circ$, $P = 1.09$ for $\Lambda = 50^\circ$, and $P = 1.10$ for $\Lambda = 70^\circ$ (e.g., figs. 9 and 64). Profile surface-oil-flow motion pictures, both with and without the outboard tip plate attached, indicate purely streamwise flow on the end plate. No corner-flow, edge-flow, or tip-plate effects are noticeable in the region of instrumentation for any wing sweepback angle.

For all elevon deflections, neither wing sweepback nor the addition of the outboard tip plate noticeably affects either the extent or magnitude of the elevon induced pressures on the end-plate surface. The surface-oil-flow patterns on the end-plate surface are unaffected by wing sweepback, whether or not the tip plate is attached to the model.

Elevon effects. - Pressures induced on the end-plate surface by elevons on the adjacent wing surface attain maximum values near where the elevon surface joins the end plate (e.g., figs. 14, 51, and 100). For the 10° and 20° elevons, the pressure ratios induced on the end-plate surface remain less than those attained on the elevon surface. However, the 30° elevon induces some pressure ratios on the end-plate surface that exceed those on the elevon surface itself (e.g., figs. 37, 59, and 96). This may be the result of a complex, multiple shock system near the end-plate surface.

The regions of increased pressures on the end-plate surface, induced by the elevons on the adjacent wing, are much more extensive than would be anticipated by using inviscid flow analyses. Without the end plate, the elevon shock-wave angles measured on the profile schlieren flow photographs agree well with the shock-wave angles θ calculated for inviscid flows $\theta = 18^\circ$, 28° , and 41° for $\epsilon = 10^\circ$, 20° , and 30° . The loci of these shock waves are indicated by dotted lines on the carpet plots of the pressure ratios on the end-plate surface. The elevon induced pressures on the end-plate surface increase over the undisturbed values far ahead of these shock-wave locations (e.g., figs. 21, 22, 59, and 69).

The regions of increased pressure on the end-plate surface are delineated quite accurately by the oil accumulation lines evident in profile surface-oil-flow motion pictures (e.g., figs. 40, 46, and 79). The oil accumulation lines on the end plate form angles, with respect to the free-stream direction, of 31° , 47° , and 58° for $\epsilon = 10^\circ$, 20° , and 30° . The oil accumulation lines for $\epsilon = 30^\circ$ emanate from locations approximately 2 cm upstream of the 30° elevon hinge line (e.g., figs. 39, 60, and 97). When superimposed on the end-plate pressure-ratio carpet plots (dot-dash lines in figs. 14, 22, 37, 38, 42, 51, 59, 78, 96, 98, and 100), the locations of the oil accumulation lines accurately bound the regions of increased pressure. Downstream of the oil accumulation lines, the oil flow on the end plate parallels the oil accumulation lines, not the elevon surface (as might be expected using inviscid-flow analyses).

Gap effects.— Whenever an elevon is not sealed to the end plate, pressures on the shaded region of the end-plate surface (in the gap between the elevon and end plate) are measured and recorded. The locus of where the elevon surface, if extended, would intersect the end plate is shown as a dashed line on the carpet plots of the pressure ratios on the end-plate surface (e.g., figs. 42, 80, and 103). The pressures measured on the end plate in the region shaded by the elevon are greatest near the upstream boundary of the region (dashed line).

The overpressures induced by the elevon on the end-plate surface upstream of the shaded region diminish with increasing gap size (figs. 41 to 44 and 102 to 105). Also, as expected, the extent of the region of increased pressures upstream of the elevon diminishes with increasing gap size.

The decreased extent of the region of increased pressures on the end-plate surface ahead of the elevon is evidenced also by the oil accumulation lines apparent in frames from profile surface-oil-flow motion pictures (figs. 39, 45, 97, and 99). Also evident in the surface-oil-flow photographs is the concave shape of the oil accumulation lines when there are gaps, as opposed to the straight-line shapes when the elevon is sealed to the end plate. Even for substantial gap sizes, there apparently remains much upward flow on the end-plate surface in a direction more nearly aligned with the oil accumulation line than with the elevon surface (fig. 45).

CONCLUDING REMARKS

Data are presented on basic flat-plate configurations for which there are important three-dimensional separated flow effects that are not predictable with current theoretical methods. The configurations are representative of the fuselage-wing-elevon portions of hypersonic aircraft. The data, obtained for Mach 6 flows and a wing-root-chord Reynolds number of approximately 20×10^6 , can be used to guide analyses of flap or elevon induced loads on adjacent surfaces of hypersonic aircraft for similar geometries and flow conditions.

For the subject range of test conditions, the pressure on the forward portion of the elevon is considerably less than the value calculated by using inviscid flow theory. The tip plate and end plate prevent the spanwise dropoff in pressure on the aft portion of the elevon. The region of increased pressure on the end plate, induced by the deflected elevon, is considerably larger than that indicated using inviscid-flow elevon shock-wave angles. The surface flow on this region of the end plate parallels the oil accumulation line (which indicates the extent of the region of increased pressure), and not the deflected elevon surface direction.

Wing sweepback had negligible effect on the surface pressure distributions except for the farthest outboard line of pressure taps on the 70° swept wing. The effective aspect ratio of the elevon, for a 30° deflection, is sufficiently large so that tip-plate and end-plate effects are mutually independent. Increasing the gap size between the end plate and the elevon diminishes the extent of the region of increased pressures on the end-plate surface and diminishes the effectiveness of the end plate in preventing spanwise flow on the wing and elevon surfaces.

Langley Research Center
National Aeronautics and Space Administration
Hampton, VA 23665
February 2, 1977

REFERENCES

1. Korkegi, R. H.: Survey of Viscous Interactions Associated With High Mach Number Flight. AIAA J., vol. 9, no. 5, May 1971, pp. 771-784.
2. Ryan, B. M.: Summary of the Aerothermodynamic Interference Literature. Tech. Note 4061-160, Naval Weapons Center (China Lake, Calif.), Apr. 1969.
3. Goldberg, Theodore J.: Three-Dimensional Separation for Interaction of Shock Waves With Turbulent Boundary Layers. AIAA J., vol. 11, no. 11, Nov. 1973, pp. 1573-1575.
4. Sedney, Raymond; and Kitchens, Clarence W., Jr.: The Structure of Three-Dimensional Separated Flows in Obstacle, Boundary-Layer Interactions. Flow Separation, AGARD-CP-168, Nov. 1975, pp. 37-1 - 37-15.
5. Korkegi, R. H.: Comparison of Shock-Induced Two- and Three-Dimensional Incipient Turbulent Separation. AIAA J., vol. 13, no. 4, Apr. 1975, pp. 534-535.
6. McCabe, A.: The Three-Dimensional Interaction of a Shock Wave With a Turbulent Boundary Layer. Aeronaut. Q., vol. XVII, pt. 3, Aug. 1966, pp. 231-252.
7. Peake, David J.; Rainbird, William J.; and Atraghji, Edward G.: Three-Dimensional Flow Separations on Aircraft and Missiles. AIAA J., vol. 10, no. 5, May 1972, pp. 567-580.
8. Whitehead, Allen H., Jr.; Sterrett, James R.; and Emery, James C.: Effects of Transverse Outflow From a Hypersonic Separated Region. AIAA J., vol. 10, no. 4, Apr. 1972, pp. 553-555.
9. Small, William J.; Kirkham, Frank S.; and Fetterman, David E.: Aerodynamic Characteristics of a Hypersonic Transport Configuration at Mach 6.86. NASA TN D-5885, 1970.
10. Chapman, Dean R.; Kuehn, Donald M.; and Larson, Howard K.: Investigation of Separated Flows in Supersonic and Subsonic Streams With Emphasis on the Effect of Transition. NACA Rep. 1356, 1958.
11. Hypersonic Aircraft by 2000 Pushed. Aviat. Week & Space Technol., vol. 99, no. 12, Sept. 17, 1973, pp. 52-57.
12. Clark, Louis E.; and Richie, Christine B.: Aerodynamic Characteristics at Mach 6 of a Hypersonic Research Airplane Concept Having a 70° Swept Delta Wing. NASA TM X-3475, 1977.
13. Creel, Theodore R., Jr.; and Penland, Jim A.: Low-Speed Aerodynamic Characteristics of a Hypersonic Research Airplane Concept Having a 70° Swept Delta Wing. NASA TM X-71974, 1974.

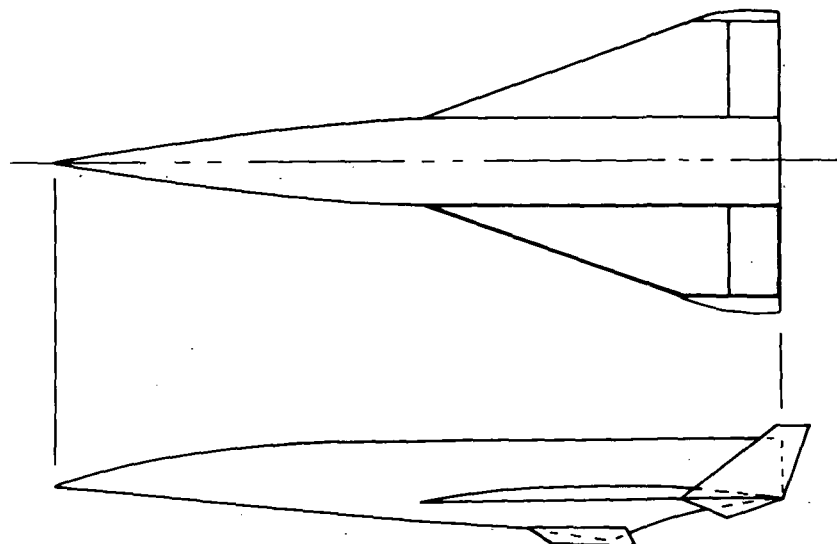
14. Nagel, A. L.; and Becker, J. V.: Key Technology for Airbreathing Hypersonic Aircraft. AIAA Paper No. 73-58, Jan. 1973.
15. Whitehead, Allen H., Jr.; and Keyes, J. Wayne: Flow Phenomena and Separation Over Delta Wings With Trailing-Edge Flaps at Mach 6. AIAA J., vol. 6, no. 12, Dec. 1968, pp. 2380-2387.
16. Kaufman, Louis G., II; and Freeman, L. Michael: Separation Ahead of Controls on Swept Wings. ARL TR 75-0134, U.S. Air Force, June 1975.
17. Sterrett, James R.; and Emery, James C.: Extension of Boundary-Layer-Separation Criteria to a Mach Number of 6.5 by Utilizing Flat Plates With Forward-Facing Steps. NASA TN D-618, 1960.
18. Schaefer, William T., Jr.: Characteristics of Major Active Wind Tunnels at the Langley Research Center. NASA TM X-1130, 1965.
19. Ames Research Staff: Equations, Tables, and Charts for Compressible Flow. NACA Rep. 1135, 1953.

TABLE I.- TUNNEL FLOW CONDITIONS

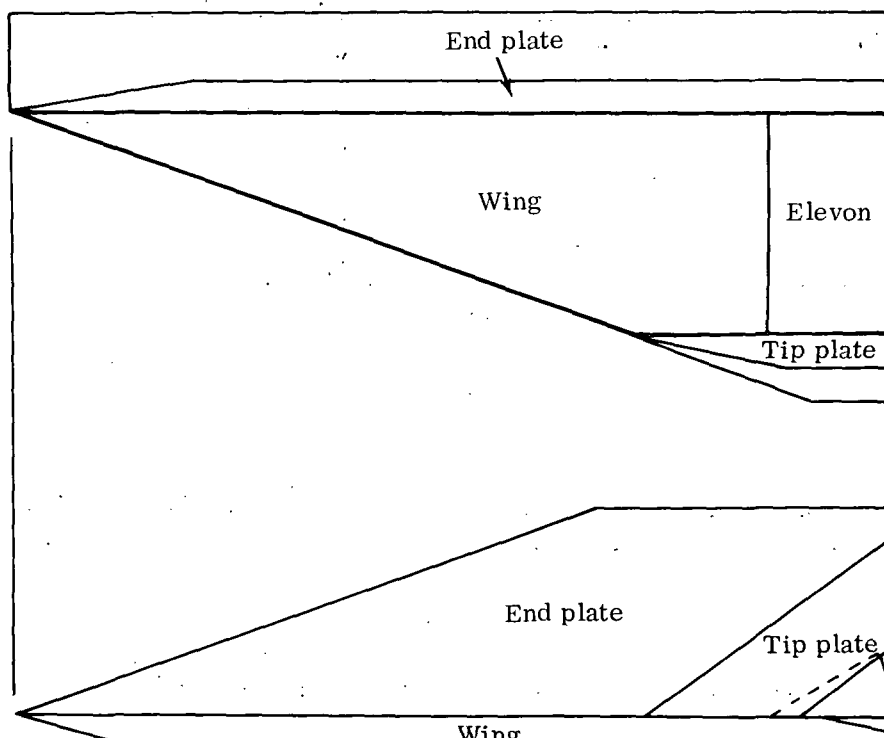
Stagnation pressure, p_t , MPa (psia)	3.56 (516)
Free-stream pressure, p_∞ , kPa (psia)	2.26 (0.327)
Stagnation temperature, T_t , K ($^{\circ}$ R)	498 (896)
Free-stream Mach number, M_∞	6
Reynolds number, R_C	19.54×10^6

TABLE II.- TYPES OF DATA PRESENTED FOR VARIOUS MODEL CONFIGURATIONS

Λ , deg	ϵ , deg	Type of data	Figure
End plate off and tip plate off			
0	0	Pressure distribution; schlieren photograph	6; 7
10	0	Pressure distribution; schlieren photograph	10, 11; 12
20	0	Pressure distribution; schlieren photograph	16, 17; 18
30	0	Pressure distribution; oil-flow photograph; schlieren photograph	24, 25; 27; 26
50	20	Pressure distribution; schlieren photograph	47, 48; 49
50	30	Pressure distribution; oil-flow photograph; schlieren photograph	53, 54; 56; 55
70	0	Pressure distribution; schlieren photograph	61; 62
10	0	Pressure distribution; schlieren photograph	65, 66; 67
20	0	Pressure distribution; schlieren photograph	71, 72; 73
30	0	Pressure distribution; oil-flow photograph; schlieren photograph	81, 82; 83; 84
End plate off and tip plate attached			
0	30	Pressure distribution	28
End plate attached and tip plate off			
0	0	Pressure distribution	8, 9
10	0	Pressure distribution; oil-flow photograph	13, 14; 15
20	0	Pressure distribution	19, 21
30	0	Pressure distribution; oil-flow photograph; gap spacing	29, 37; 31, 39, 45; 33 to 36, 41 to 45
50	10	Oil-flow photograph	46
20	0	Pressure distribution; oil-flow photograph	50, 51; 52
30	0	Pressure distribution; oil-flow photograph	57, 59; 58, 60
70	0	Pressure distribution	63, 64
10	0	Pressure distribution	68, 69
20	0	Pressure distribution; oil-flow photograph; gap spacing	74, 77
30	0	Pressure distribution; oil-flow photograph; gap spacing	85, 96; 86, 88, 97, 99; 87, 88, 98, 99
End plate attached and tip plate attached			
0	20	Pressure distribution; oil-flow photograph	20, 22; 23
0	30	Pressure distribution; oil-flow photograph	30, 38; 32, 40
70	10	Oil-flow photograph	70
20	0	Pressure distribution; oil-flow photograph; gap spacing	75, 78; 79; 76, 80
30	0	Pressure distribution; oil-flow photograph; gap spacing	89, 90, 100; 91, 101; 92 to 95, 101 to 105

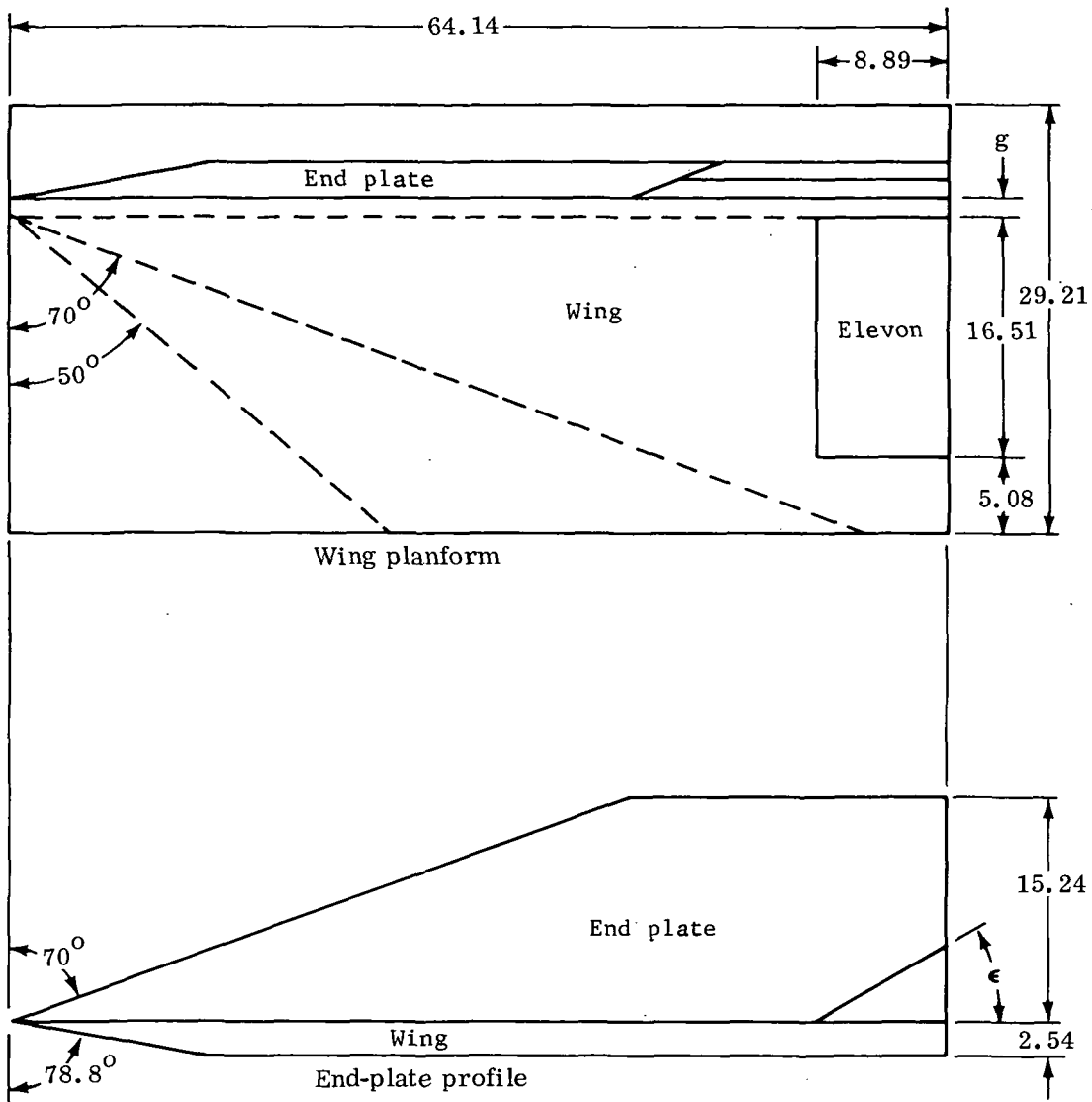


Hypersonic research airplane



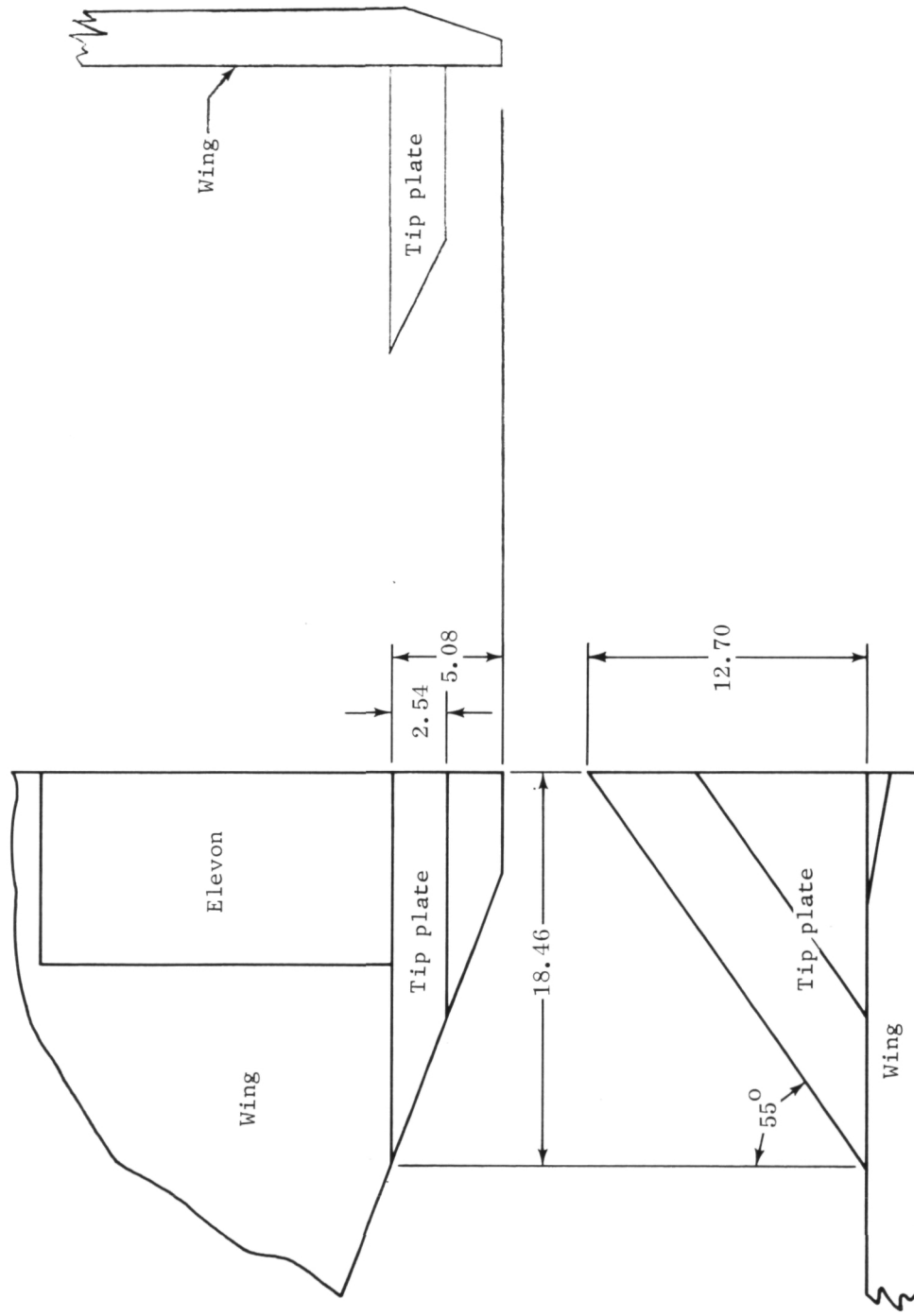
Wing-elevon model

Figure 1.- Outlines of typical hypersonic research airplane
and wing-elevon model.



(a) Wing planform ($g = 0, 0.32, 0.64, 0.95$, or 1.27) and end-plate profile ($\epsilon = 0^\circ, 10^\circ, 20^\circ$, or 30°).

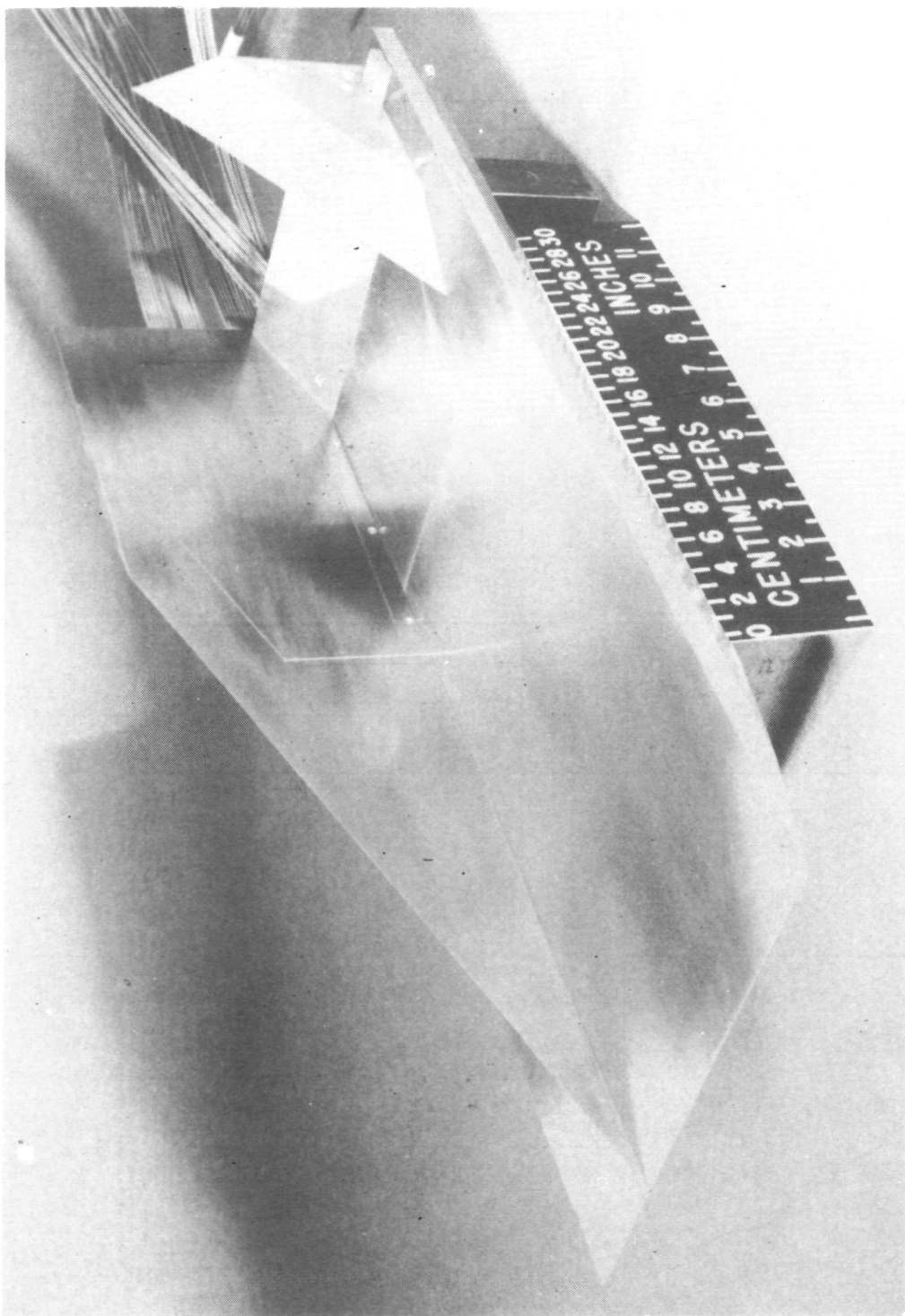
Figure 2.-- Sketch of wing-elevon model; linear dimensions in cm.



(b) Tip-plate geometry.

Figure 2.- Concluded.

L-77-108
Figure 3.- Photograph of unswept wing with elevon deflected 30° and with
end plate and tip plate attached.



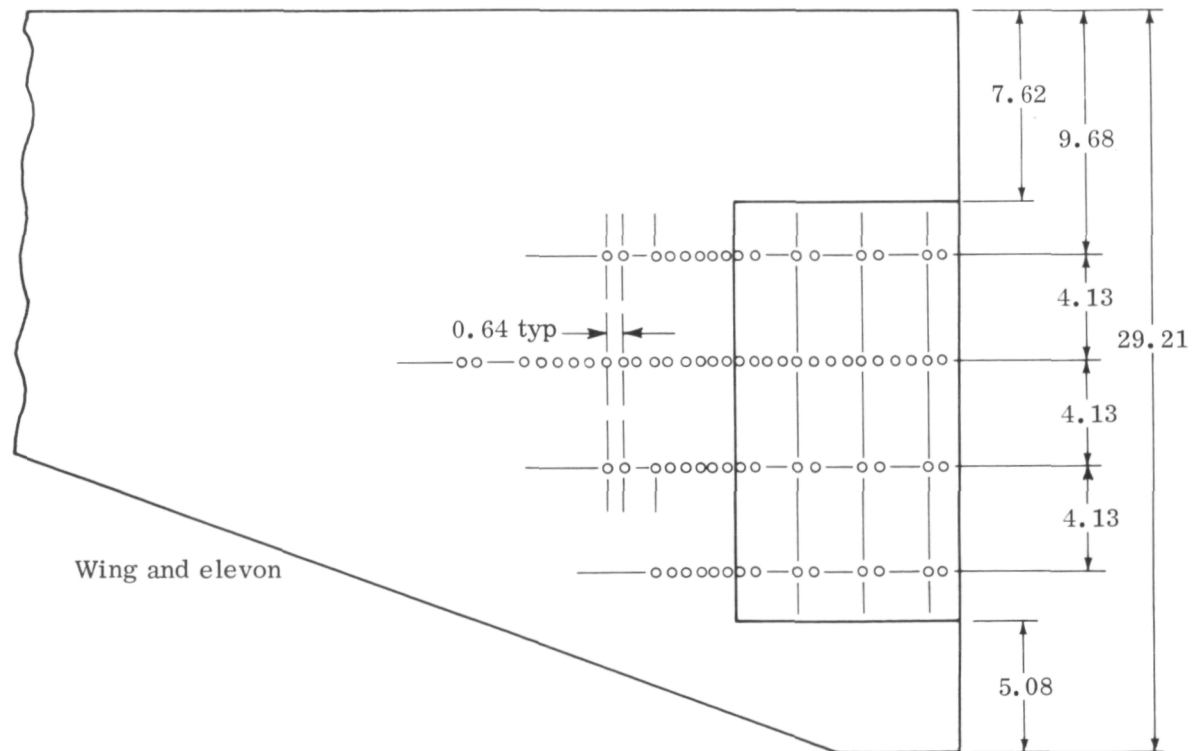
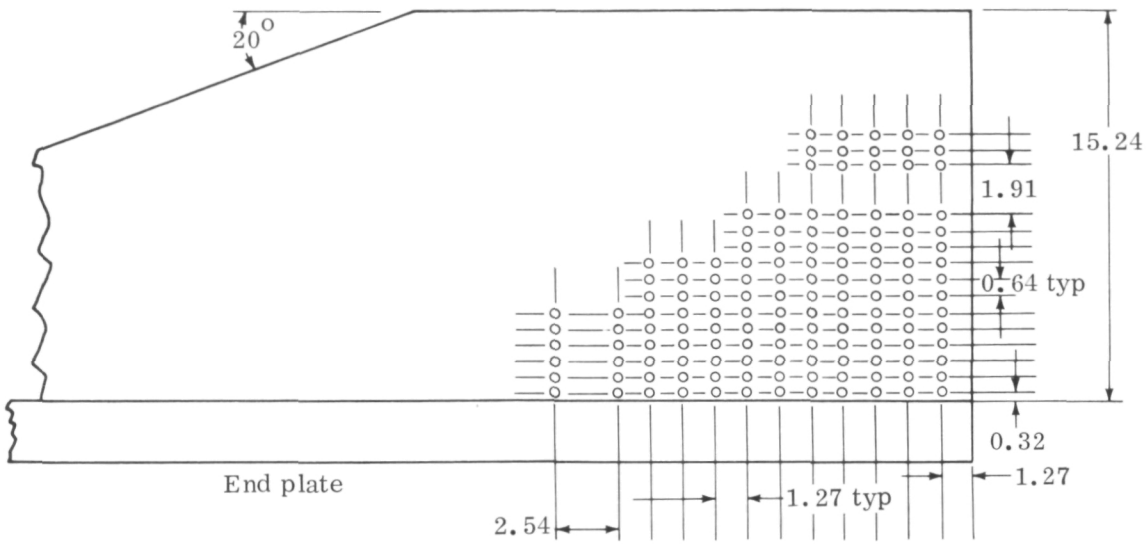
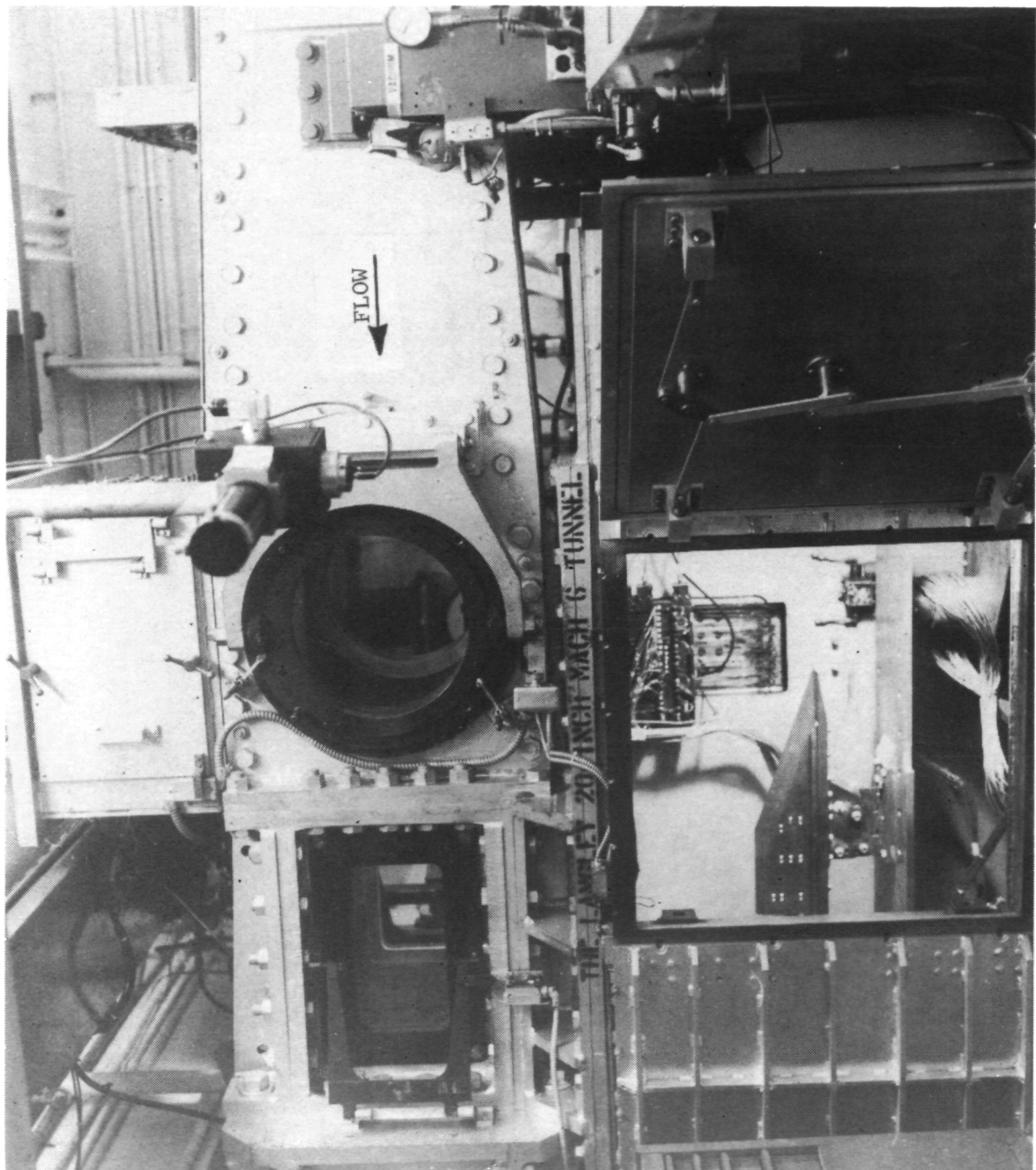


Figure 4.- Pressure orifice locations on wing, elevon, and end-plate surfaces; linear dimensions in cm.

L-77-109

Figure 5.—Photograph of Langley 20-inch Mach 6 tunnel showing wing elevon model mounted on injection system beneath test section.



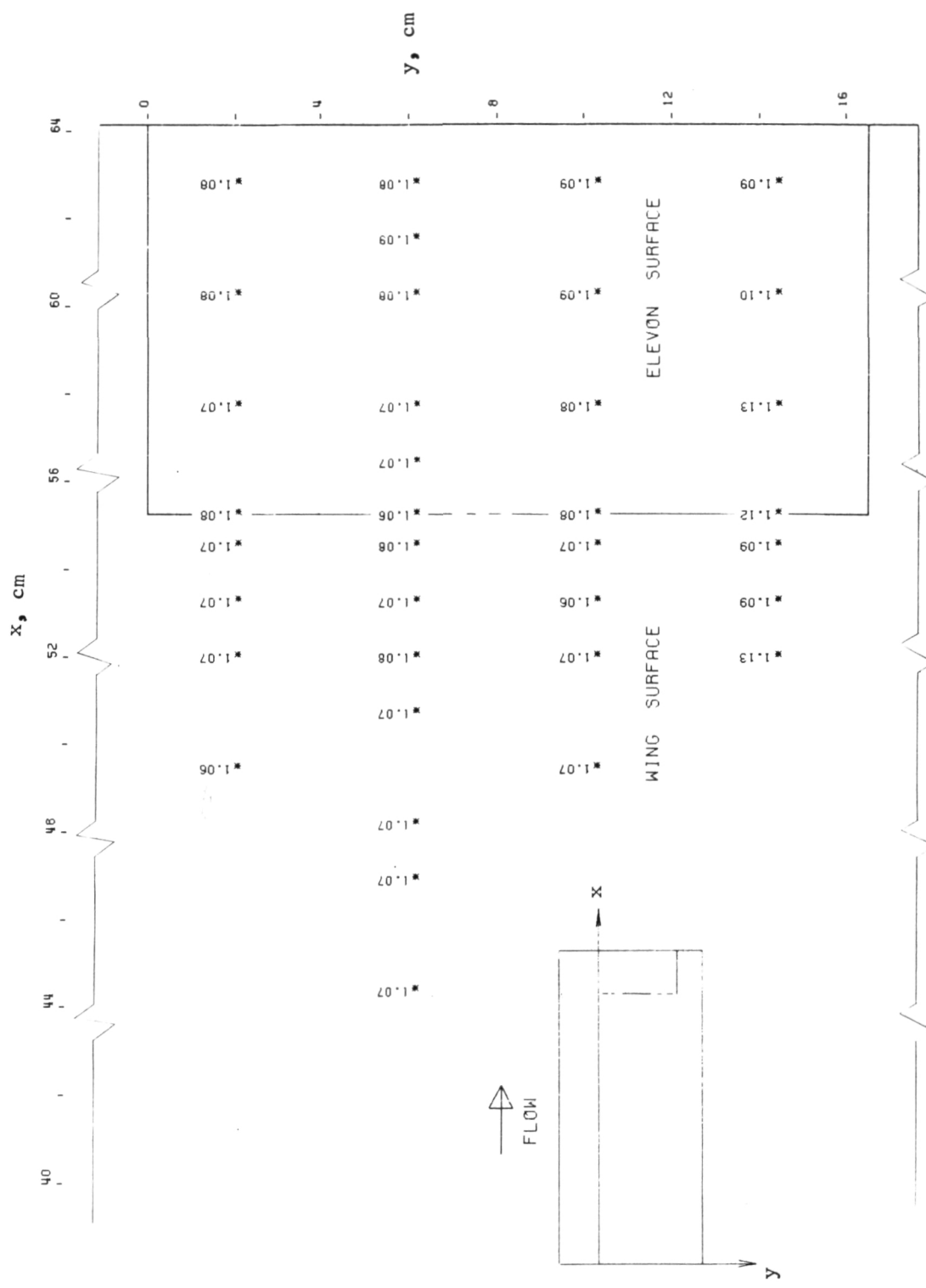


Figure 6.- Pressure-ratio (P) distribution on wing and elevon surfaces for $\Lambda = 0^\circ$ and $\epsilon = 0^\circ$.

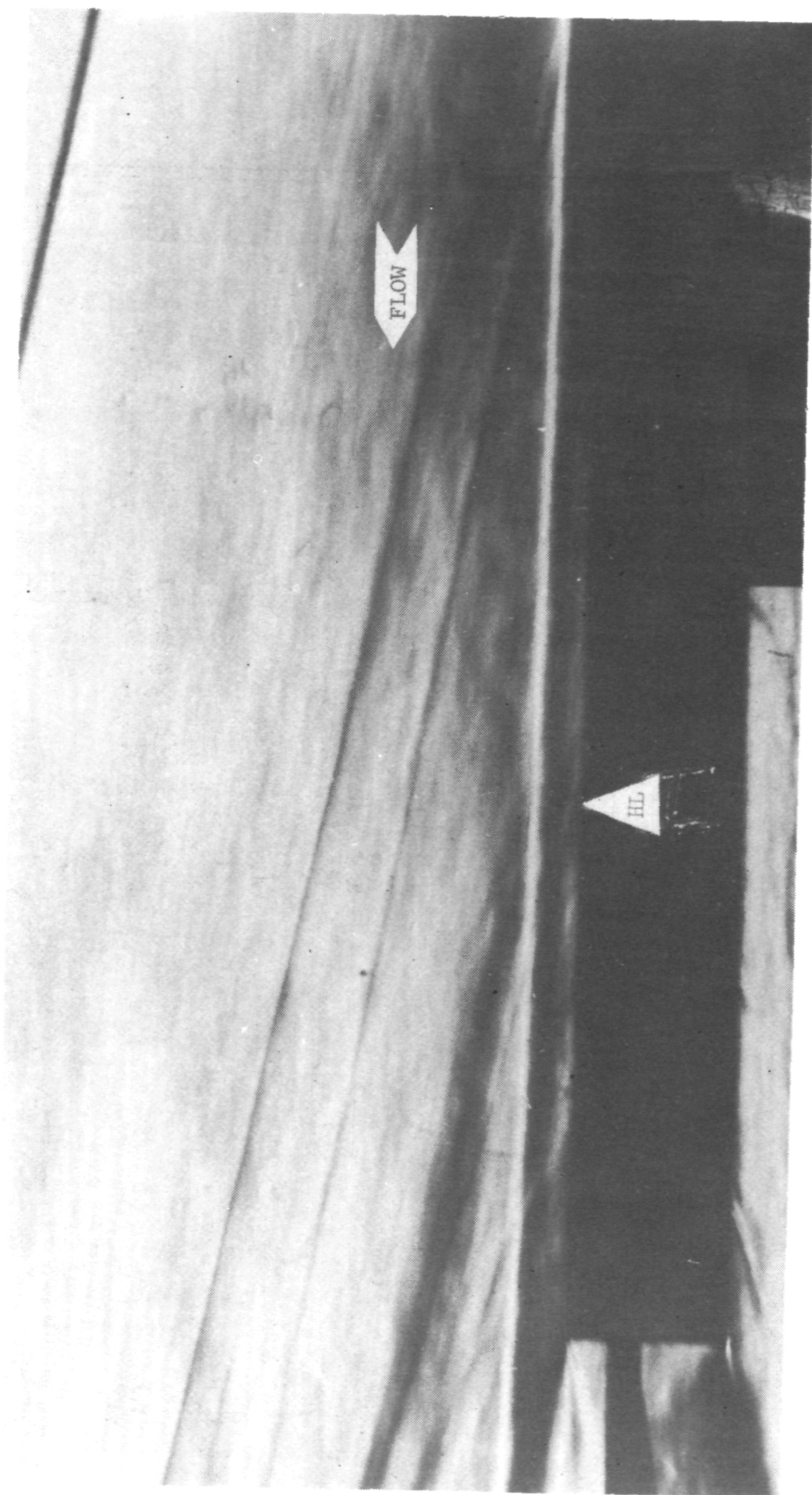


Figure 7.- Schlieren flow photograph for $\Lambda = 0^\circ$ and $\varepsilon = 0^\circ$.
L-77-110

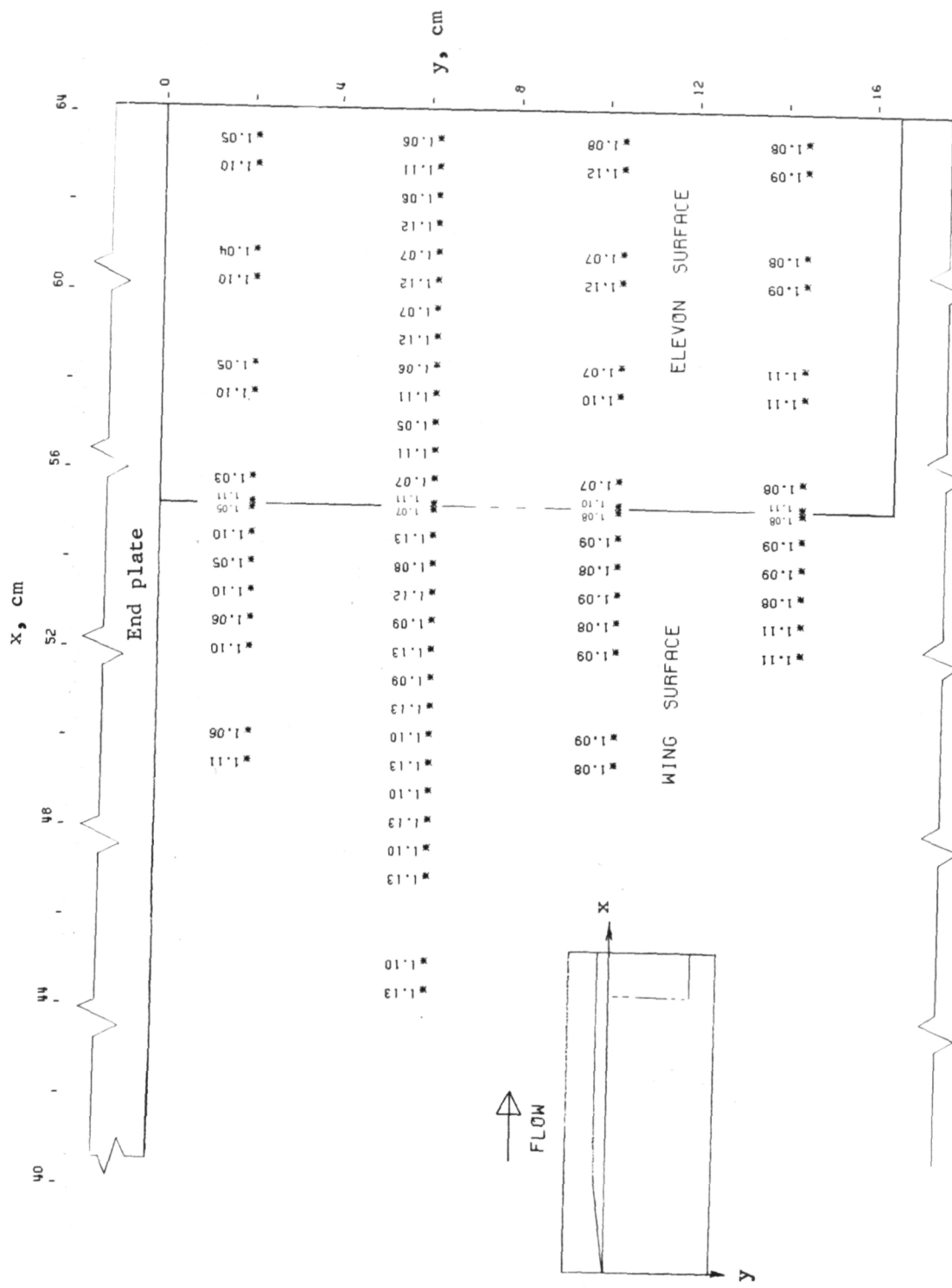


Figure 8.- Pressure-ratio (P) distribution on wing and elevon surfaces for $\Lambda = 0^\circ$, $\epsilon = 0^\circ$, and end plate attached.

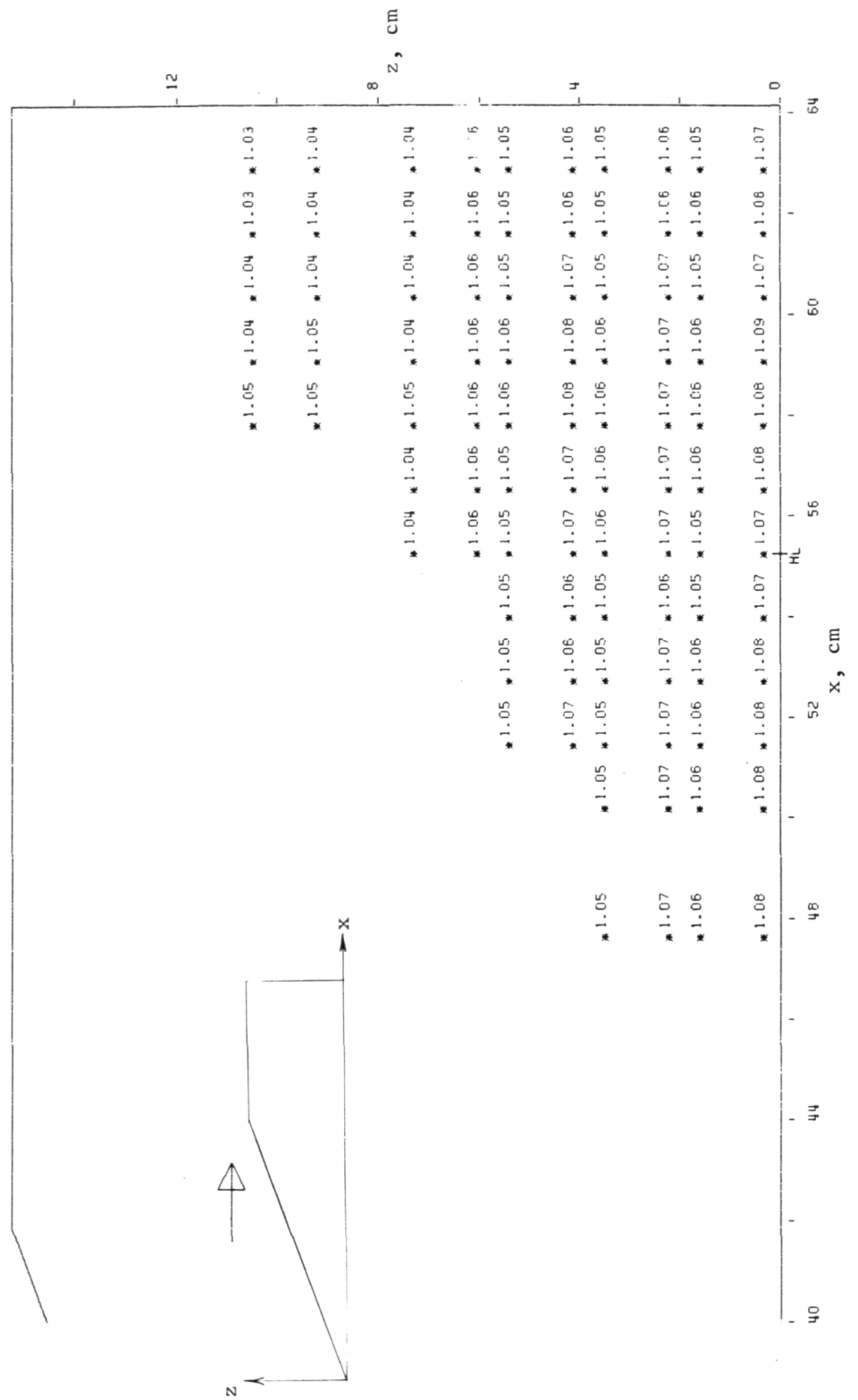


Figure 9.- Pressure-ratio (P) distribution on end-plate surface for $\Lambda = 0^\circ$ and $\epsilon = 0^\circ$.

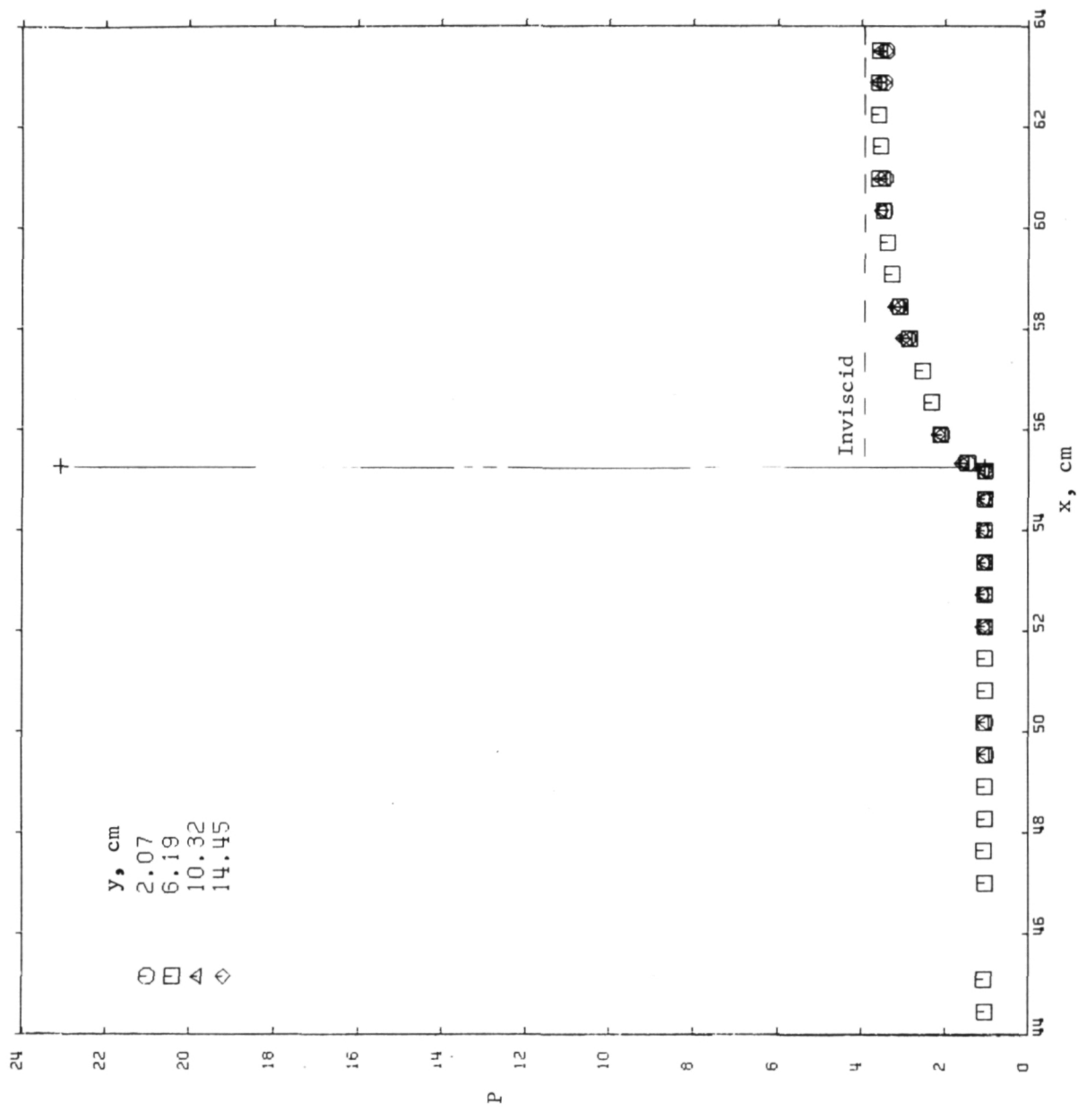


Figure 10.- Streamwise pressure-ratio distributions on wing and elevon surfaces for $\Lambda = 0^\circ$ and $\epsilon = 10^\circ$.

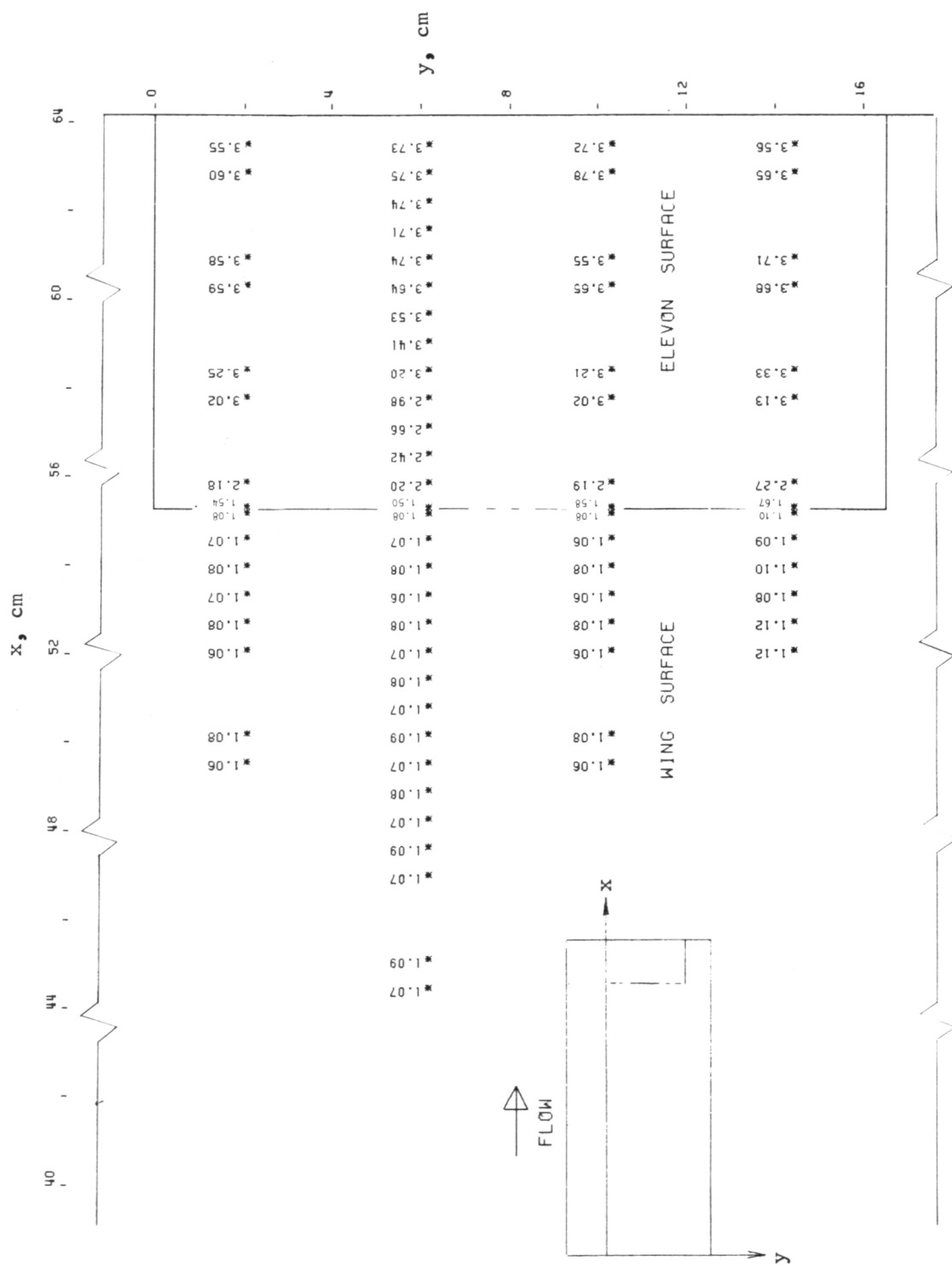
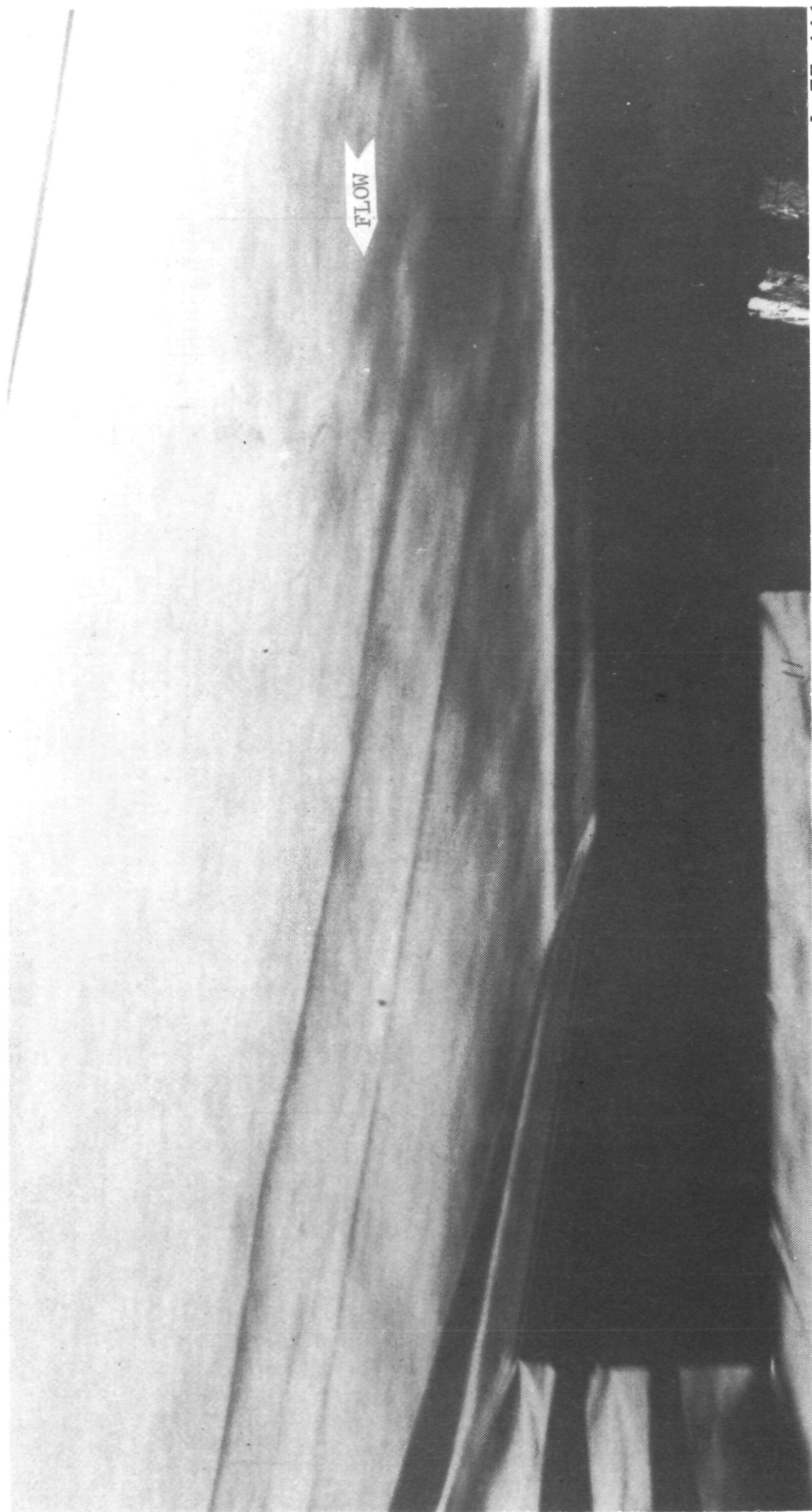


Figure 11.— Pressure-ratio (P) distribution on wing and elevon surfaces for $\Lambda = 0^\circ$ and $\epsilon = 10^\circ$.



L-77-111

Figure 12.- Schlieren flow photograph for $\Lambda = 0^\circ$ and $\epsilon = 10^\circ$.

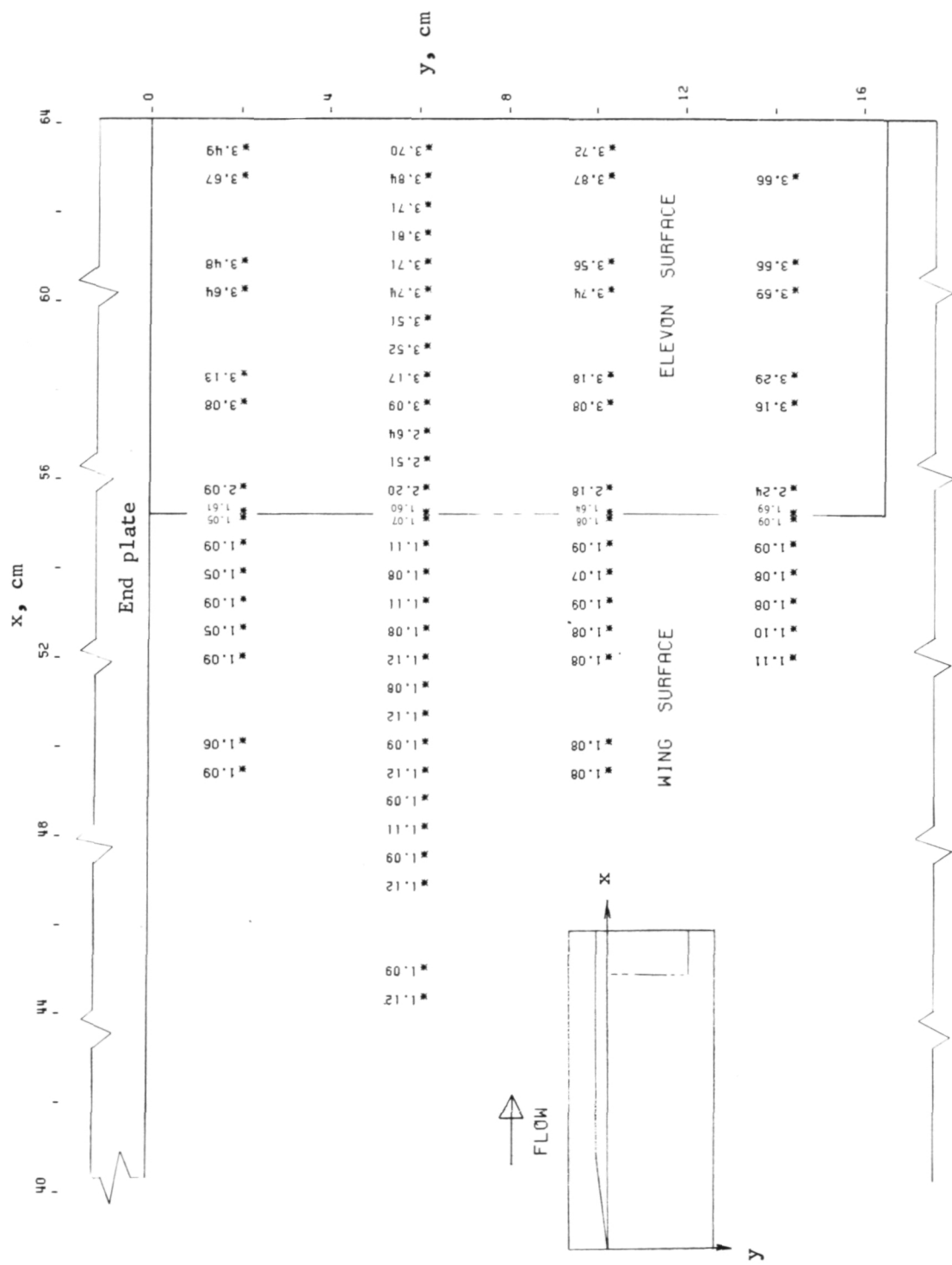


Figure 13.- Pressure-ratio (P) distribution on wing and elevon surfaces for $\Lambda = 0^\circ$, $\epsilon = 10^\circ$, and end plate attached.

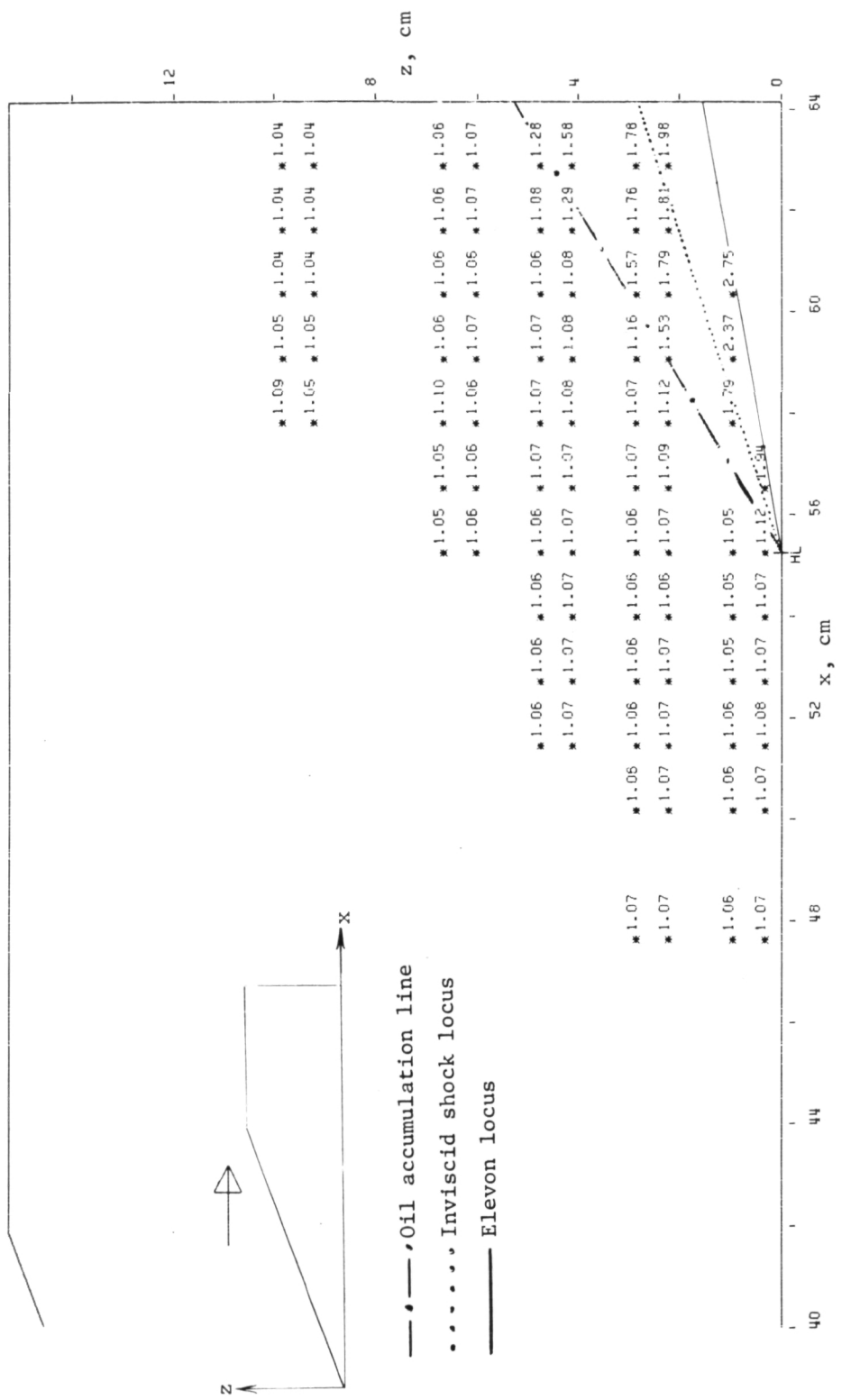
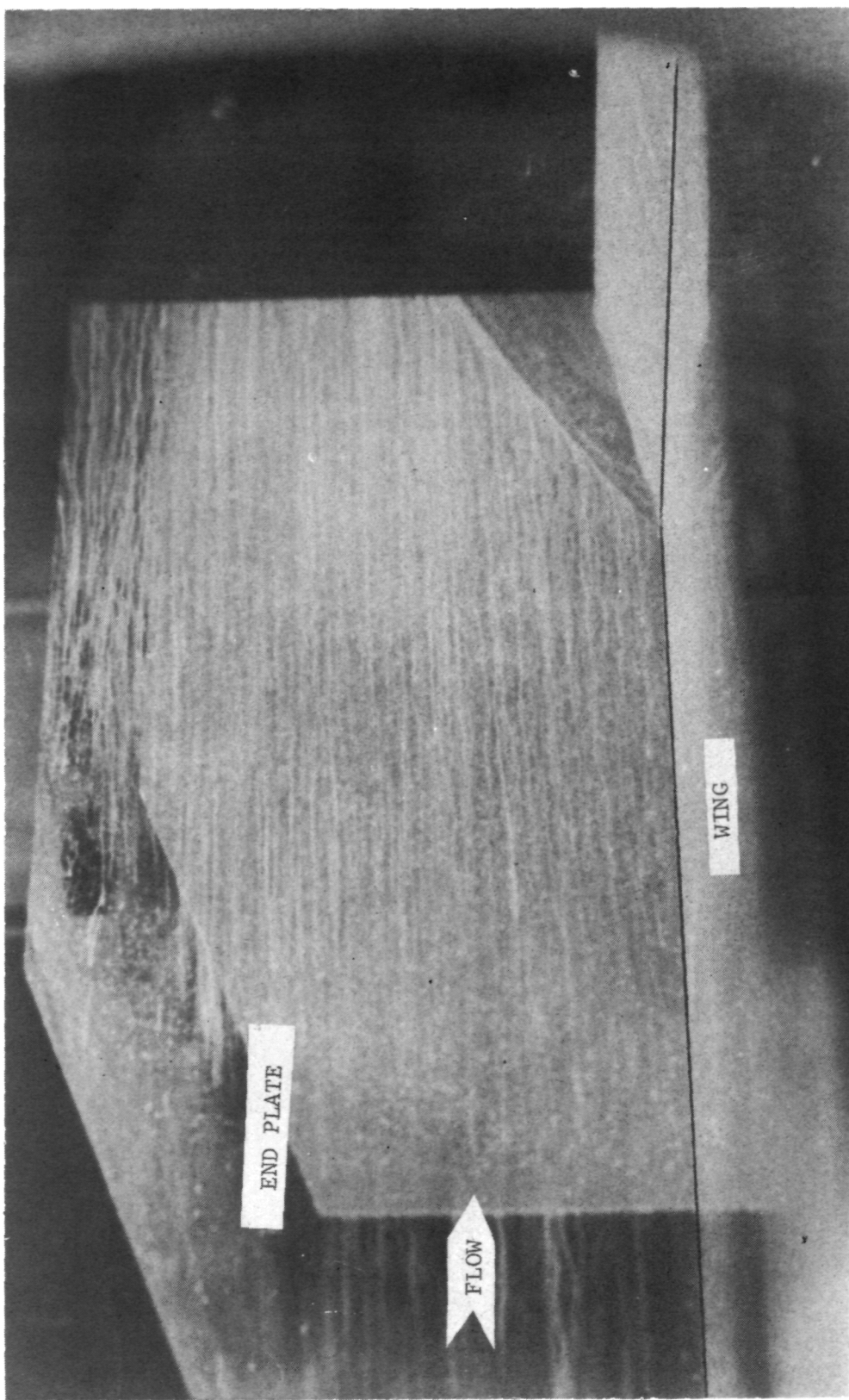


Figure 14.- Pressure-ratio (P) distribution on end-plate surface for $\Lambda = 0^\circ$ and $\epsilon = 10^\circ$.

L-77-112

Figure 15.- Frame from profile view of surface-oil-flow motion picture for $\Lambda = 0^\circ$, $\epsilon = 100$, and end plate attached.



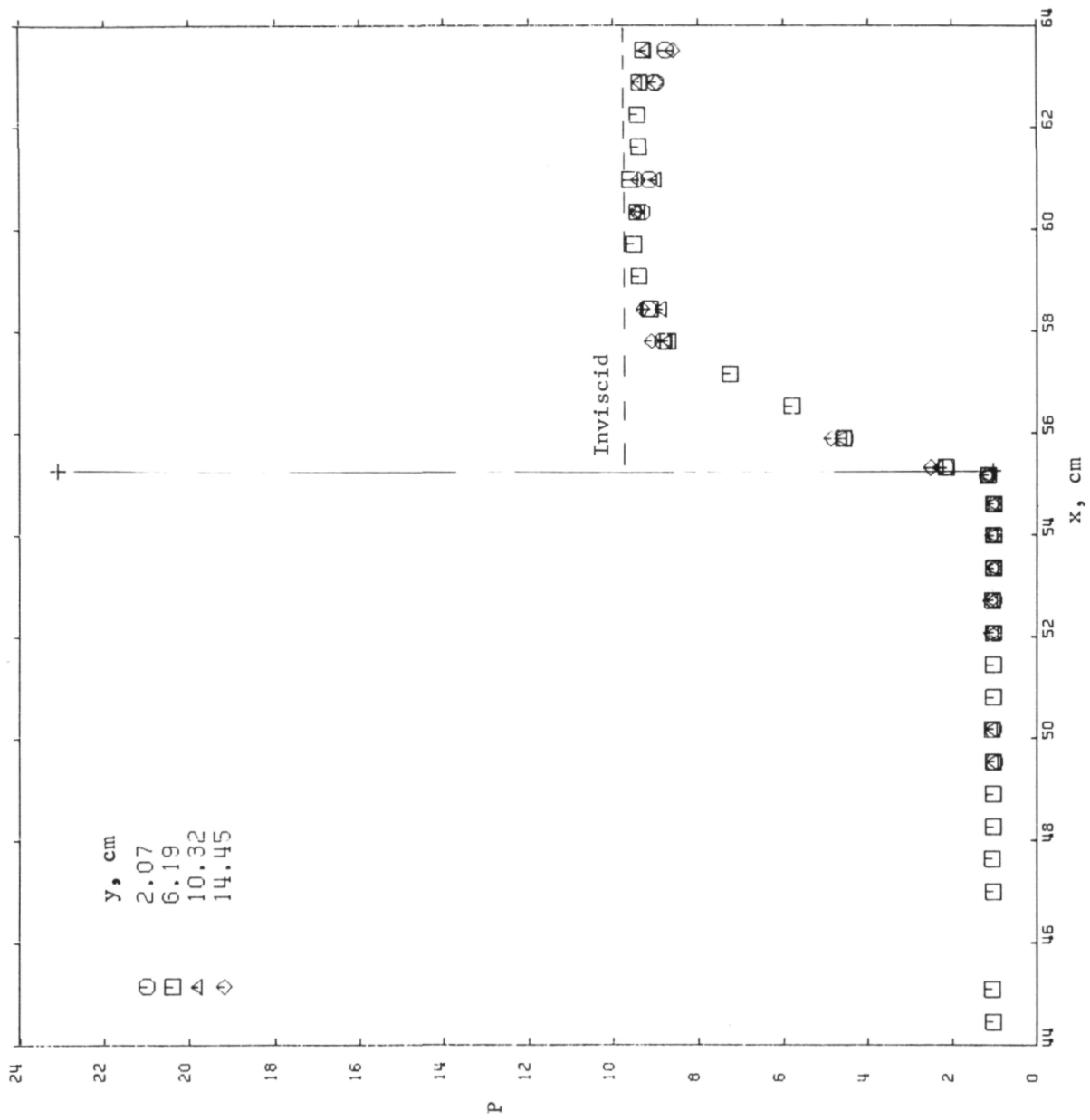


Figure 16.— Streamwise pressure-ratio distributions on wing and elevon surfaces for $\Lambda = 0^\circ$ and $\varepsilon = 20^\circ$.

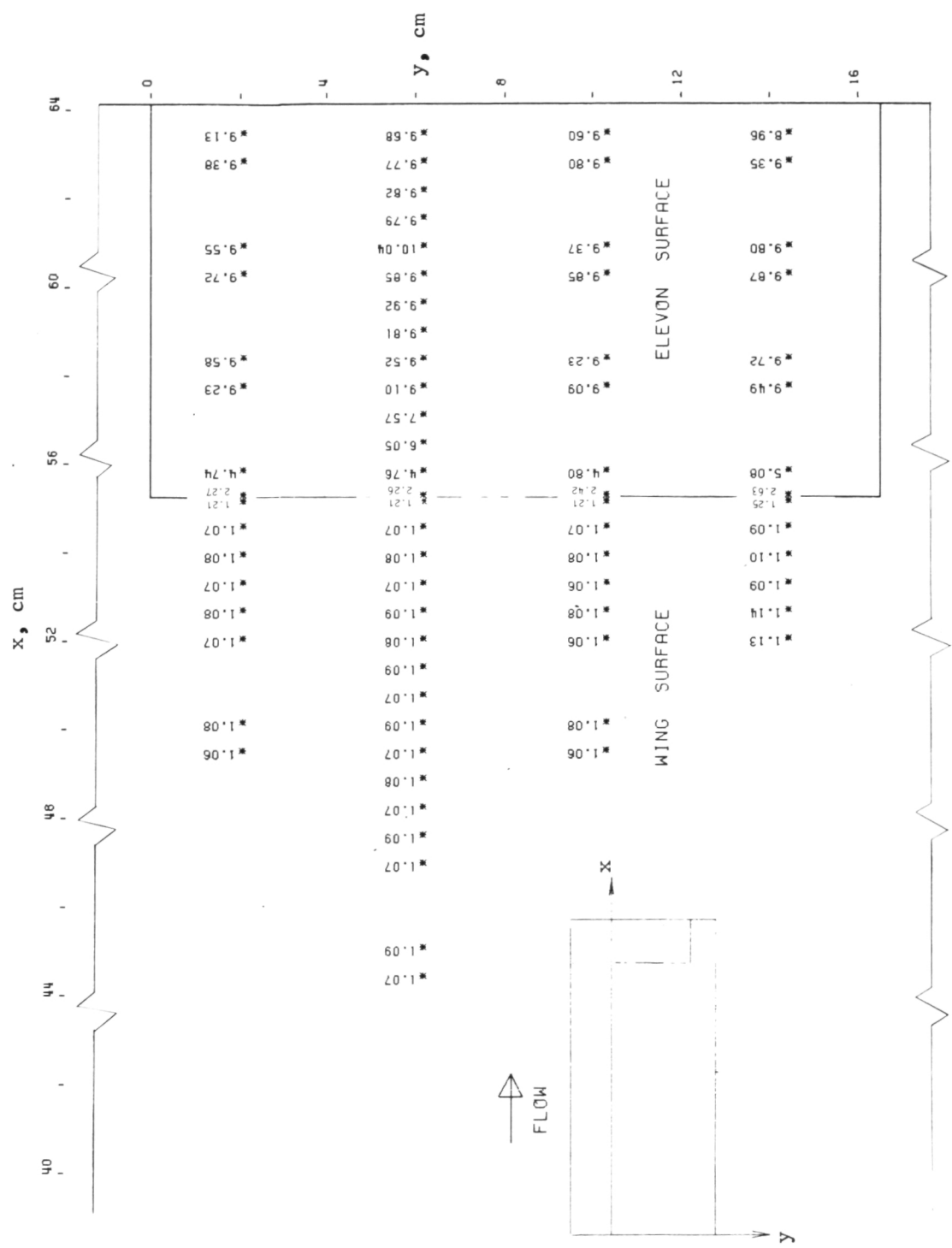


Figure 17.- Pressure-ratio (P) distribution on wing and elevon surfaces for $\Lambda = 0^\circ$ and $\epsilon = 20^\circ$.

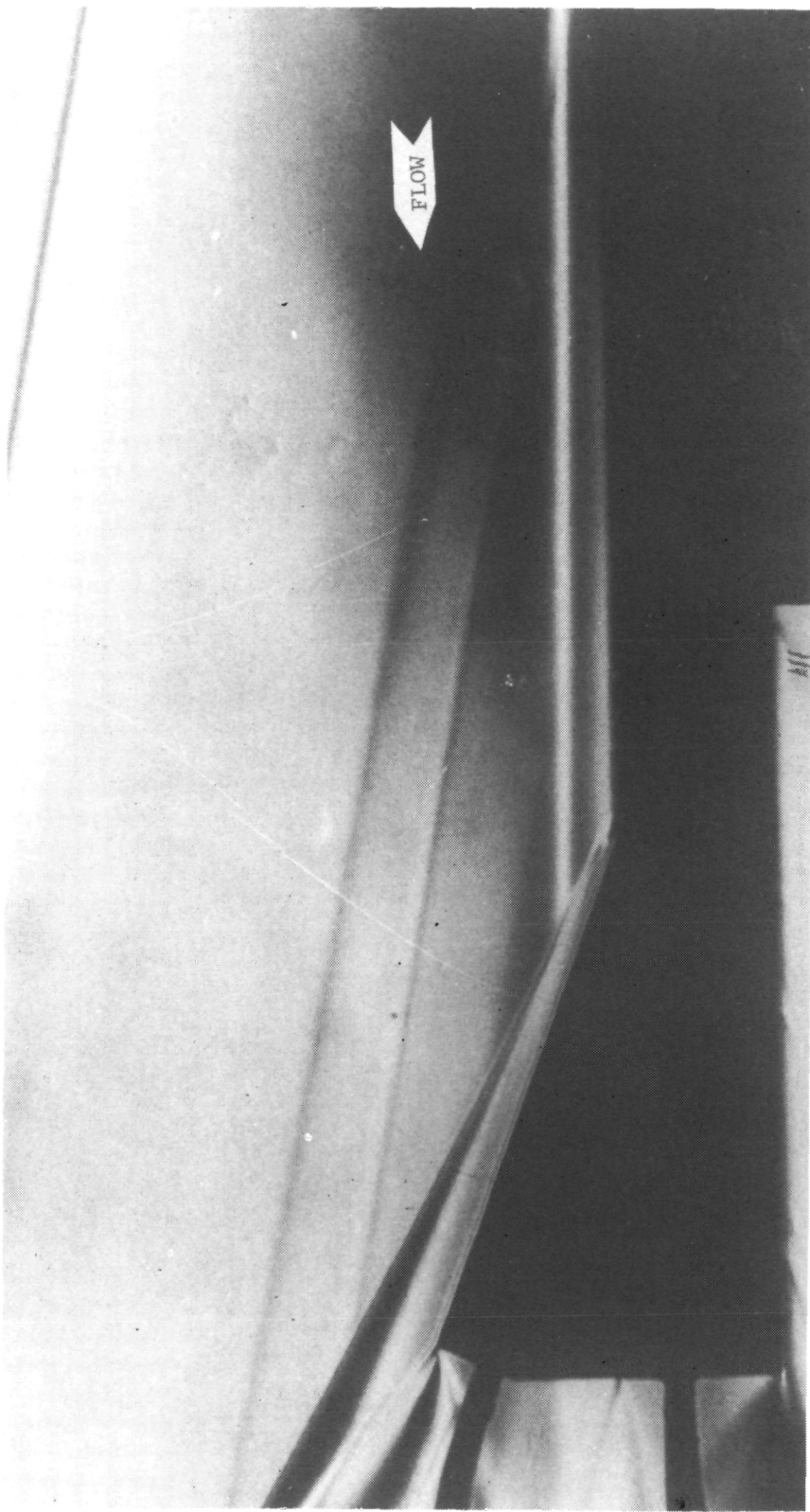


Figure 18.- Schlieren flow photograph for $\Lambda = 0^\circ$ and $\epsilon = 20^\circ$.
L-77-113

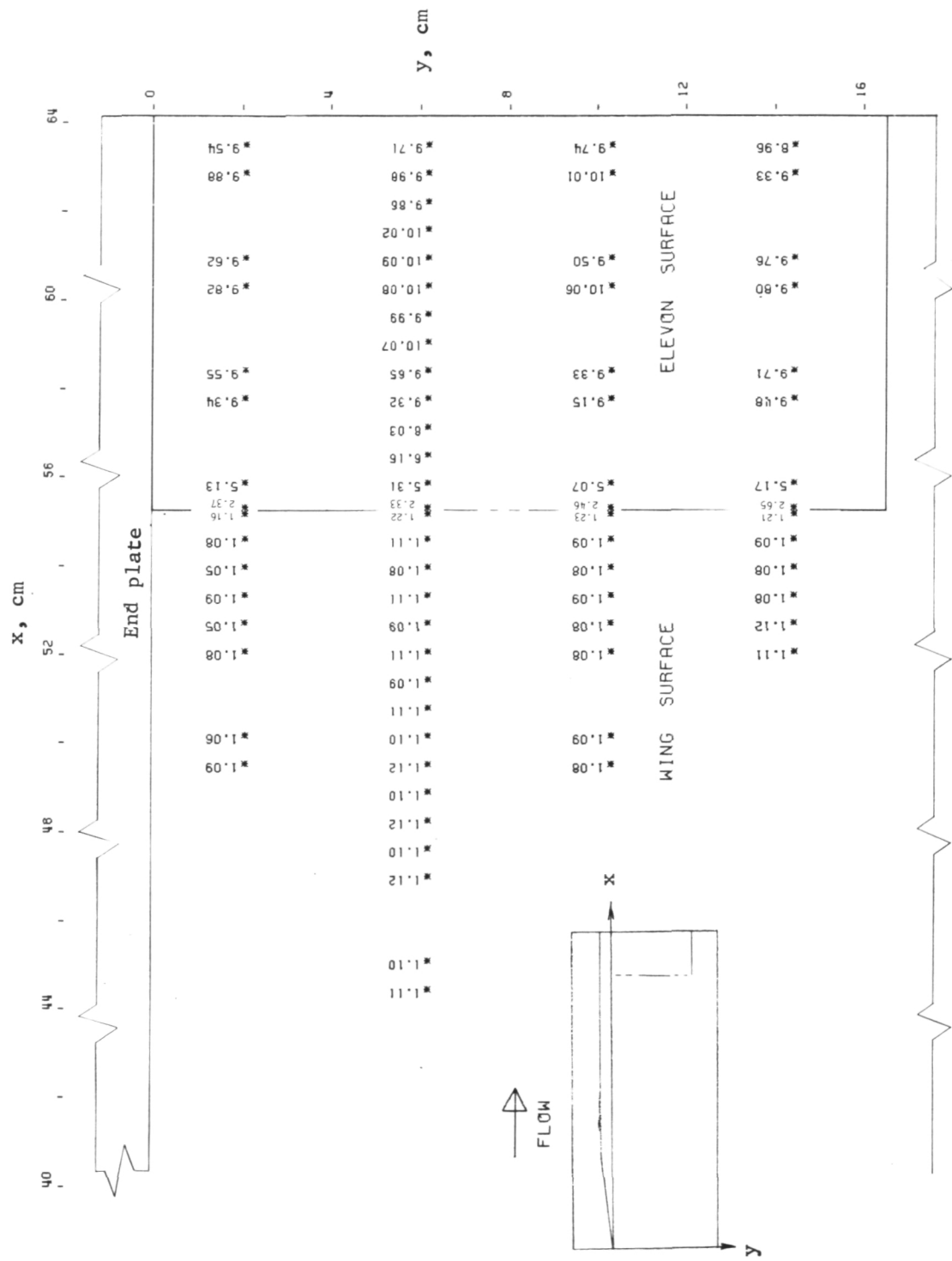


Figure 19.- Pressure-ratio (P) distribution on wing and elevon surfaces for $\Lambda = 0^\circ$, $\epsilon = 20^\circ$, and end plate attached.

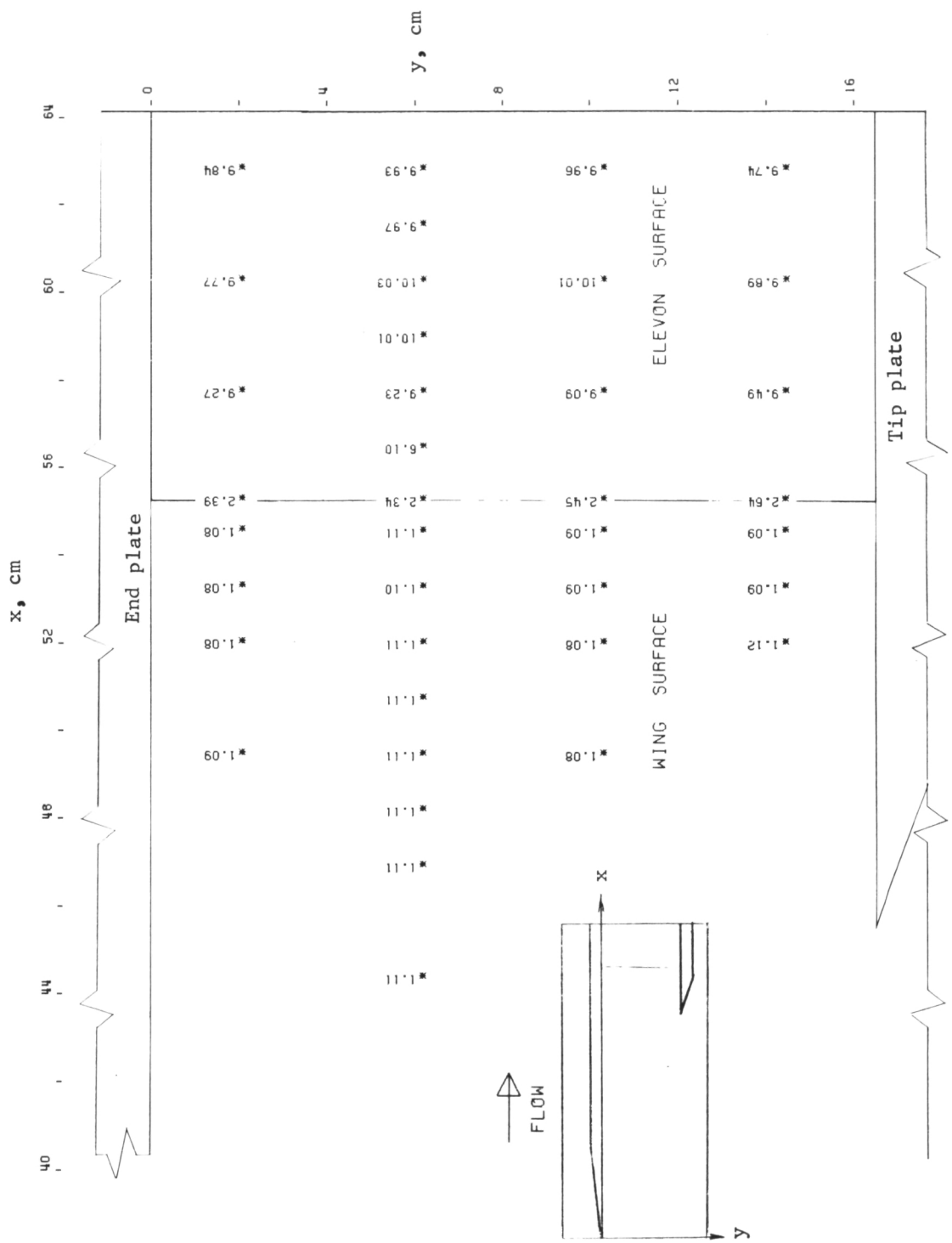


Figure 20.— Pressure-ratio (P) distribution on wing and elevon surfaces for $\Lambda = 0^\circ$, $\epsilon = 20^\circ$, end plate attached, and tip plate attached.

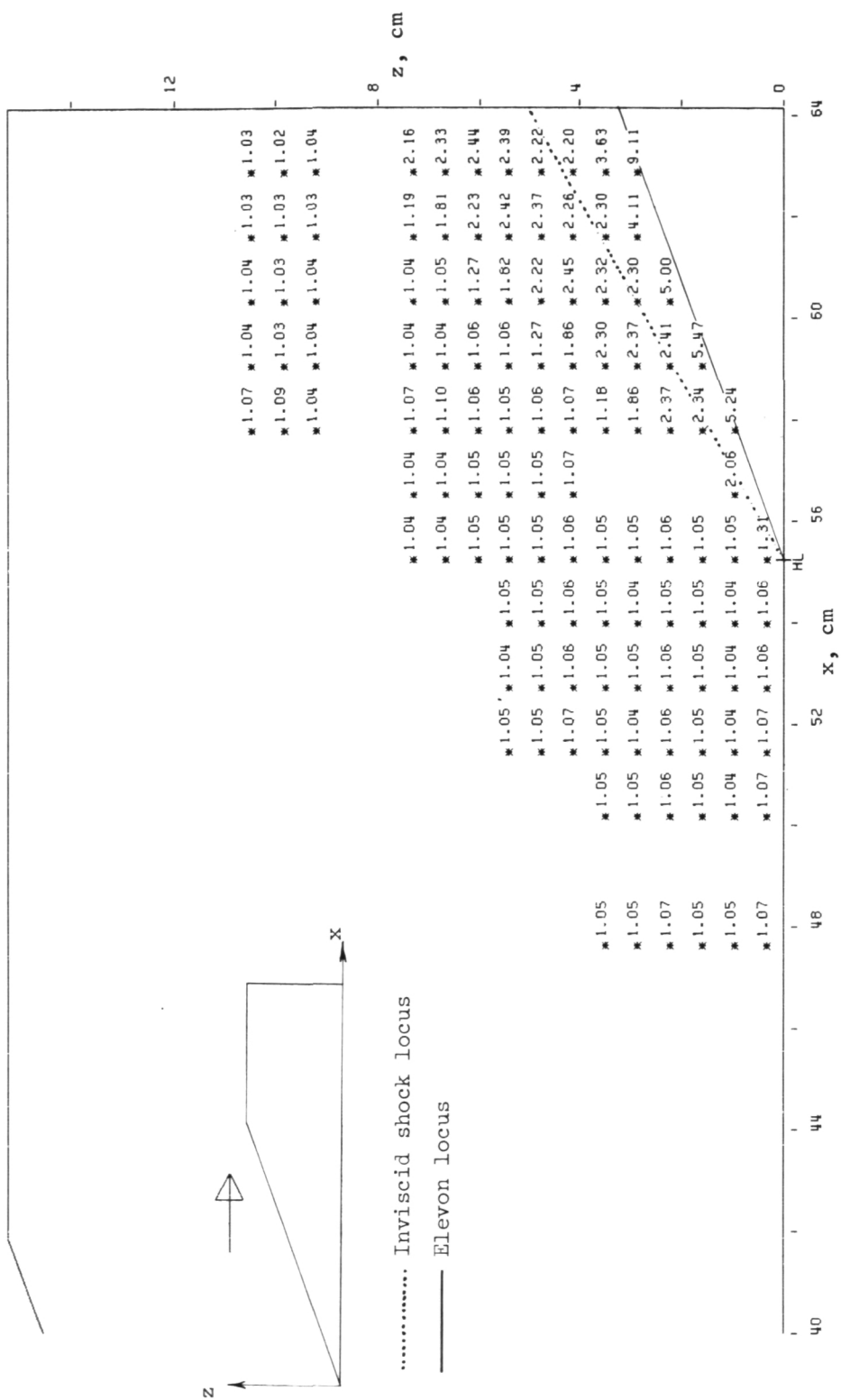


Figure 21.— Pressure-ratio (P) distribution on end-plate surface for $\Lambda = 0^\circ$ and $\epsilon = 20^\circ$.

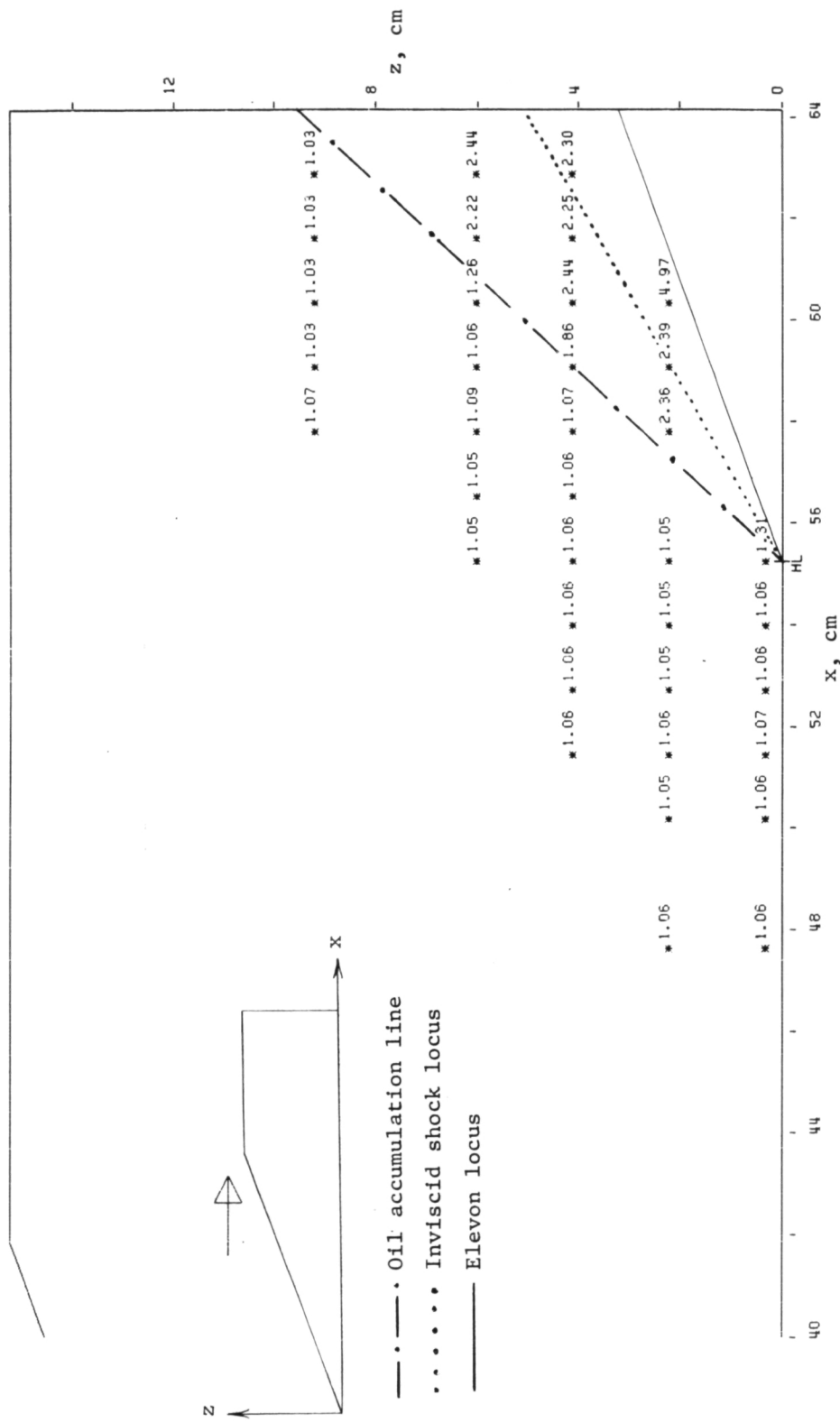
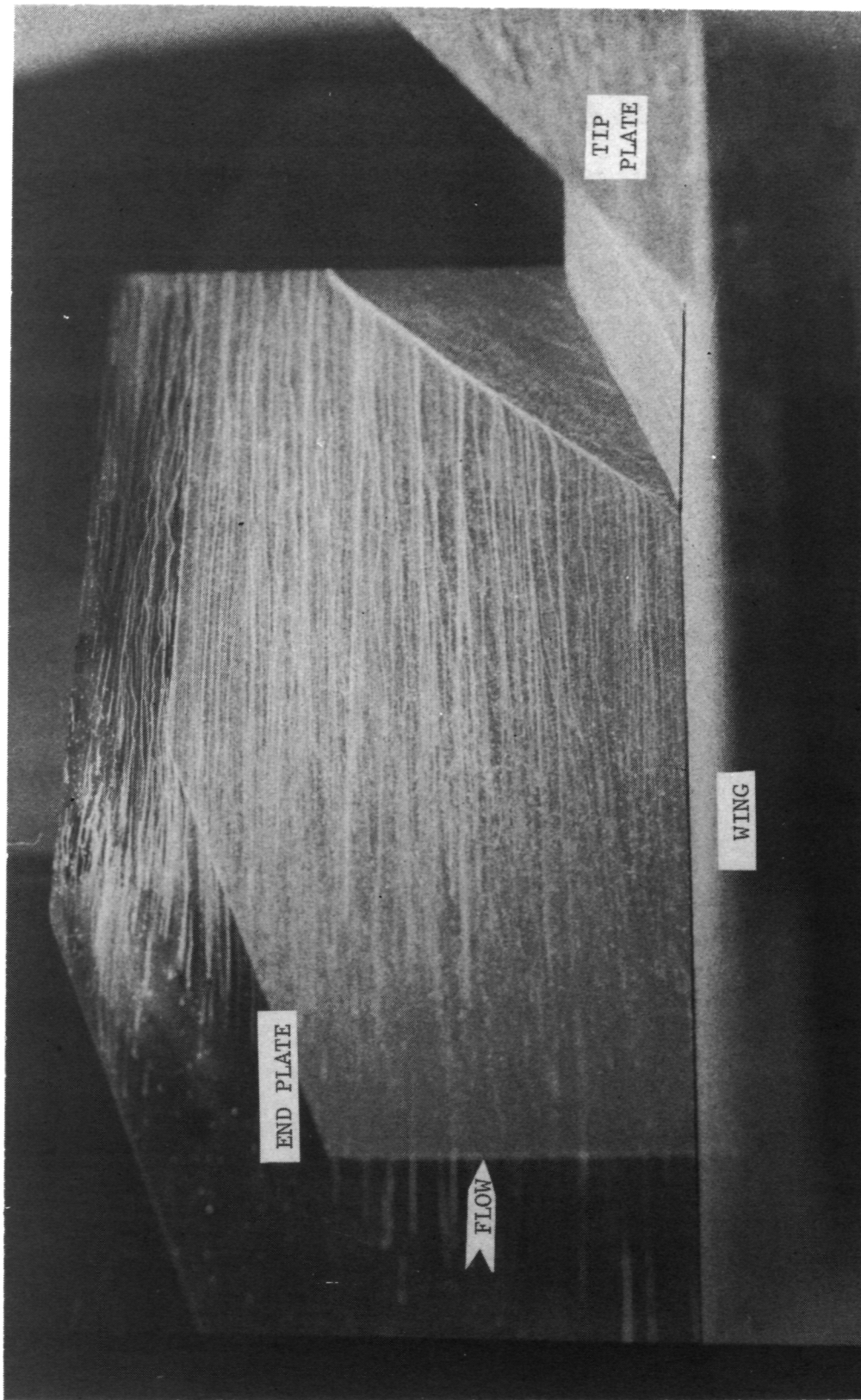


Figure 22.— Pressure-ratio (P) distribution on end-plate surface for $\Lambda = 0^\circ$, $\epsilon = 20^\circ$, and tip plate attached.

L-77-114
Figure 23.- Frame from surface-oil-flow motion picture for $\Lambda = 0^\circ$, $\epsilon = 20^\circ$, end plate attached, and tip plate attached.



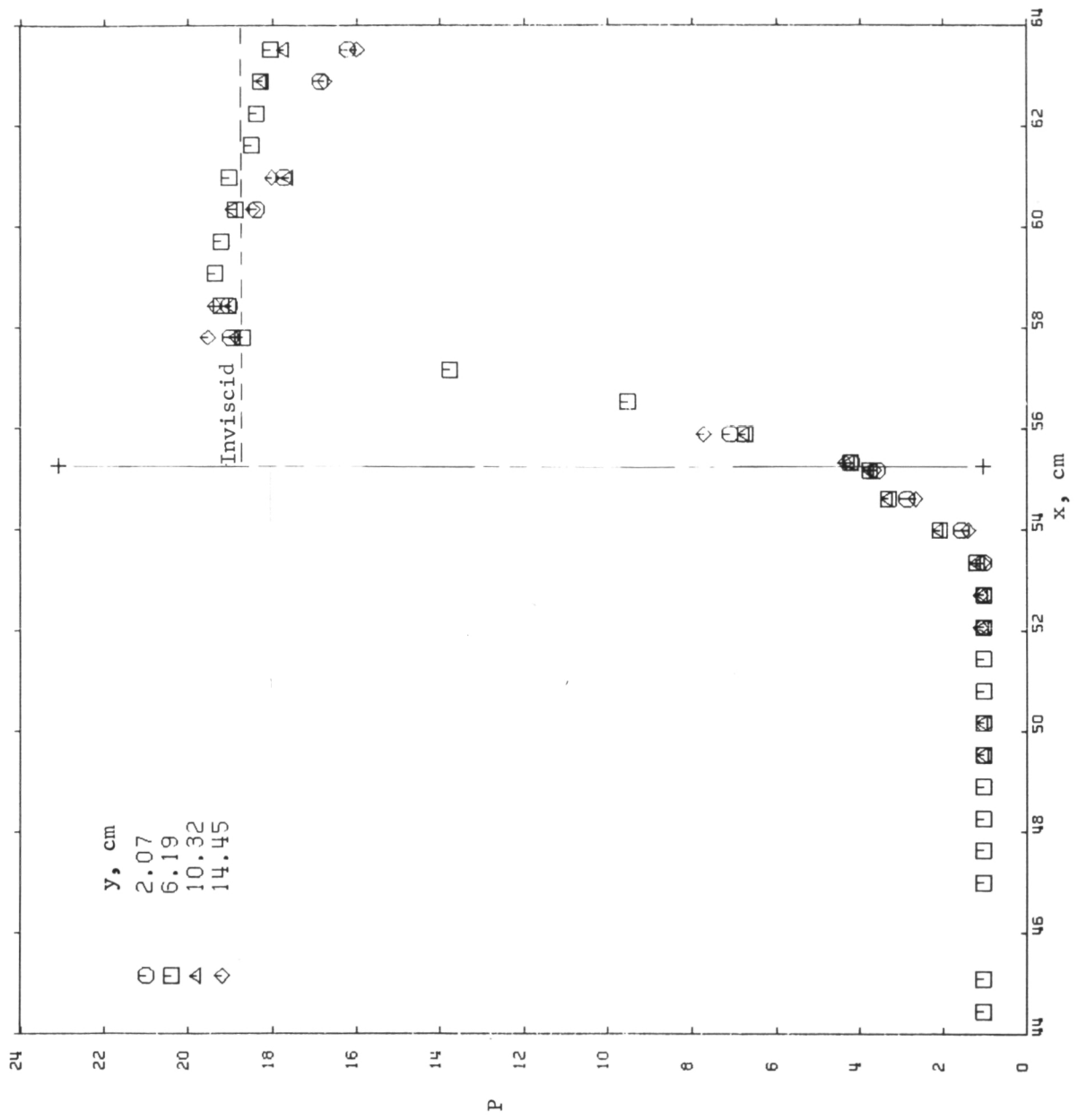


Figure 24.- Streamwise pressure-ratio distributions on wing and elevon surfaces for $\Lambda = 0^\circ$ and $\varepsilon = 30^\circ$.

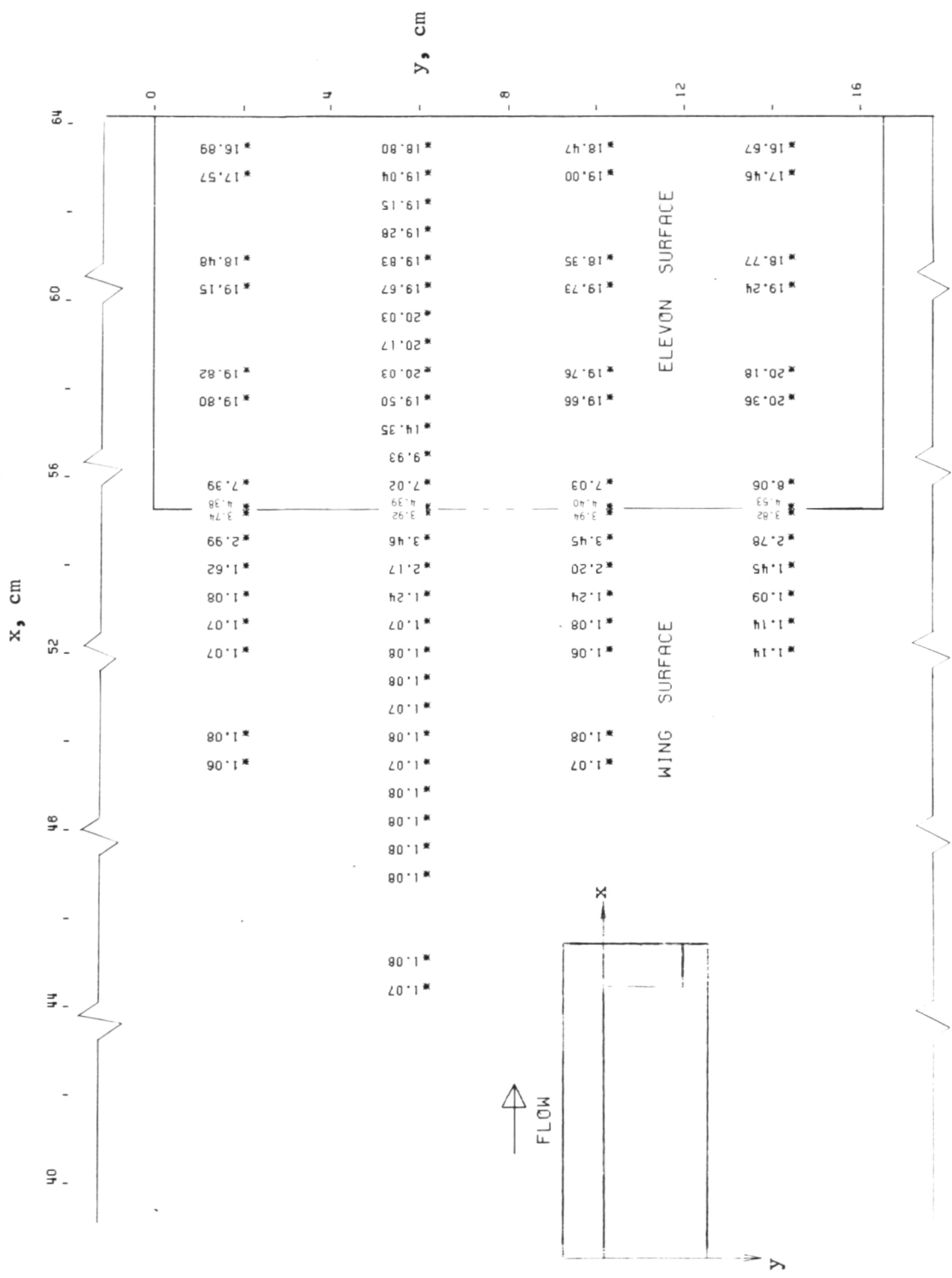
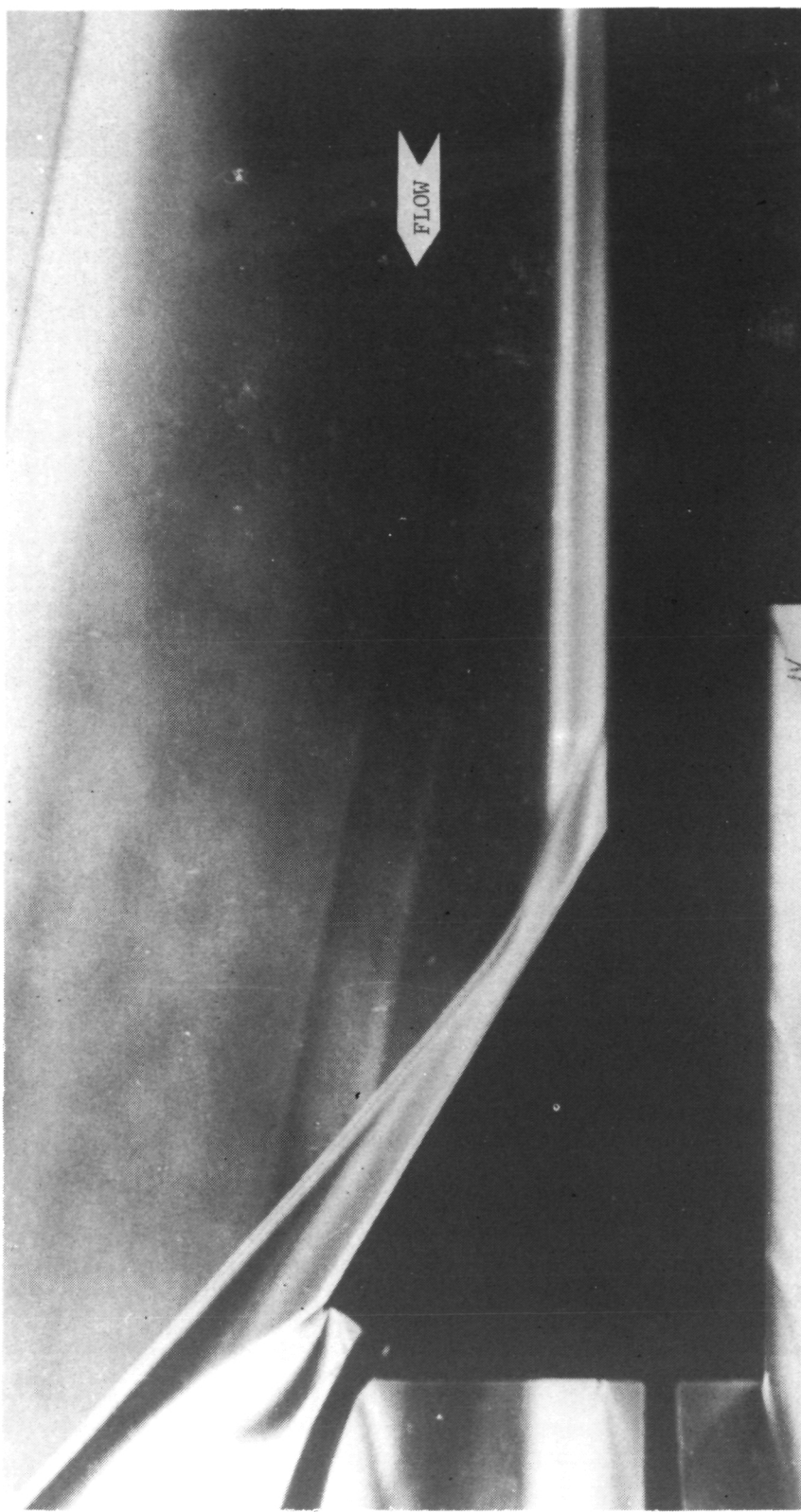


Figure 25.- Pressure-ratio (P) distribution on wing and elevon surfaces for $\Lambda = 0^\circ$ and $\epsilon = 30^\circ$.

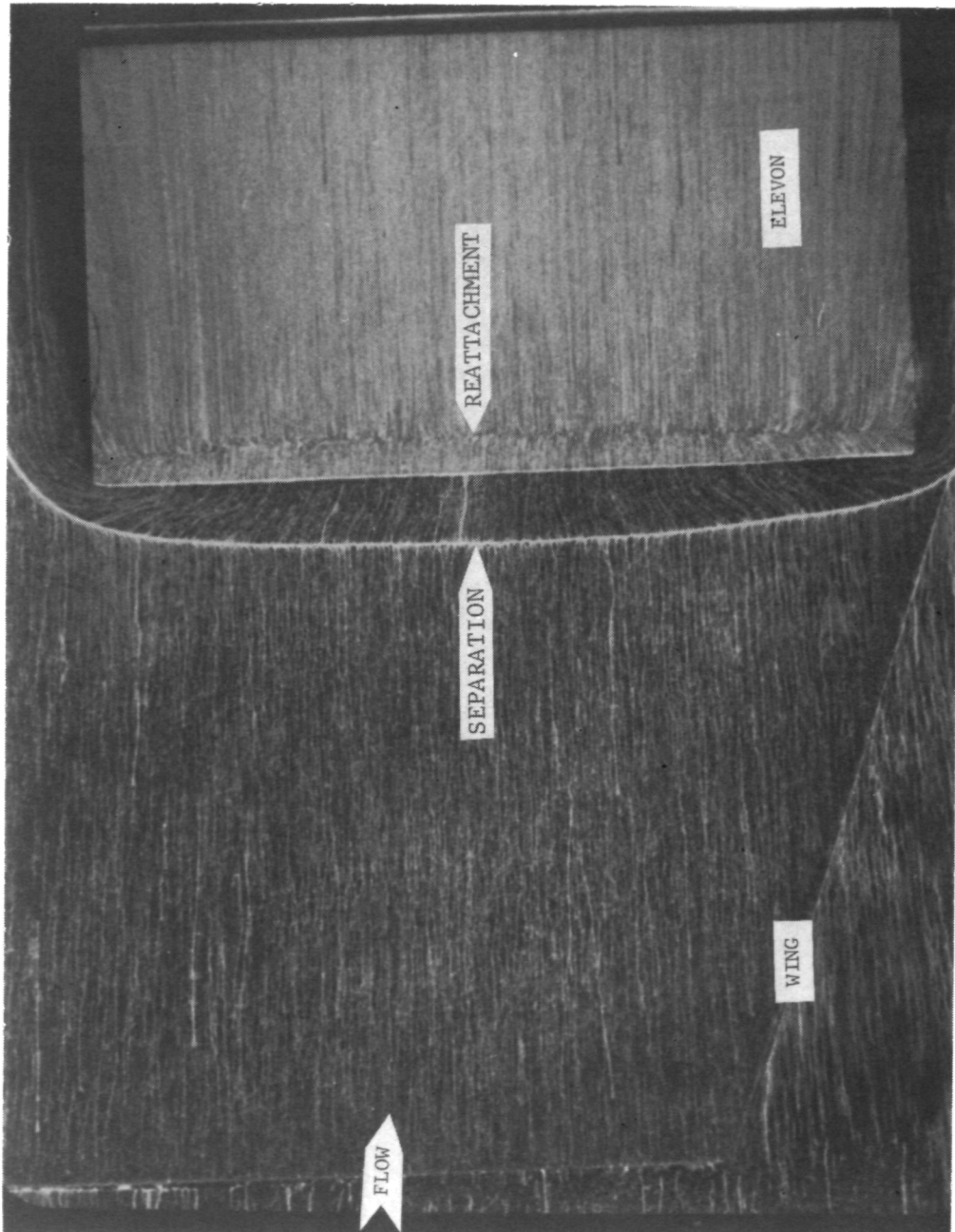
L-77-115

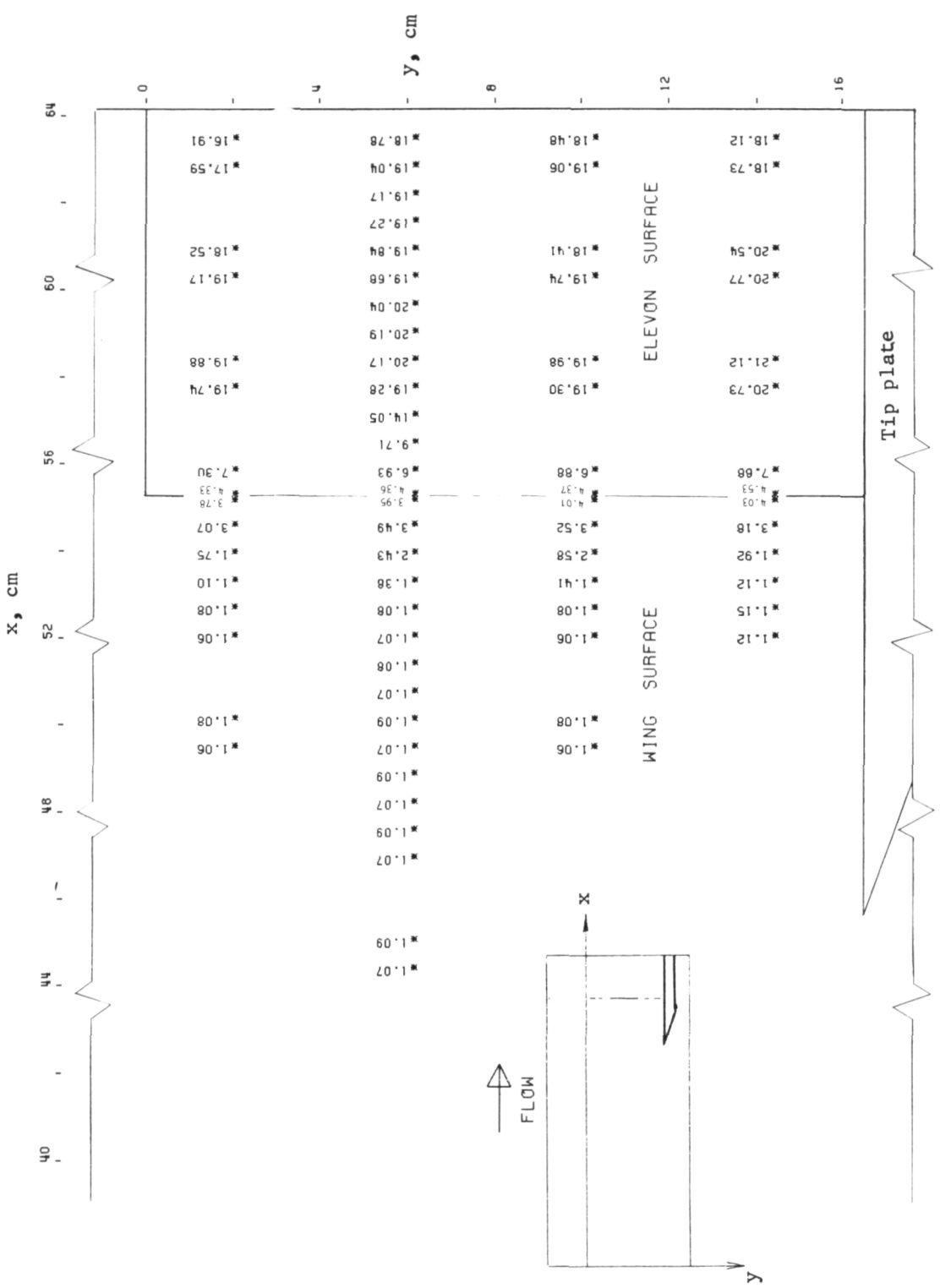
Figure 26.- Schlieren flow photograph for $\Lambda = 0^\circ$ and $\epsilon = 30^\circ$.



L-77-116

Figure 27.— Frame from planform view of surface-oil-flow motion picture for $\Lambda = 0^\circ$ and $\epsilon = 30^\circ$.





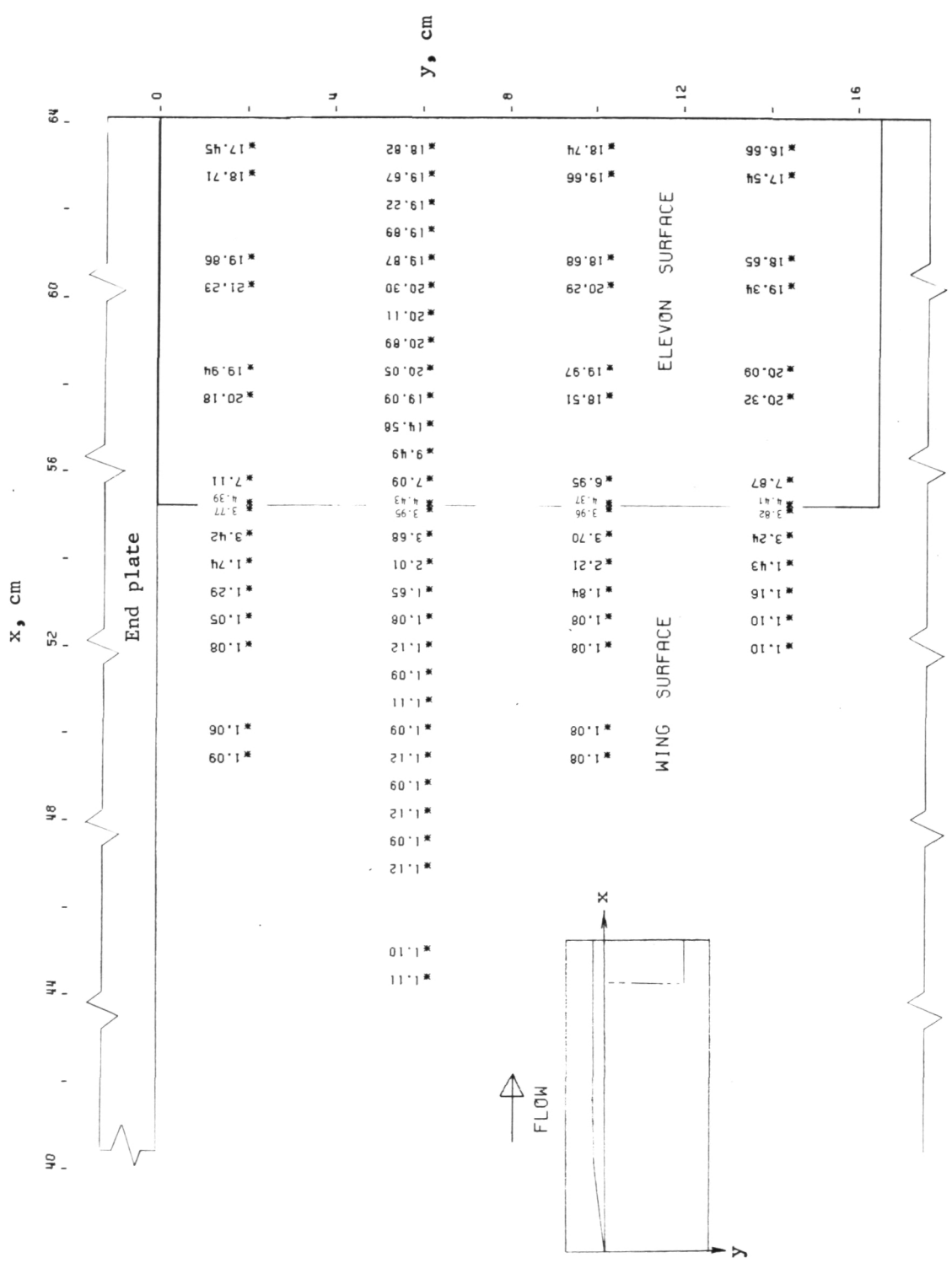


Figure 29.- Pressure-ratio (P) distribution on wing and elevon surfaces for $\Lambda = 0^\circ$, $\epsilon = 30^\circ$, and end plate attached.

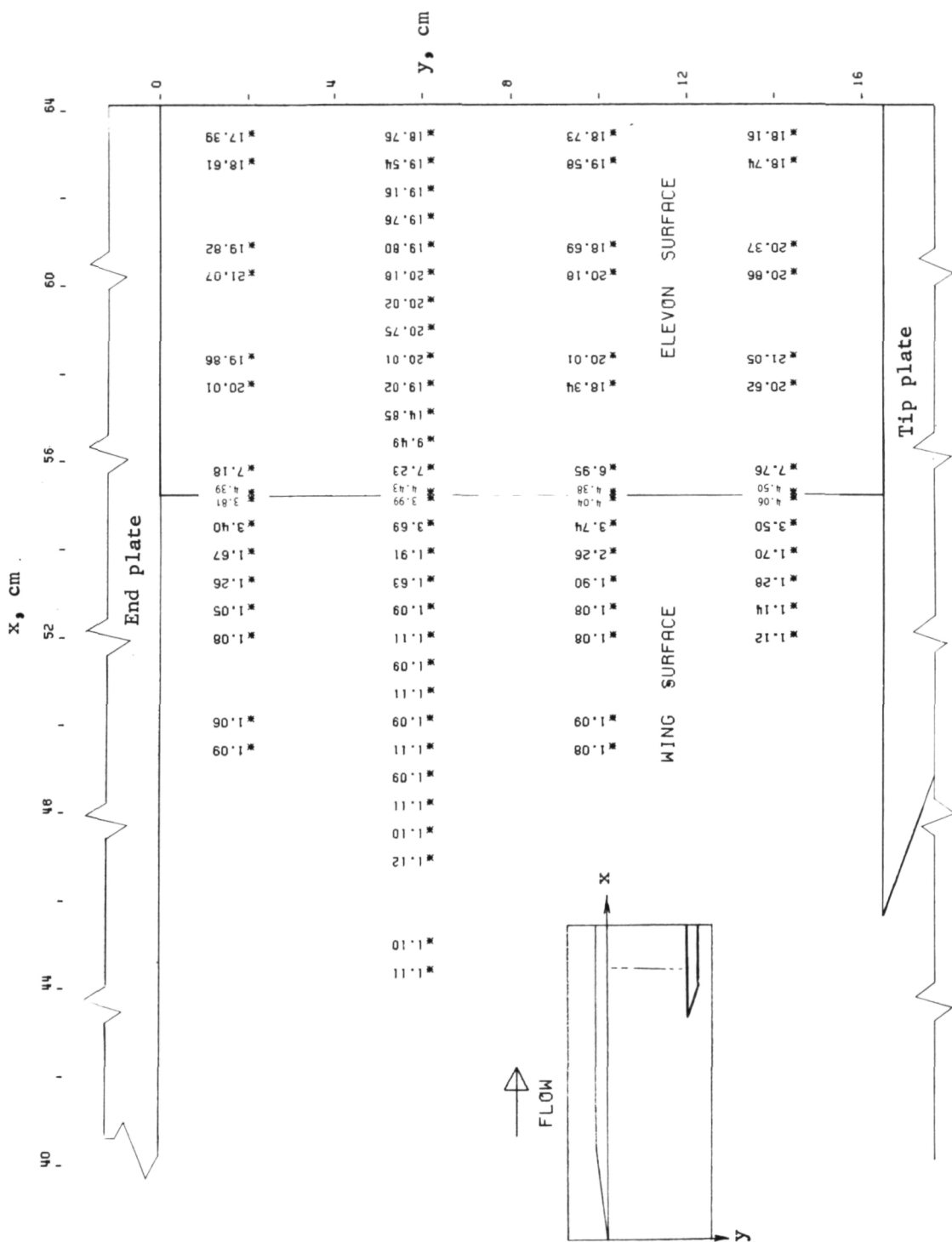


Figure 30.- Pressure-ratio (P) distribution on wing and elevon surfaces for $\Lambda = 0^\circ$, $\epsilon = 30^\circ$, end plate attached, and tip plate attached.



Figure 31.- Frame from surface-oil-flow motion picture for $\Lambda = 0^\circ$, $\epsilon = 30^\circ$, and end plate attached. L-77-117



Figure 32.- Frame from surface-oil-flow motion picture for $\Lambda = 0^\circ$,
 $\epsilon = 30^\circ$, end plate attached, and tip plate attached. L-77-118

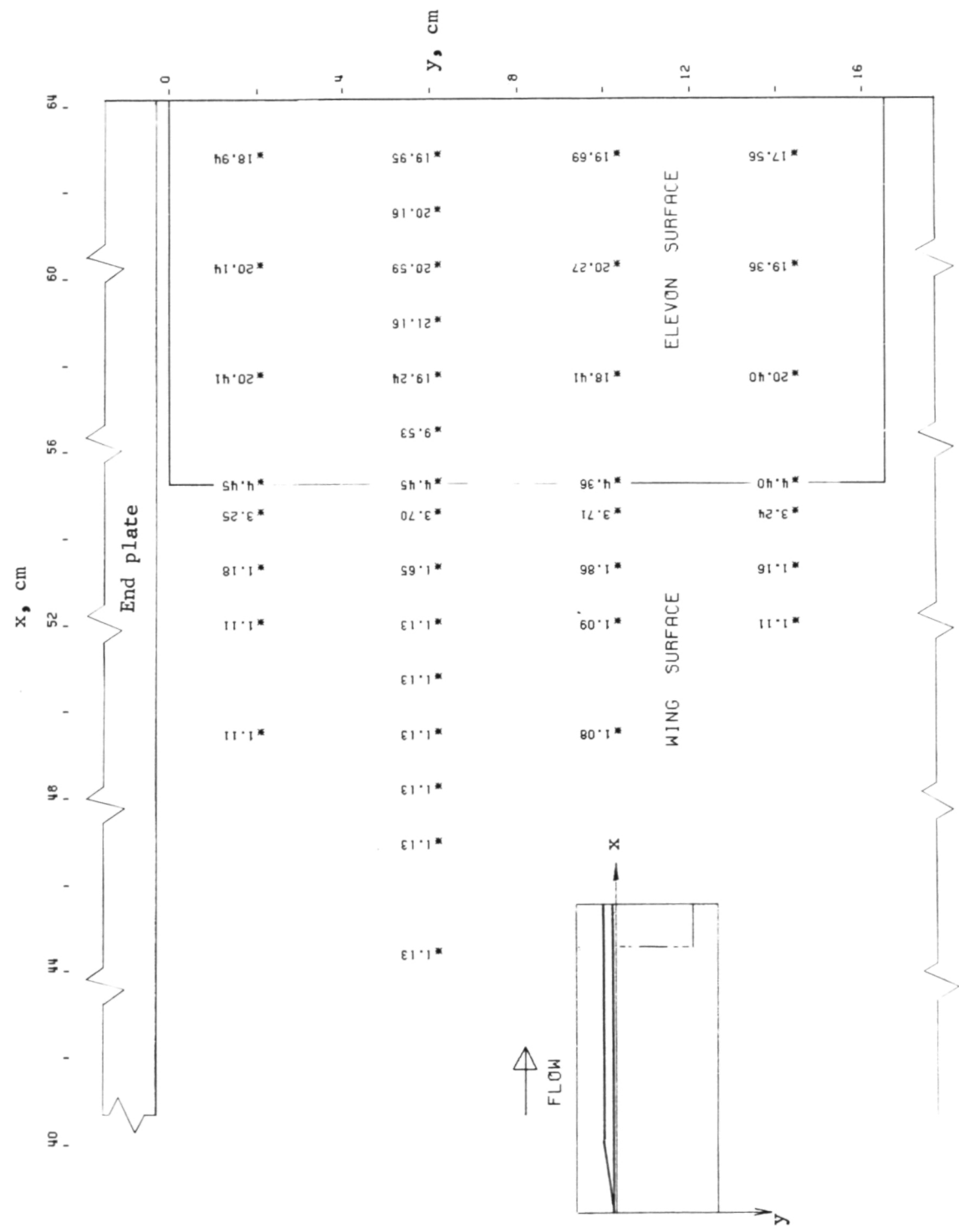


Figure 33.— Pressure-ratio (P) distribution on wing and elevon surfaces for $\Lambda = 0^\circ$, $\epsilon = 30^\circ$, and end plate attached 0.32 cm away from inboard edge of elevon.

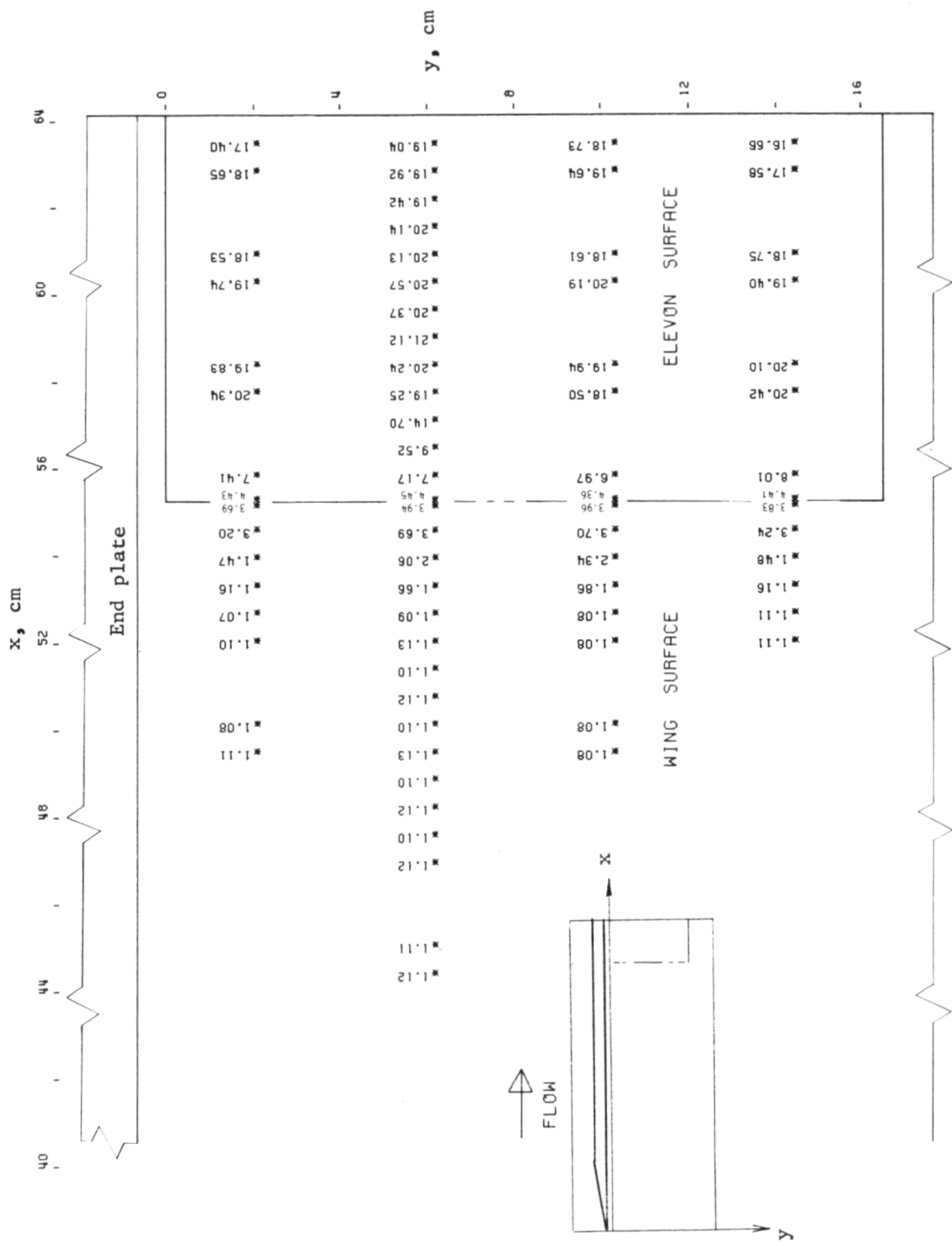


Figure 34.- Pressure-ratio (P) distribution on wing and elevon surfaces for $\Lambda = 0^\circ$, $\epsilon = 30^\circ$, and end plate attached 0.64 cm away from inboard edge of elevon.

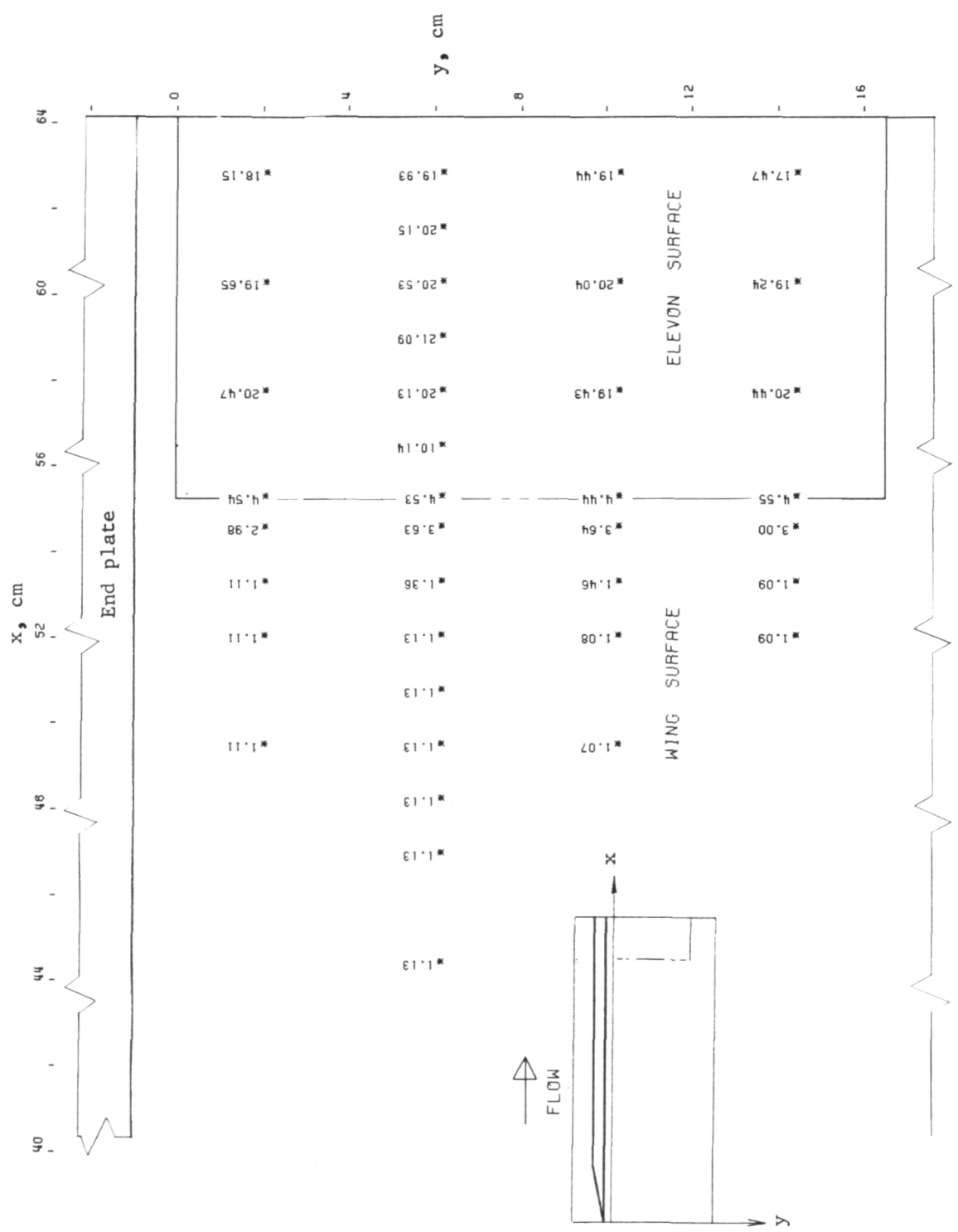
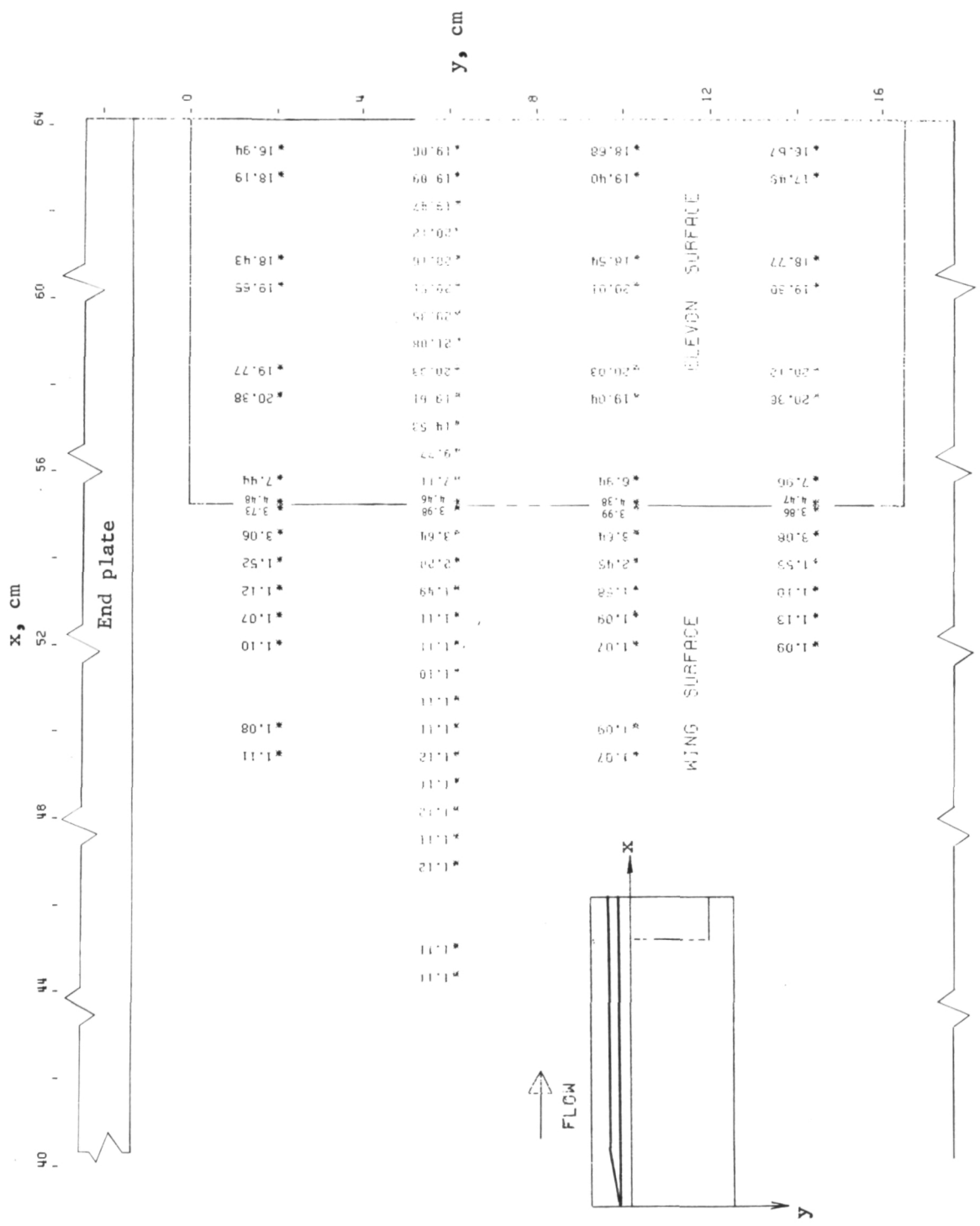


Figure 35.- Pressure-ratio (P) distribution on wing and elevon surfaces for $\Lambda = 0^\circ$, $\epsilon = 30^\circ$, and end plate attached 0.95 cm away from inboard edge of elevon.



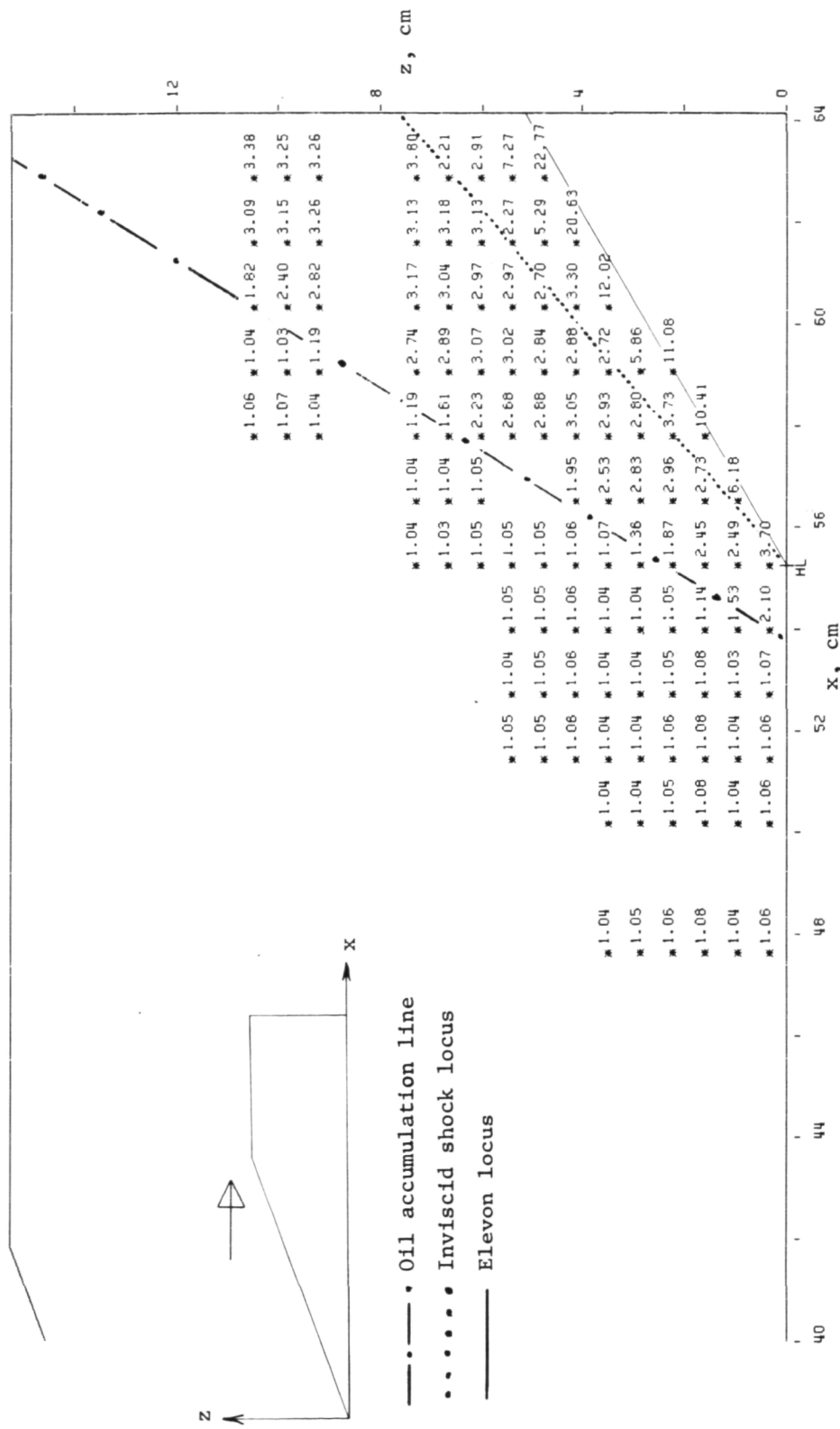


Figure 37.- Pressure-ratio (P) distribution on end-plate surface for $\Lambda = 0^\circ$ and $\epsilon = 30^\circ$.

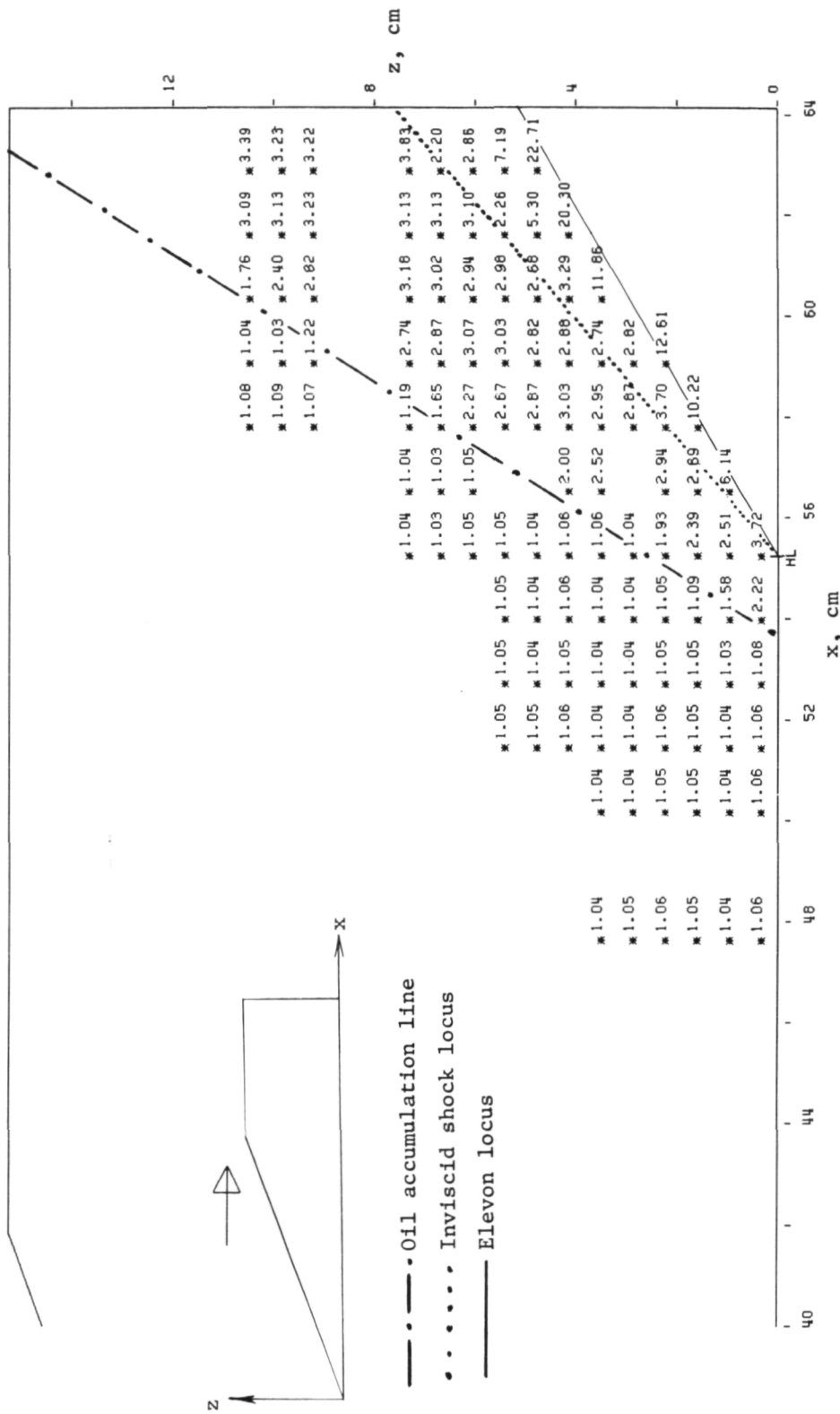
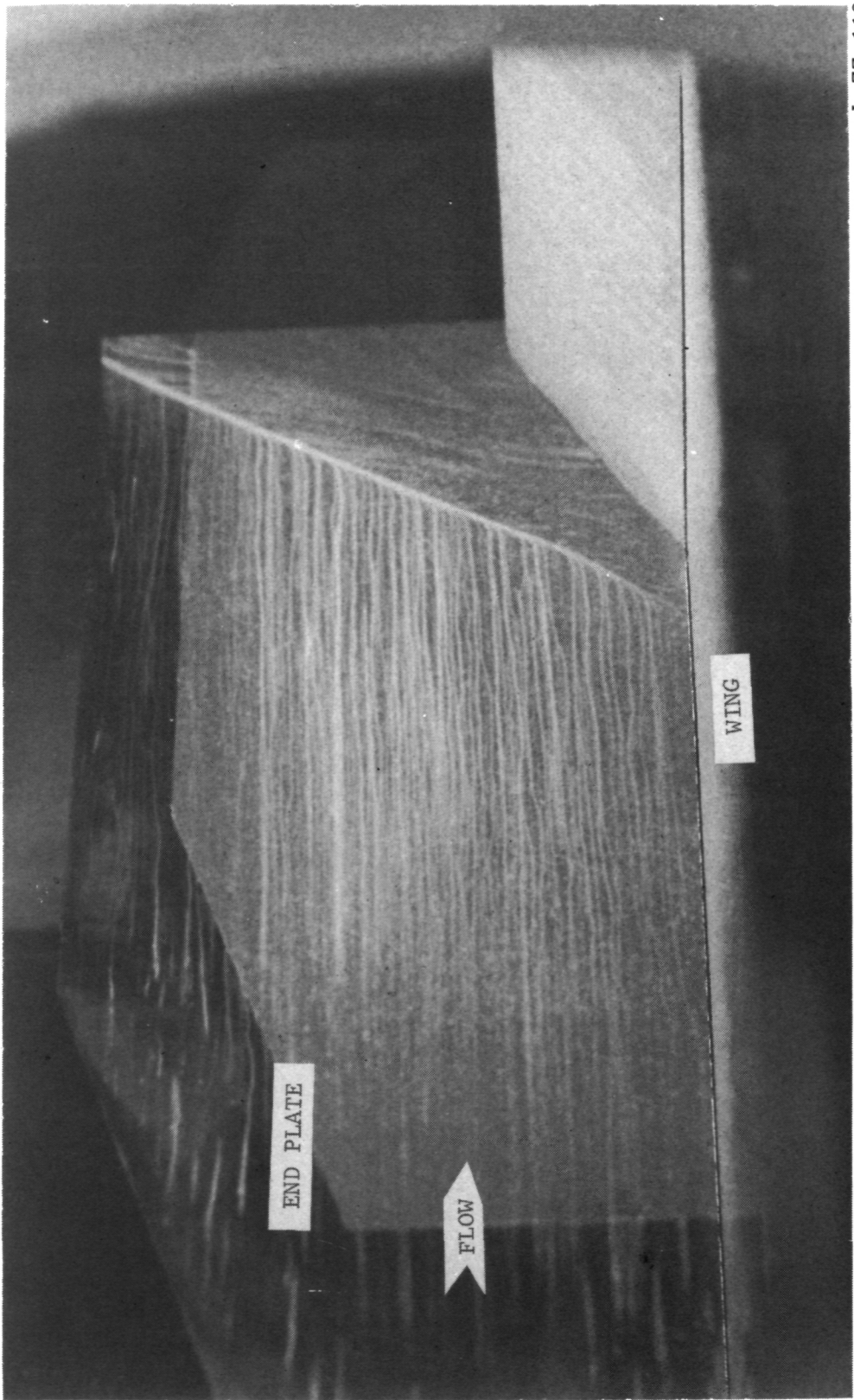


Figure 38.- Pressure-ratio (P) distribution on end-plate surface for $\Lambda = 0^\circ$, $\epsilon = 30^\circ$, and tip plate attached.

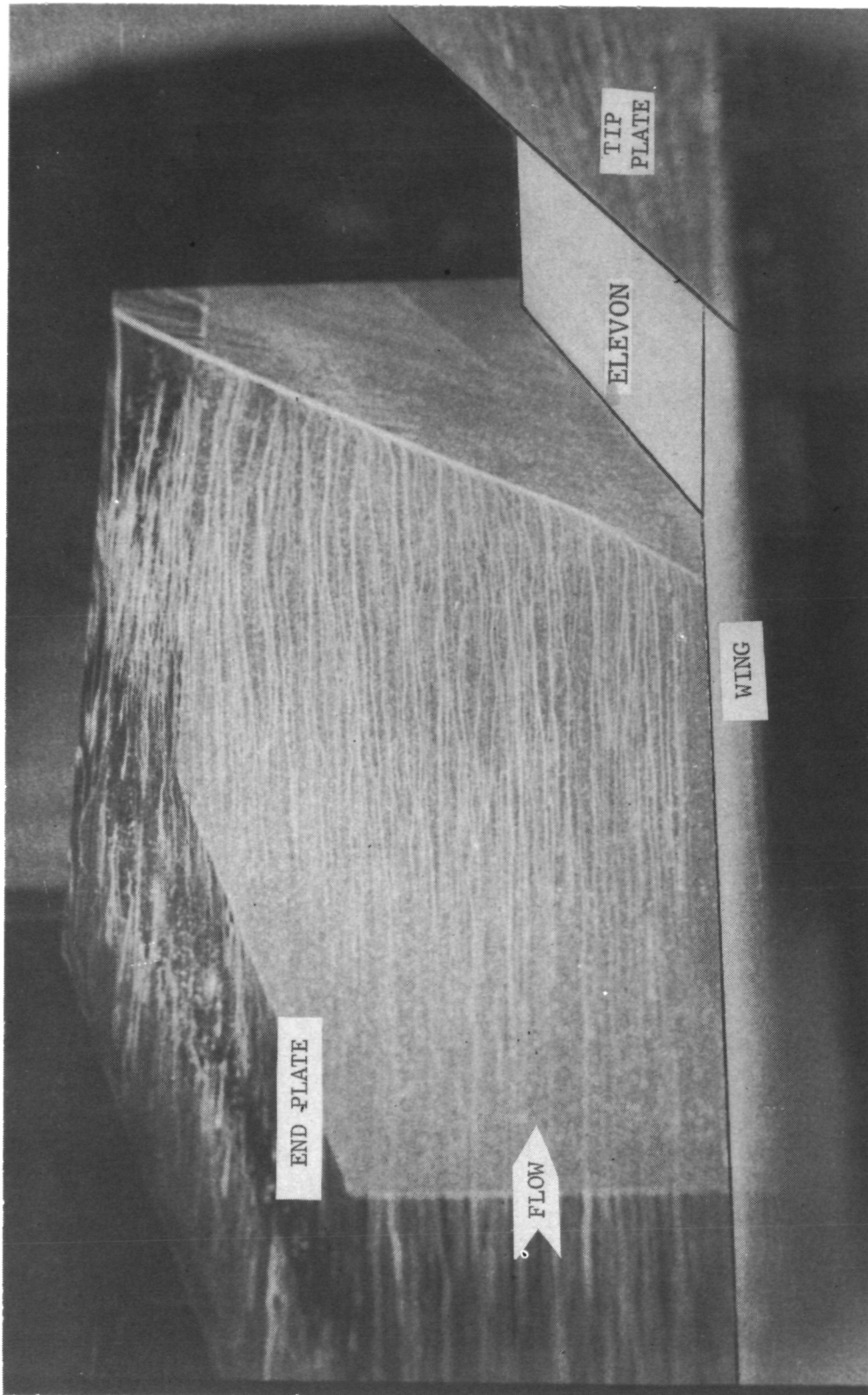
L-77-119

Figure 39.- Frame from surface-oil-film flow motion picture for $\Lambda = 0^\circ$, $\epsilon = 30^\circ$, and end plate attached.



L-77-120

Figure 40.- Frame from surface-oil-flow motion picture for $\Lambda = 0^\circ$,
 $\epsilon = 30^\circ$, end plate attached, and tip plate attached.



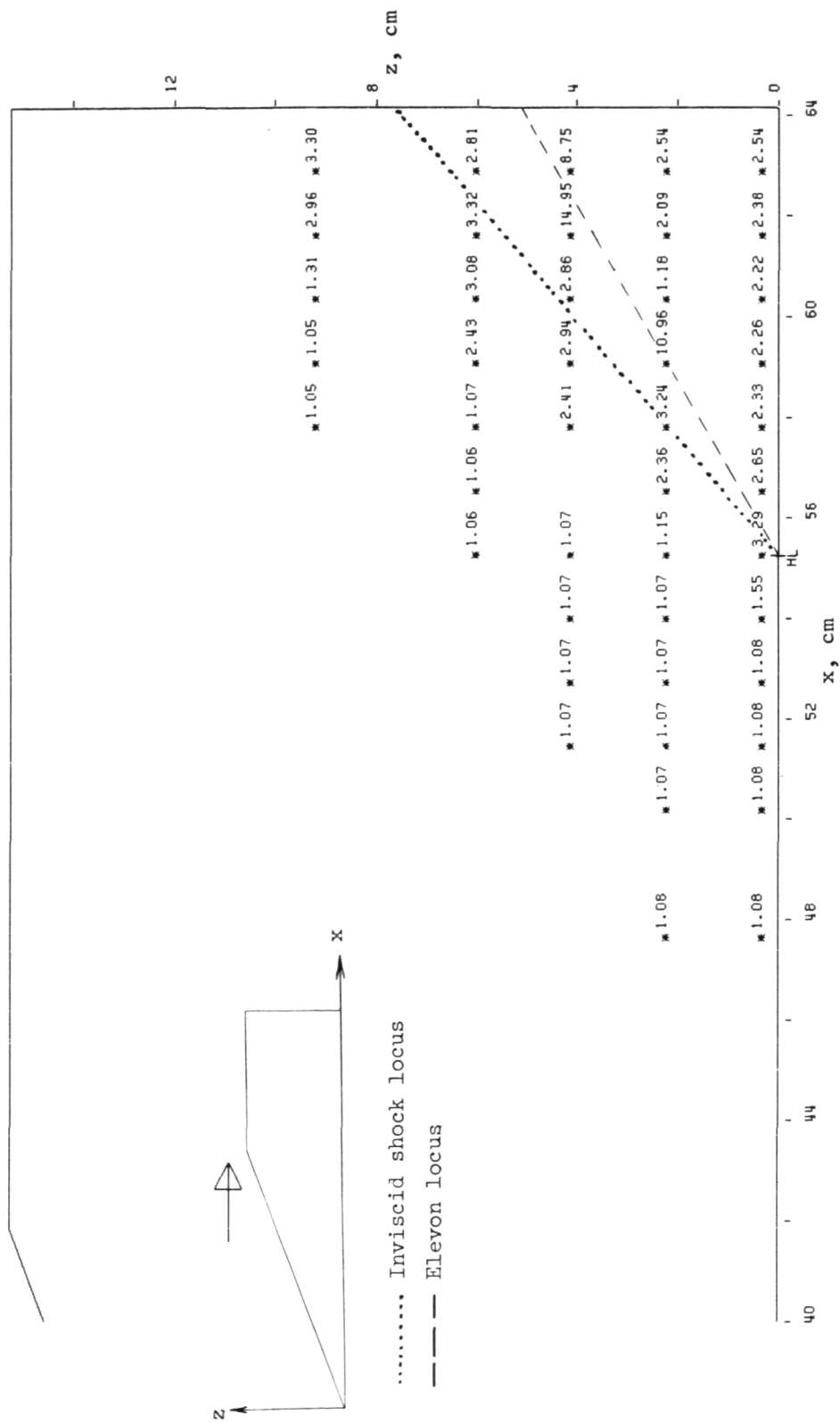


Figure 41.— Pressure-ratio (P) distribution on end-plate surface for $\Lambda = 0^\circ$, $\epsilon = 30^\circ$, and 0.32-cm gap between end plate and elevon.

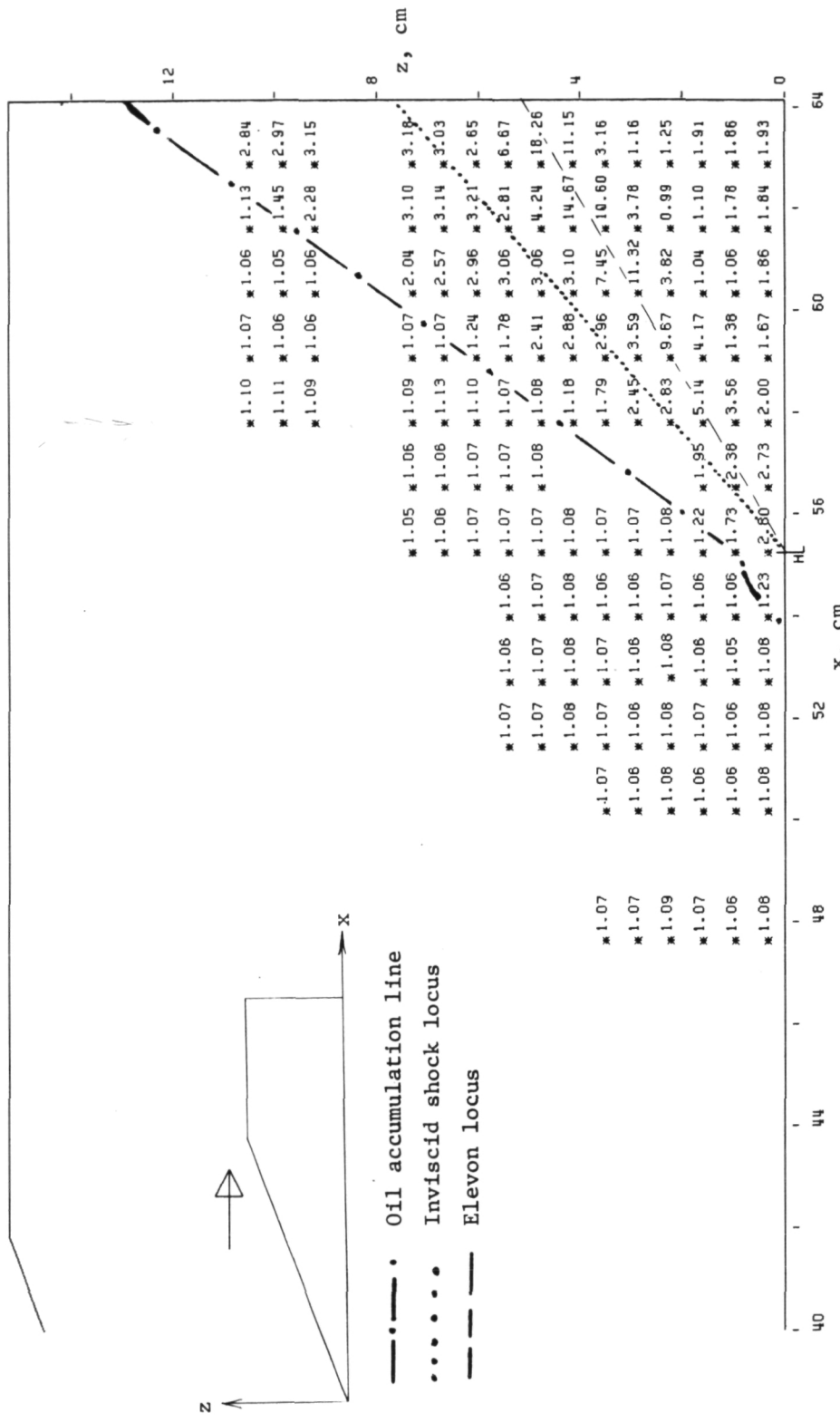


Figure 42.— Pressure-ratio (P) distribution on end-plate surface for $\Lambda = 0^\circ$, $\epsilon = 30^\circ$, and 0.64-cm gap between end plate and elevon.

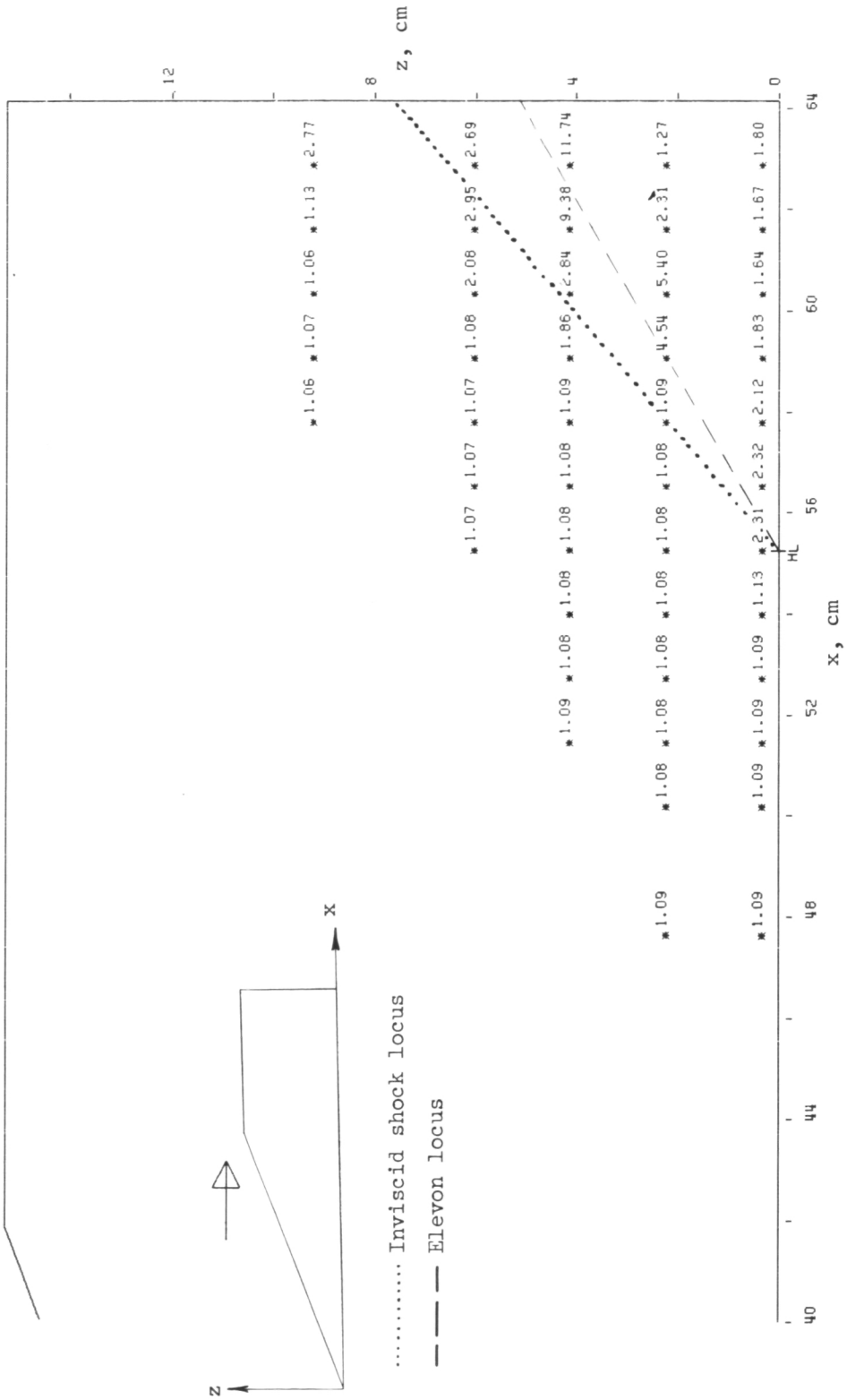


Figure 43.- Pressure-ratio (P) distribution on end-plate surface for $\Lambda = 0^\circ$, $\varepsilon = 30^\circ$, and 0.95-cm gap between end plate and elevon.

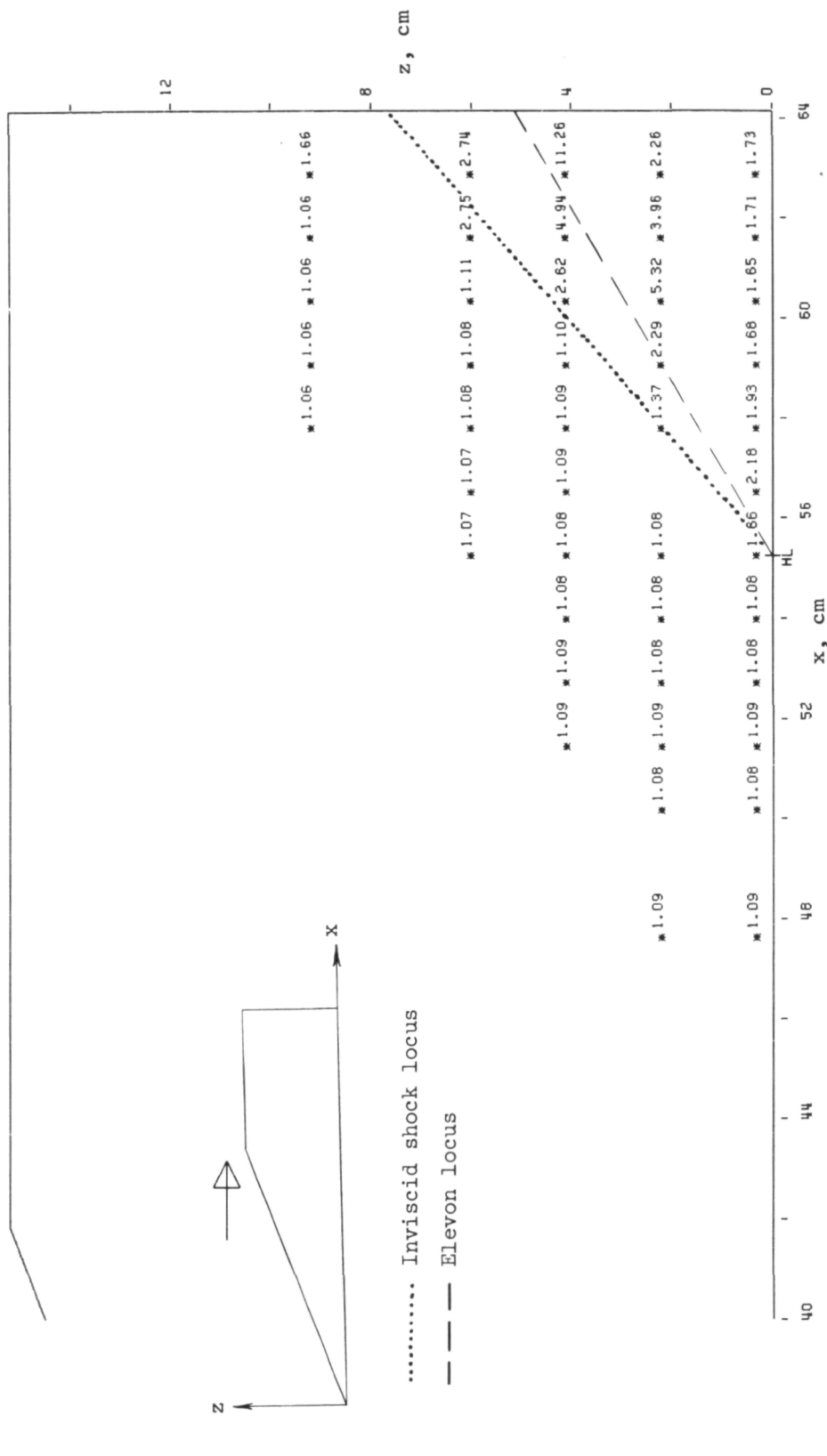
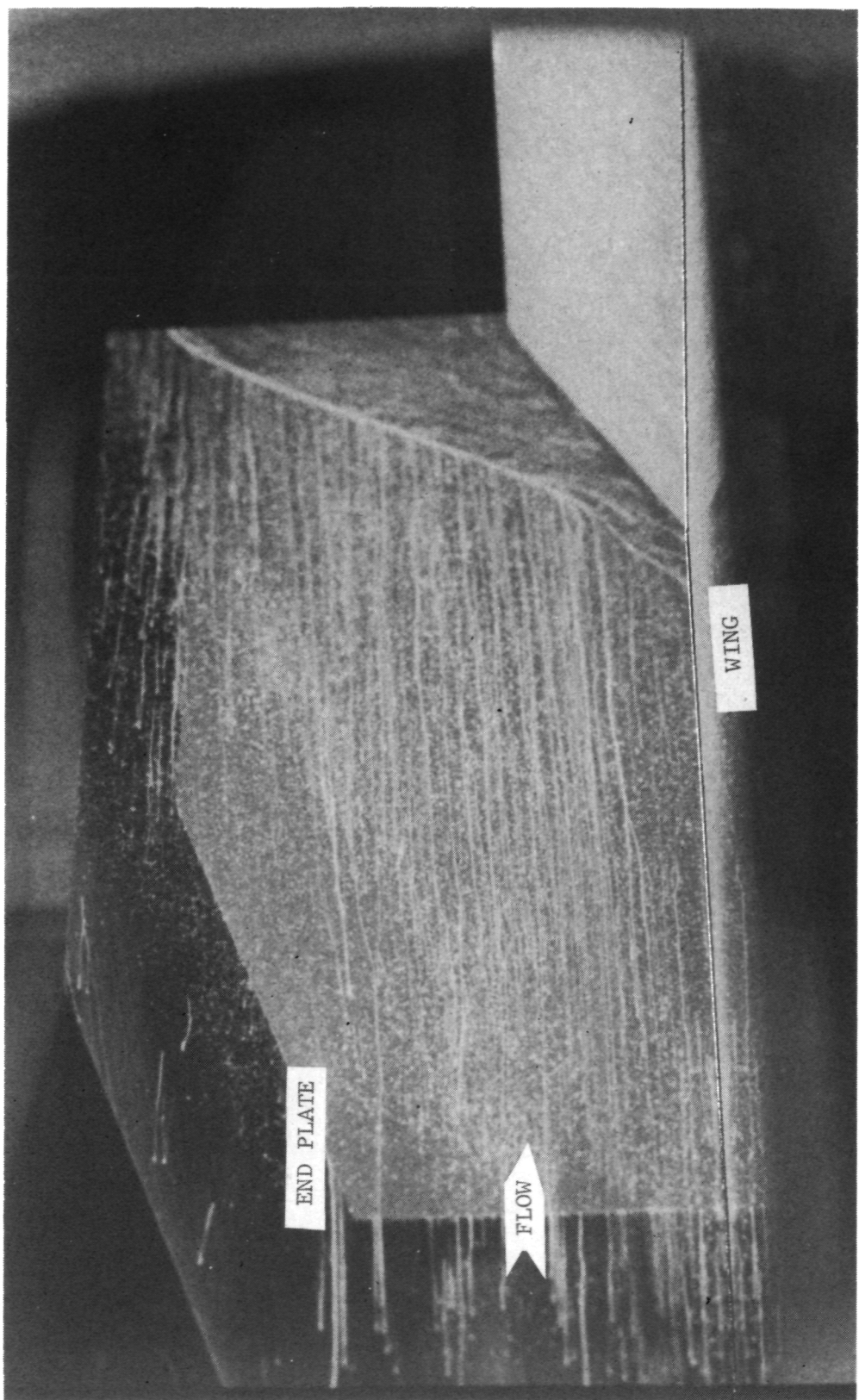
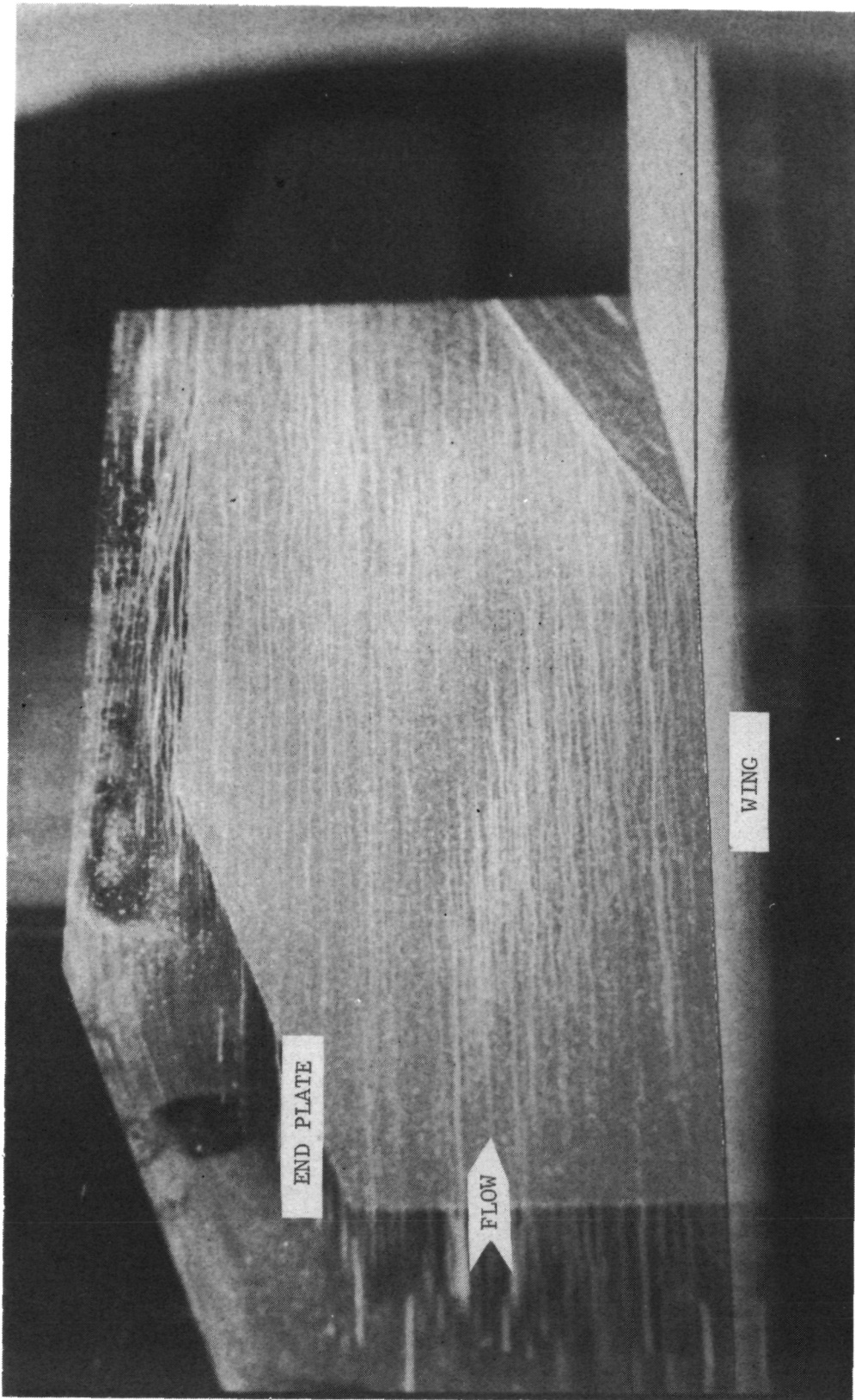


Figure 44.— Pressure-ratio (P) distribution on end-plate surface for $\Lambda = 0^\circ$, $\epsilon = 30^\circ$, and 1.27-cm gap between end plate and elevon.

L-77-121

Figure 45.- Frame from surface-oil-flow motion picture for $\Lambda = 0^\circ$, $\epsilon = 30^\circ$, and end plate attached with 0.64-cm gap between end plate and elevon.





L-77-122
Figure 46.- Frame from surface-oil-flow motion picture for $\Lambda = 50^\circ$,
 $\epsilon = 10^\circ$, and end plate attached.

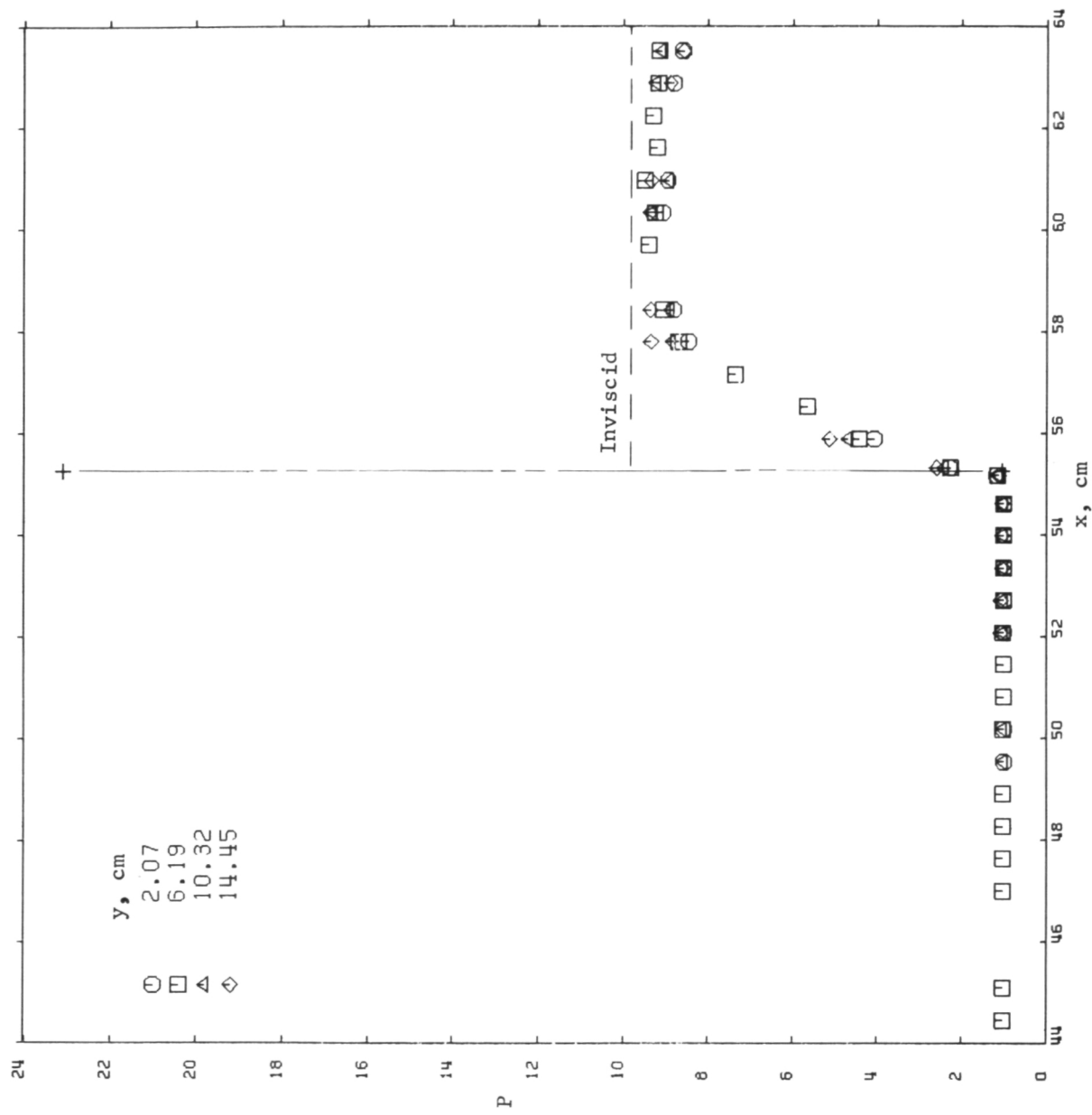


Figure 47.- Streamwise pressure-ratio distributions on wing and elevon surfaces for $\Lambda = 50^\circ$ and $\epsilon = 20^\circ$.

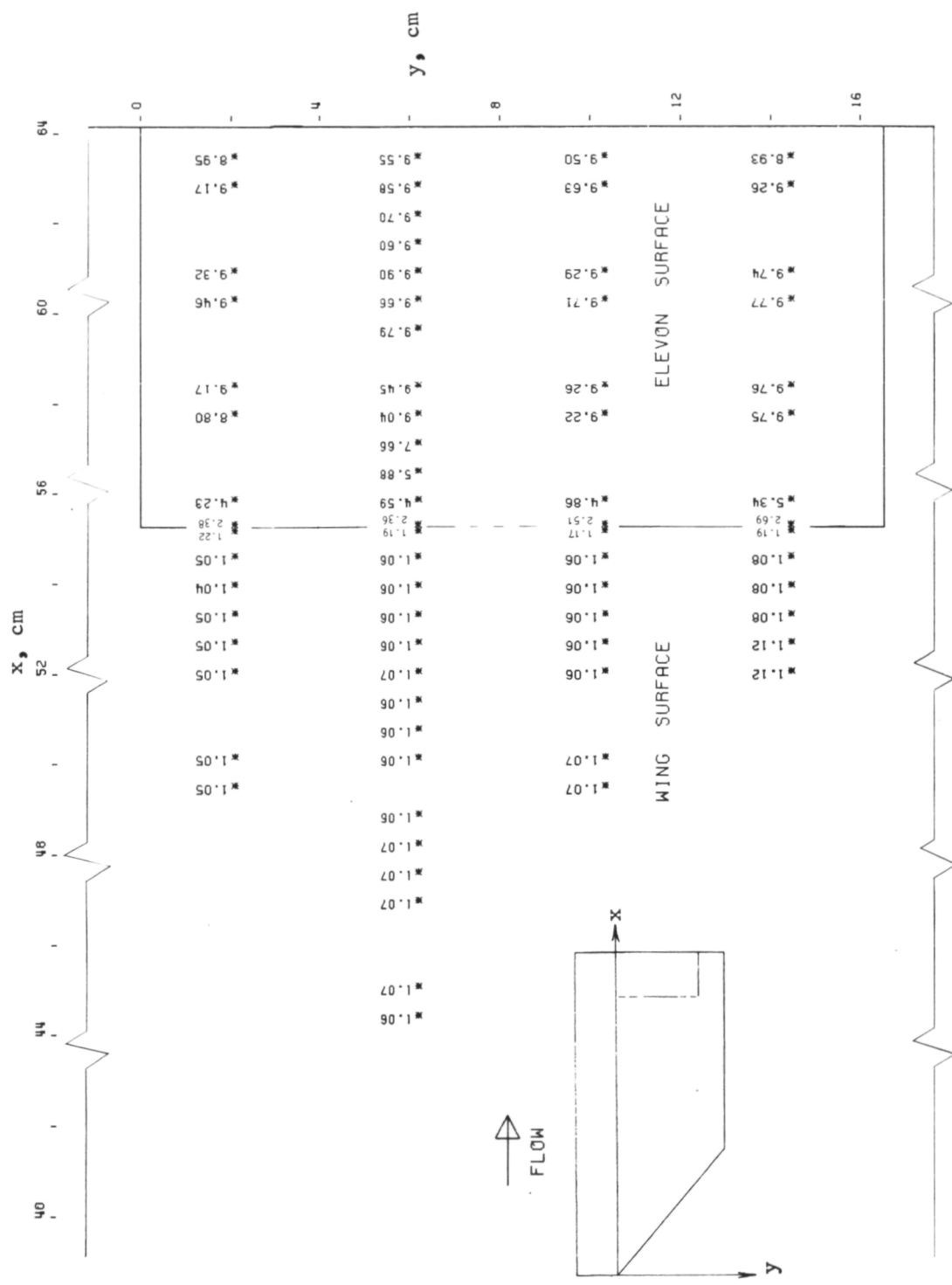


Figure 48.- Pressure-ratio (P) distribution on wing and elevon surfaces for $\Lambda = 50^\circ$ and $\epsilon = 20^\circ$.

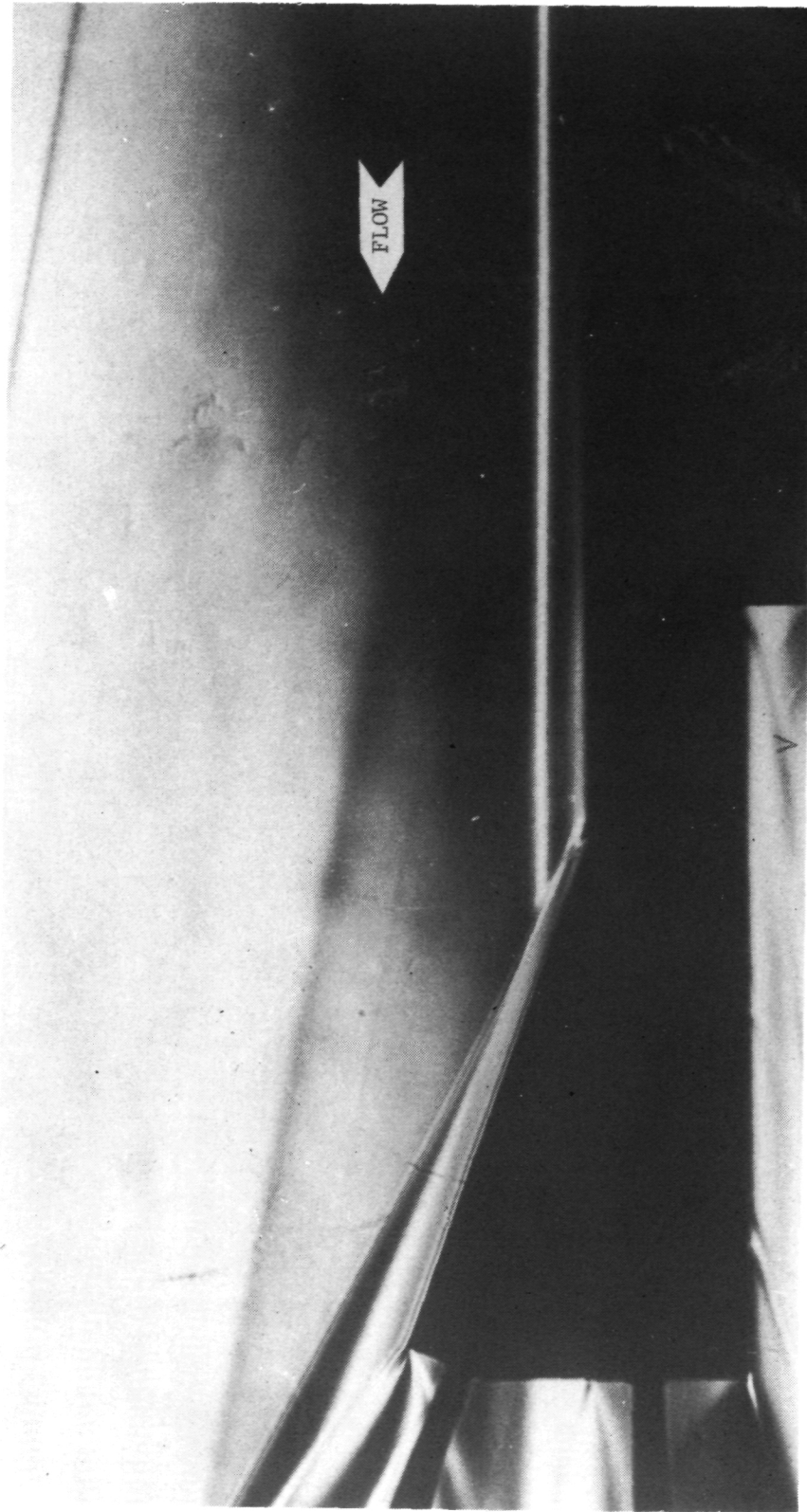


Figure 49.- Schlieren flow photograph for $\Lambda = 50^\circ$ and $\epsilon = 20^\circ$.
L-77-123

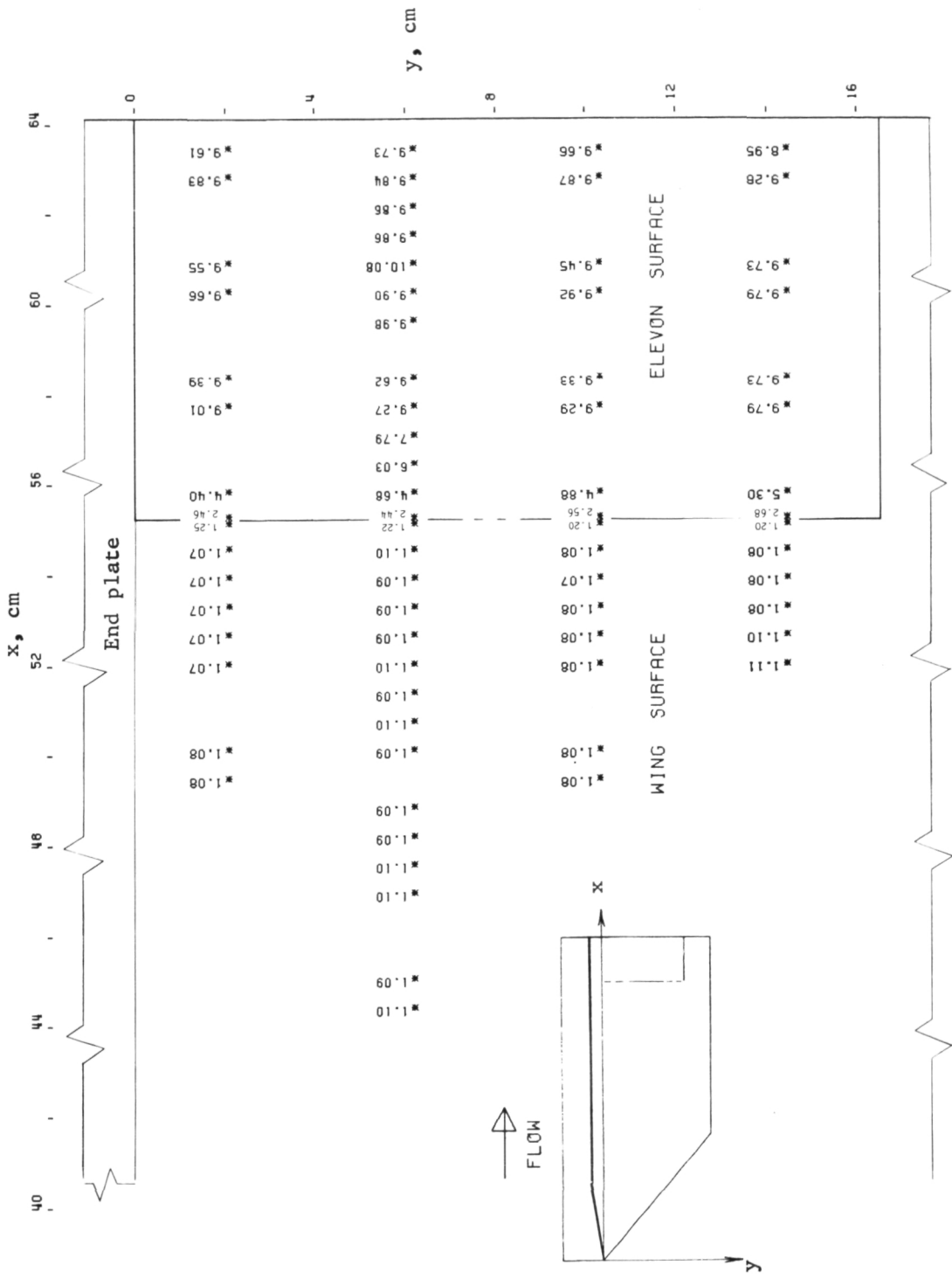


Figure 50.- Pressure-ratio (P) distribution on wing and elevon surfaces for $\Lambda = 50^\circ$, $\epsilon = 20^\circ$, and end plate attached.

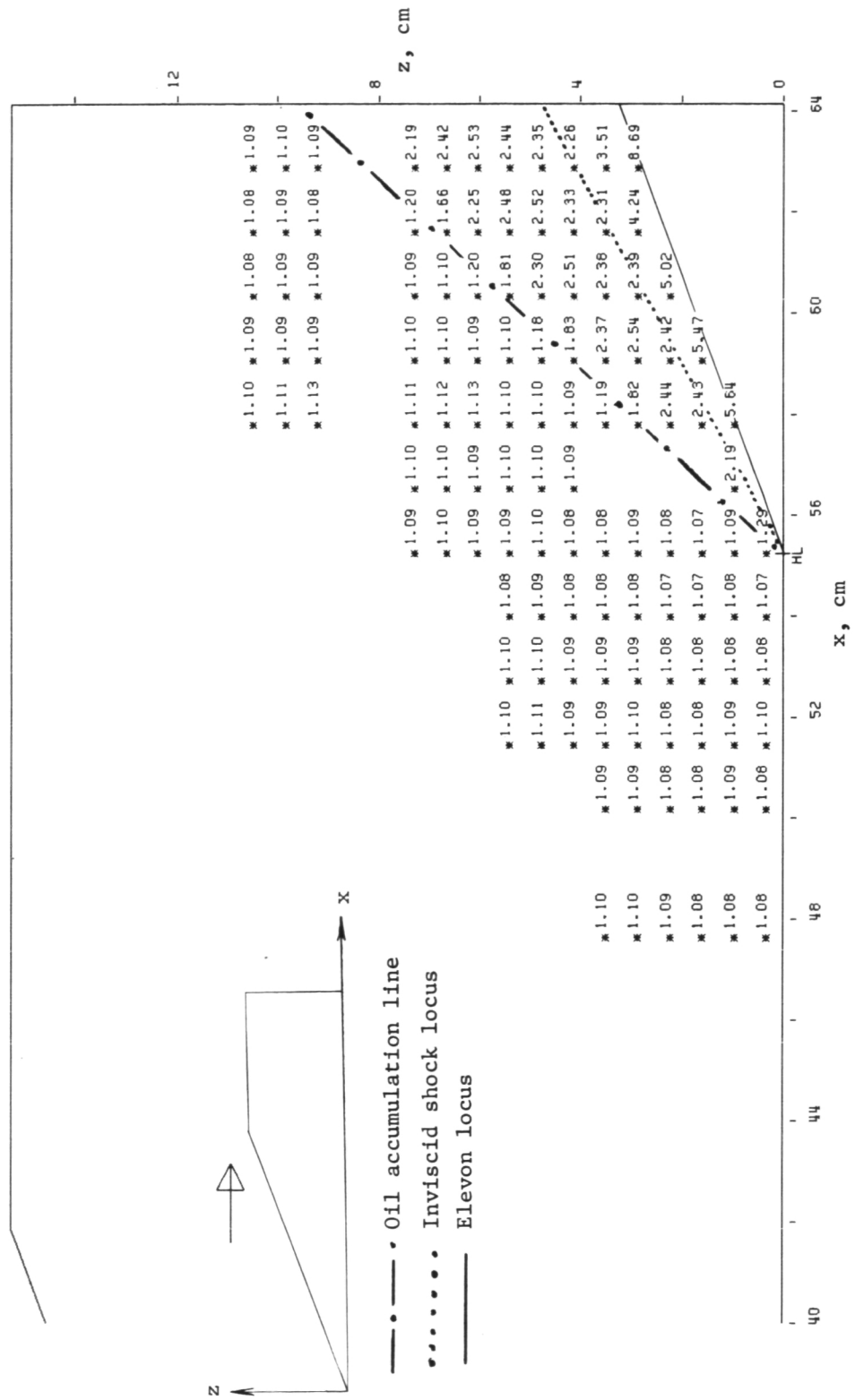
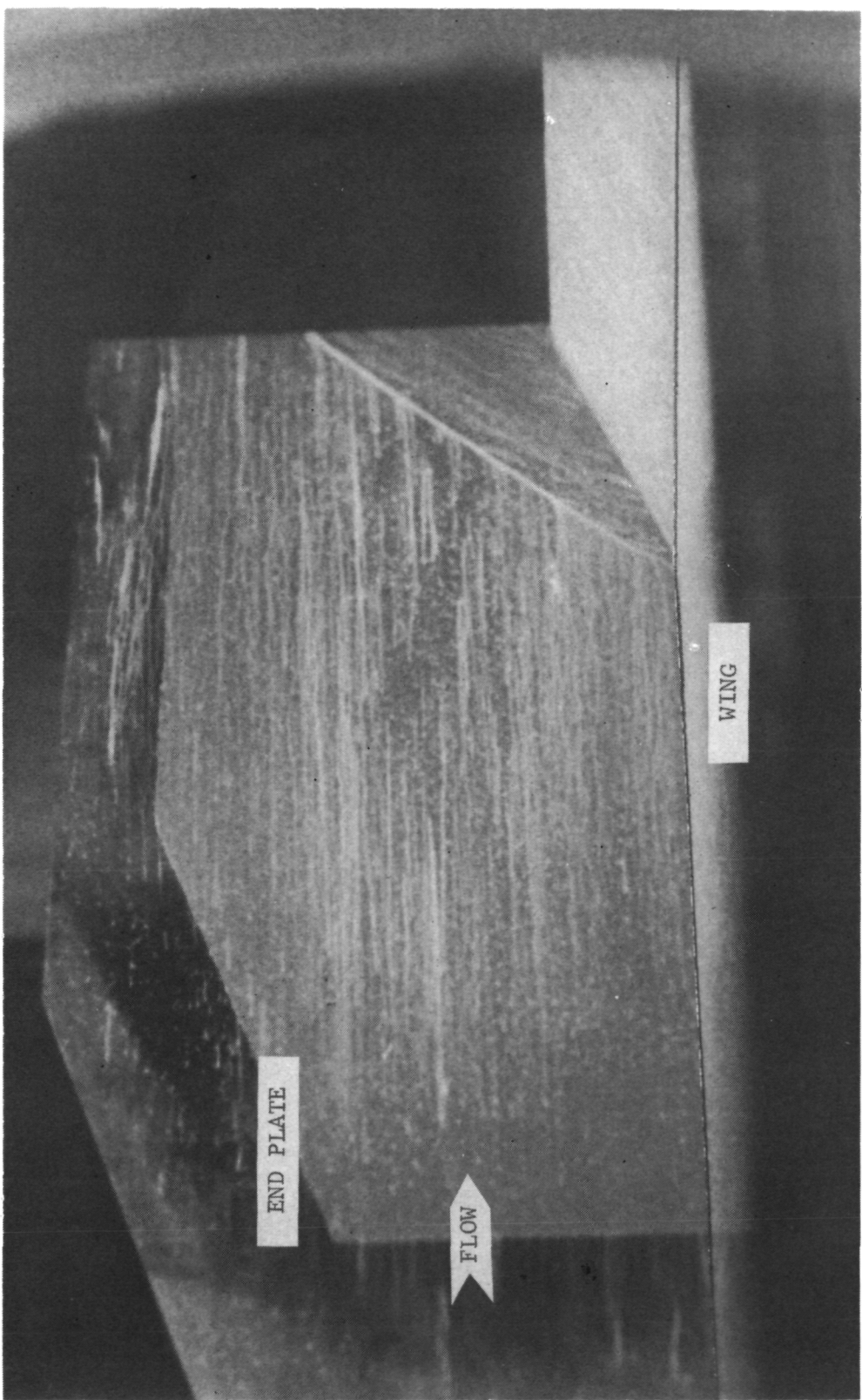


Figure 51.— Pressure-ratio (P) distribution on end-plate surface for $\Lambda = 50^\circ$ and $\epsilon = 20^\circ$.

L-77-124

Figure 52.- Frame from surface-oil-flow motion picture for $\Lambda = 50^\circ$,
 $\epsilon = 20^\circ$, and end plate attached.



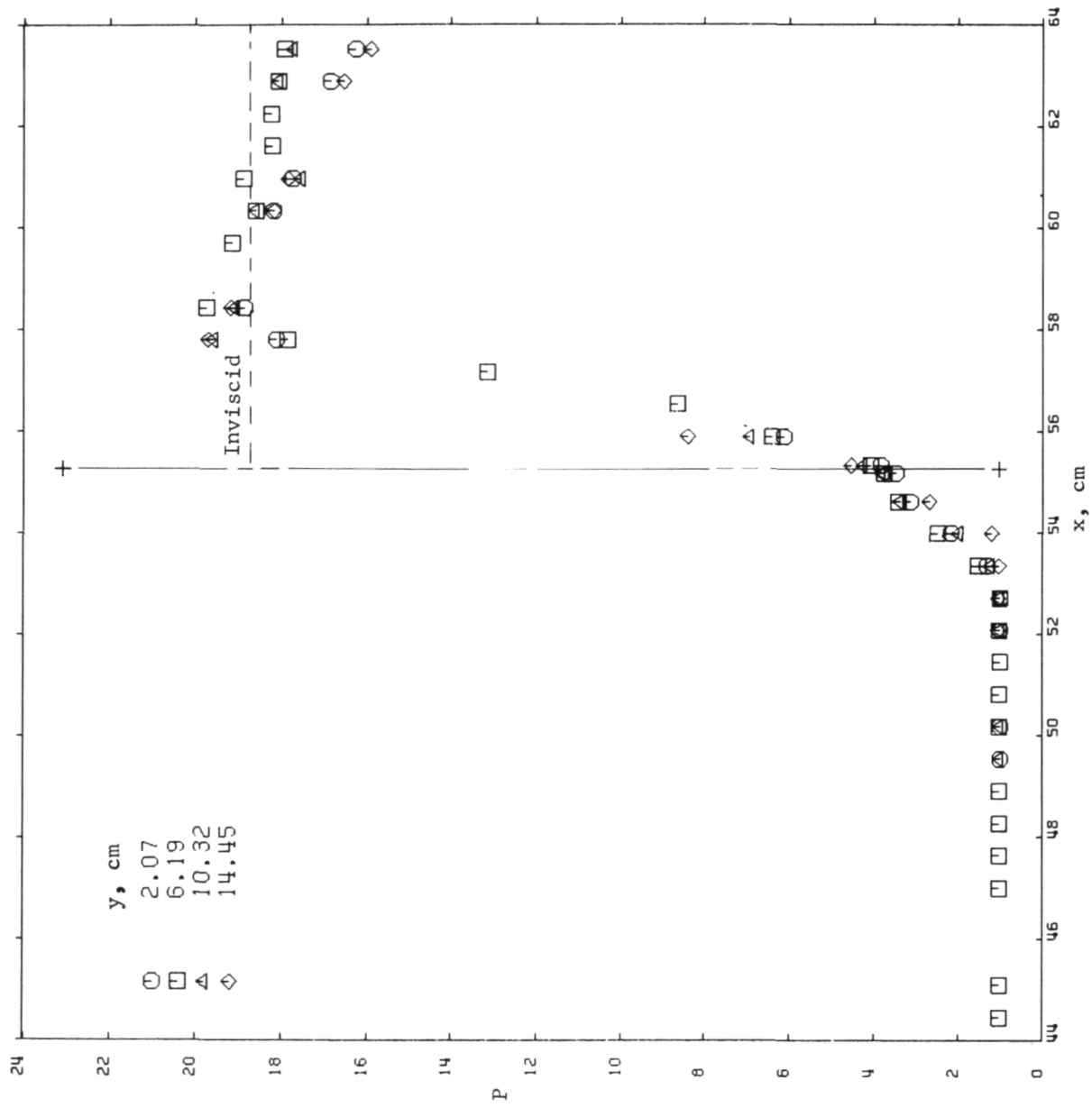


Figure 53.- Streamwise pressure-ratio distributions on wing and elevon surfaces for $\Lambda = 50^\circ$ and $\epsilon = 30^\circ$.

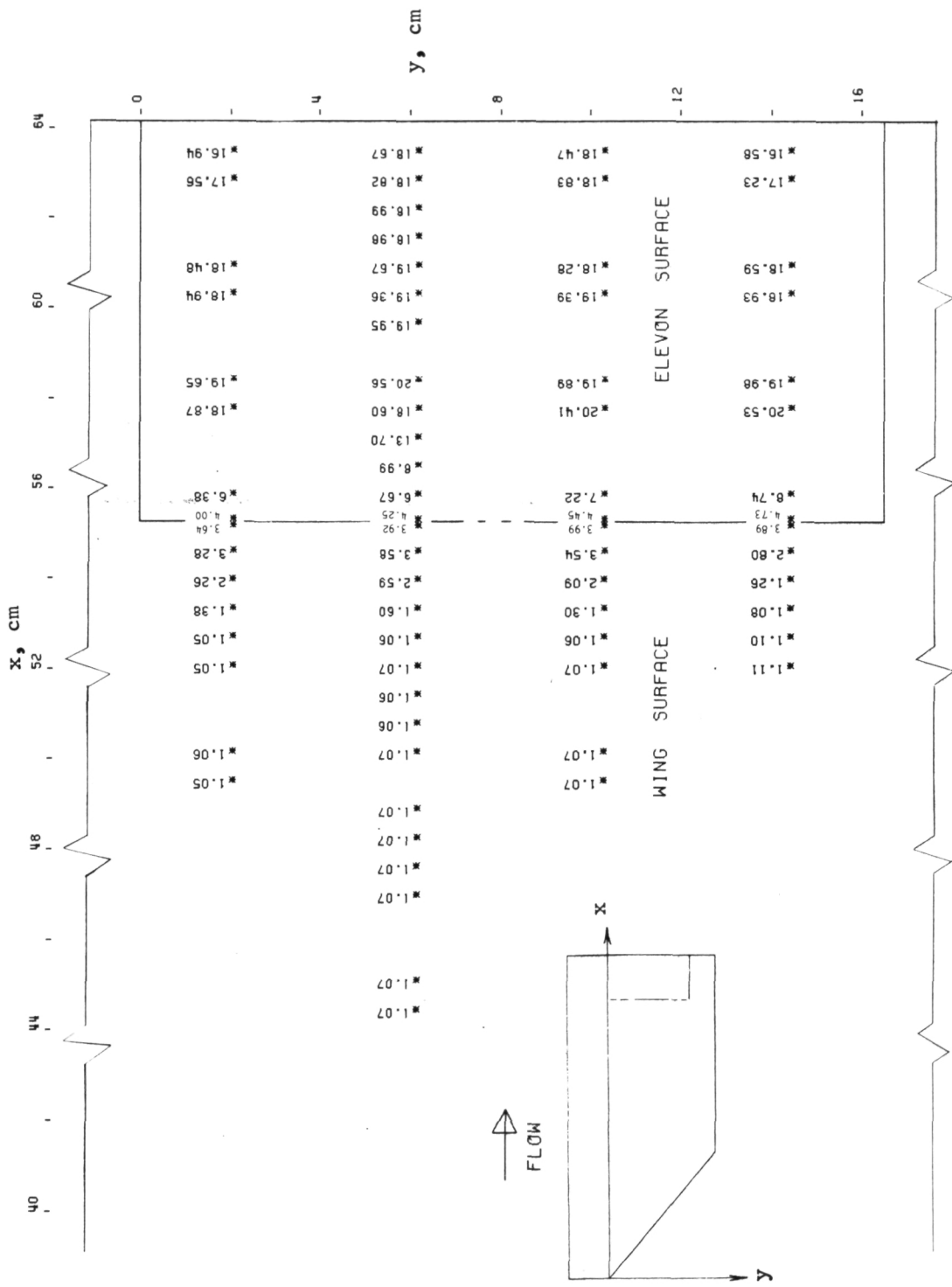
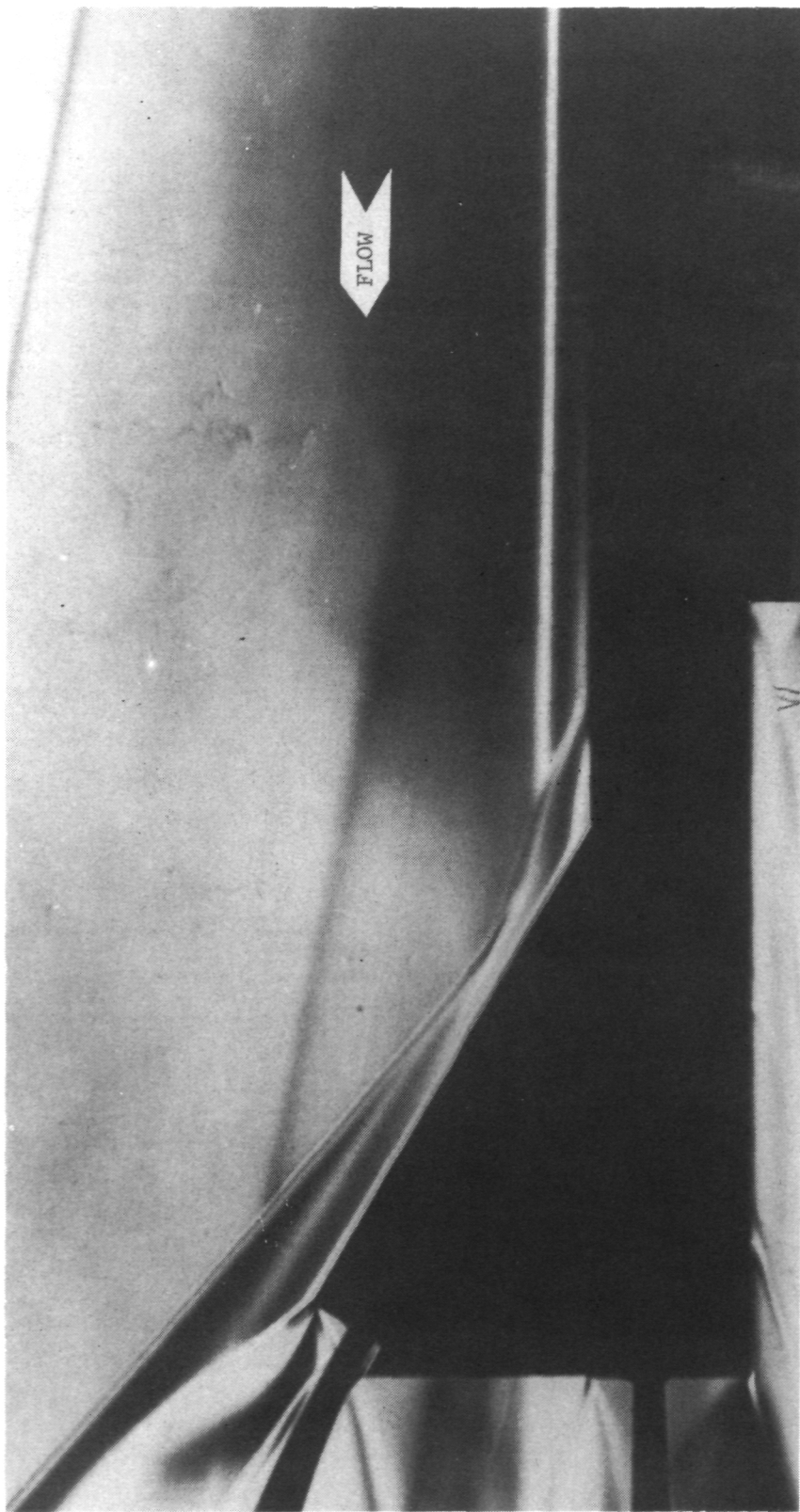
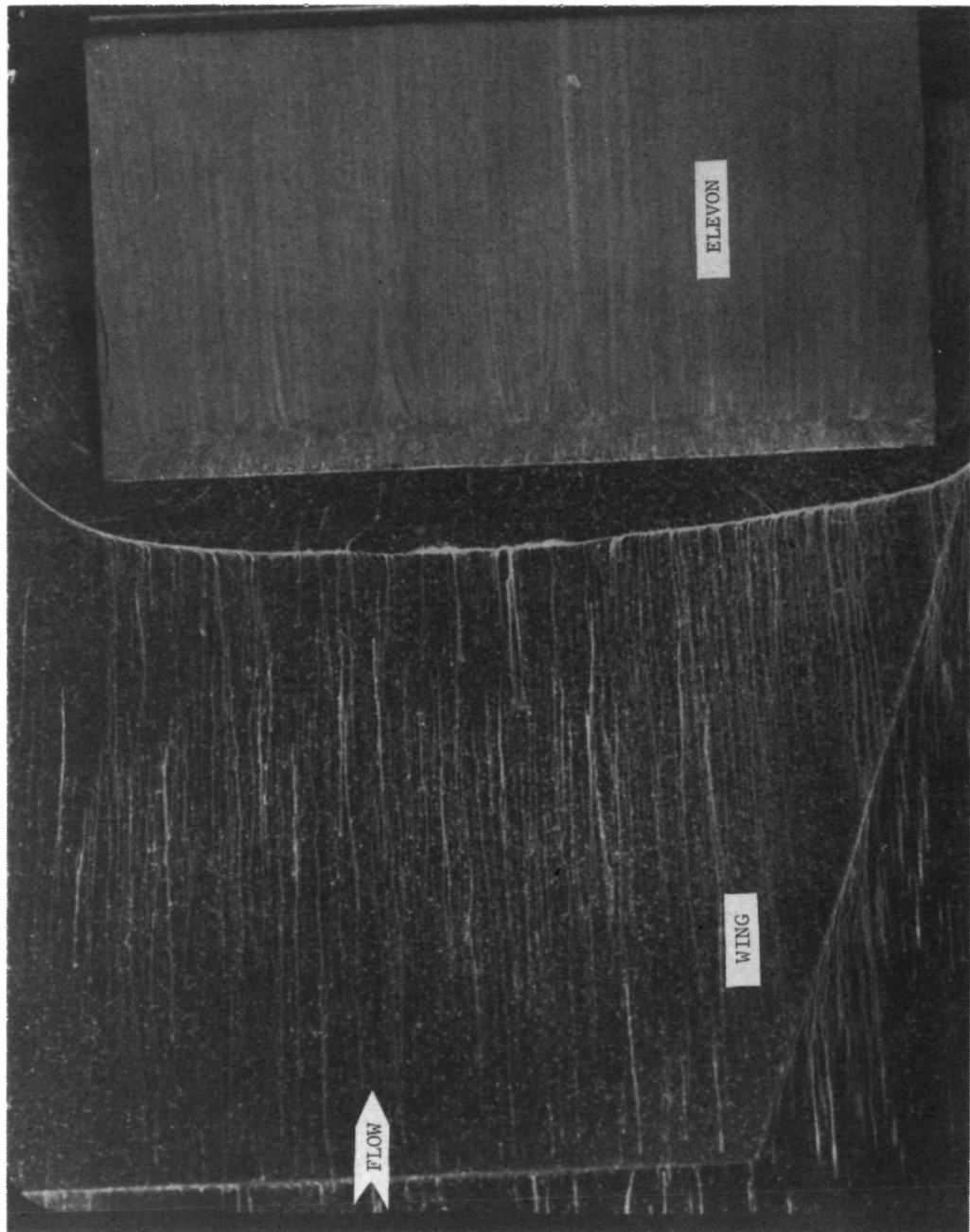


Figure 54.- Pressure-ratio (P) distribution on wing and elevon surfaces for $\Lambda = 50^\circ$ and $\epsilon = 30^\circ$.

L-77-125

Figure 55.- Schlieren flow photograph for $\Lambda = 50^\circ$ and $\epsilon = 30^\circ$.





L-77-126

Figure 56.- Frame from surface-oil-flow motion picture
for $\Lambda = 500$ and $\epsilon = 30^\circ$.

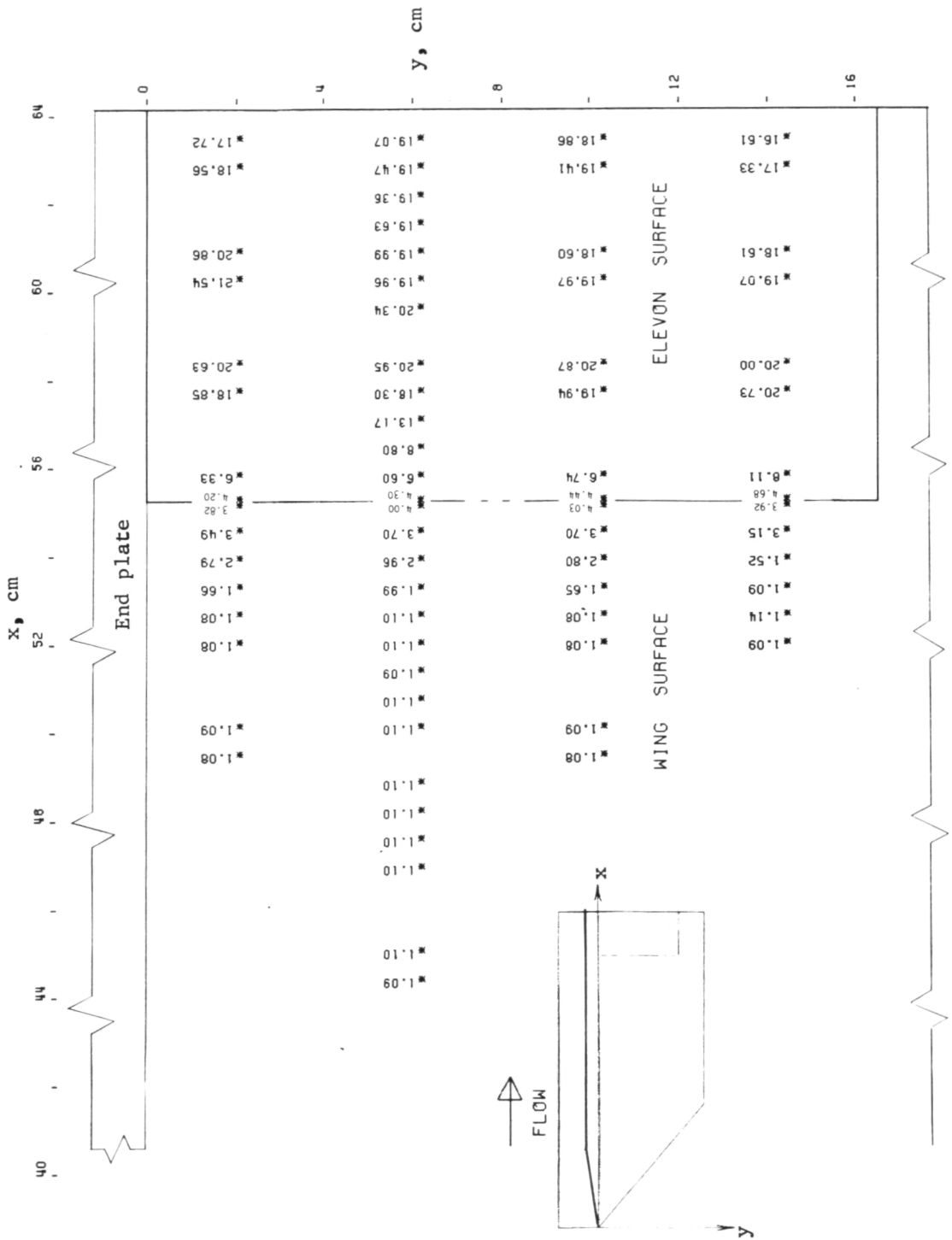
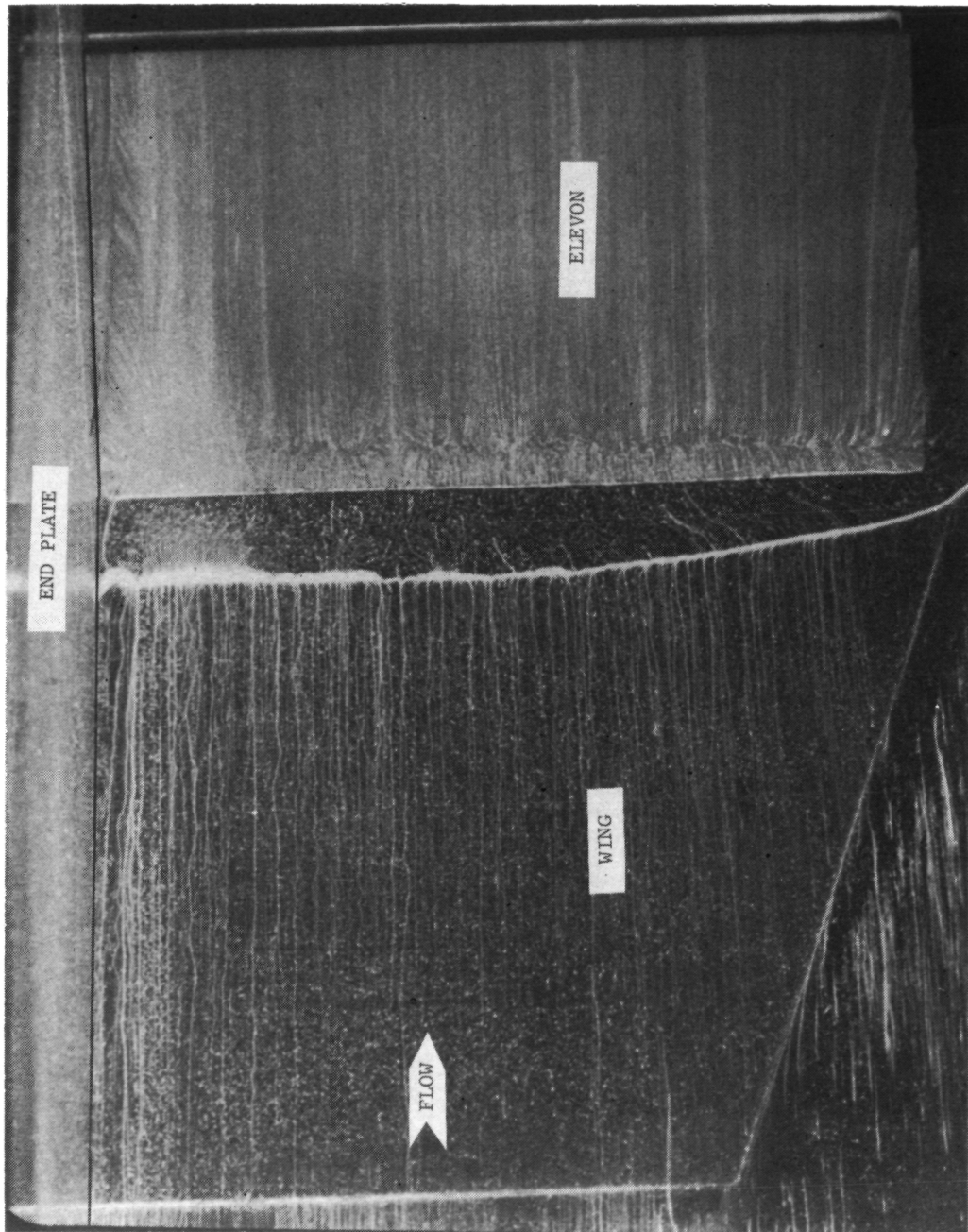


Figure 57.- Pressure-ratio (P) distribution on wing and elevon surfaces for $\Lambda = 50^\circ$, $\epsilon = 30^\circ$, and end plate attached.



L-77-127
Figure 58.- Frame from surface-oil-flow motion picture for $\Lambda = 50^\circ$,
 $\epsilon = 30^\circ$, and end plate attached.

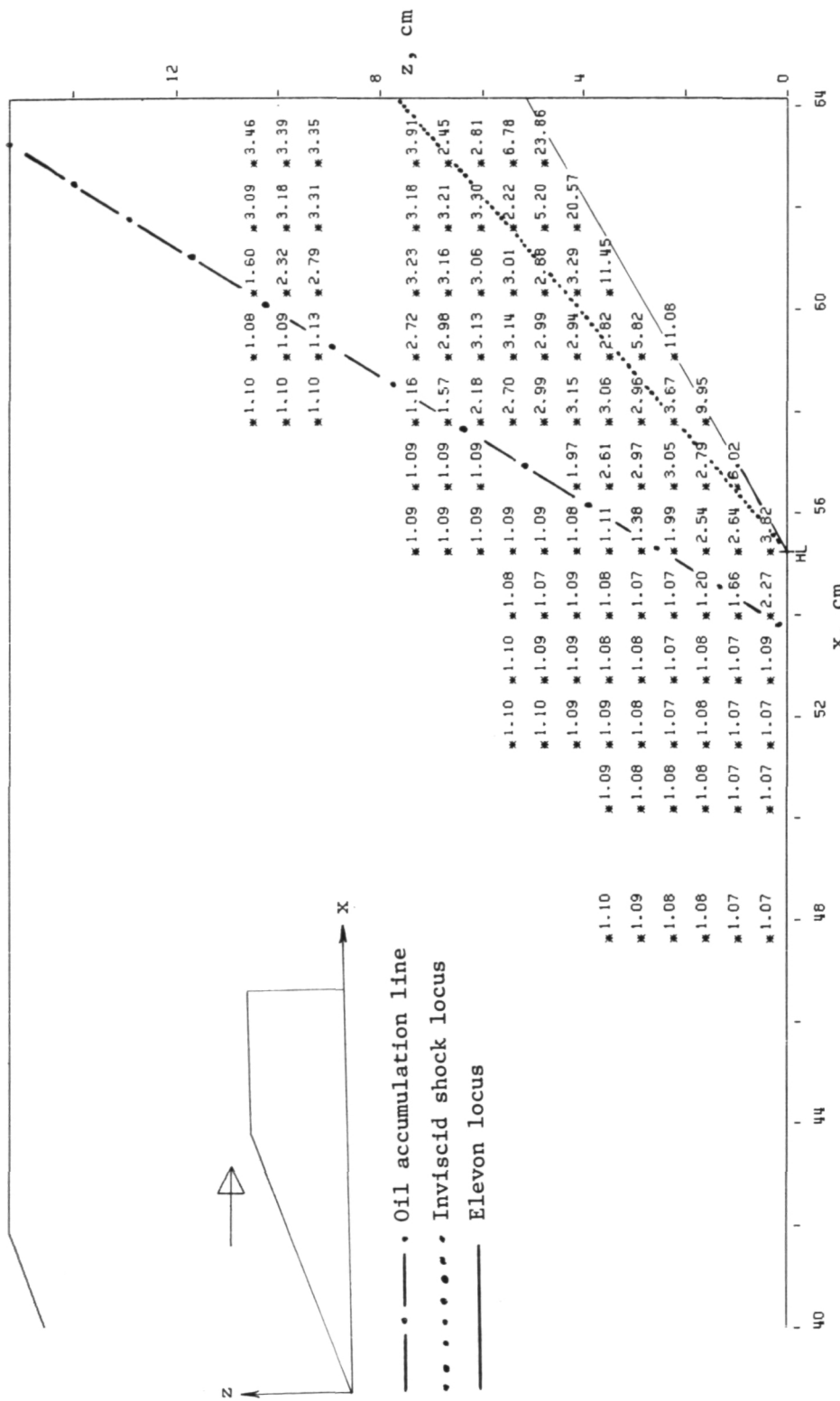
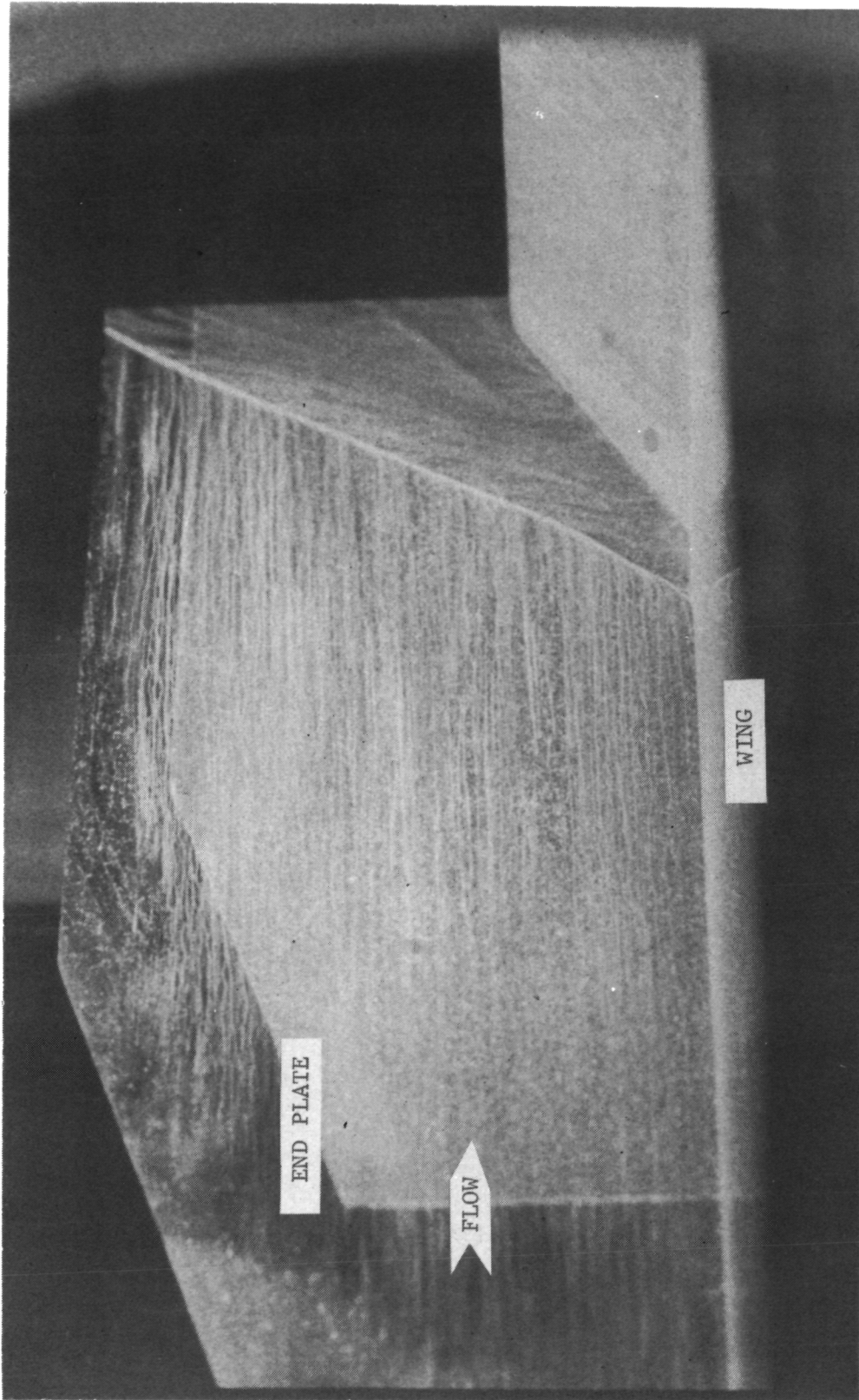


Figure 59.— Pressure-ratio (P) distribution on end-plate surface
for $\Lambda = 50^\circ$ and $\epsilon = 30^\circ$.

L-77-128

Figure 60.- Frame from surface-oil-flow motion picture for $\Lambda = 50^\circ$, $\epsilon = 30^\circ$, and end plate attached.



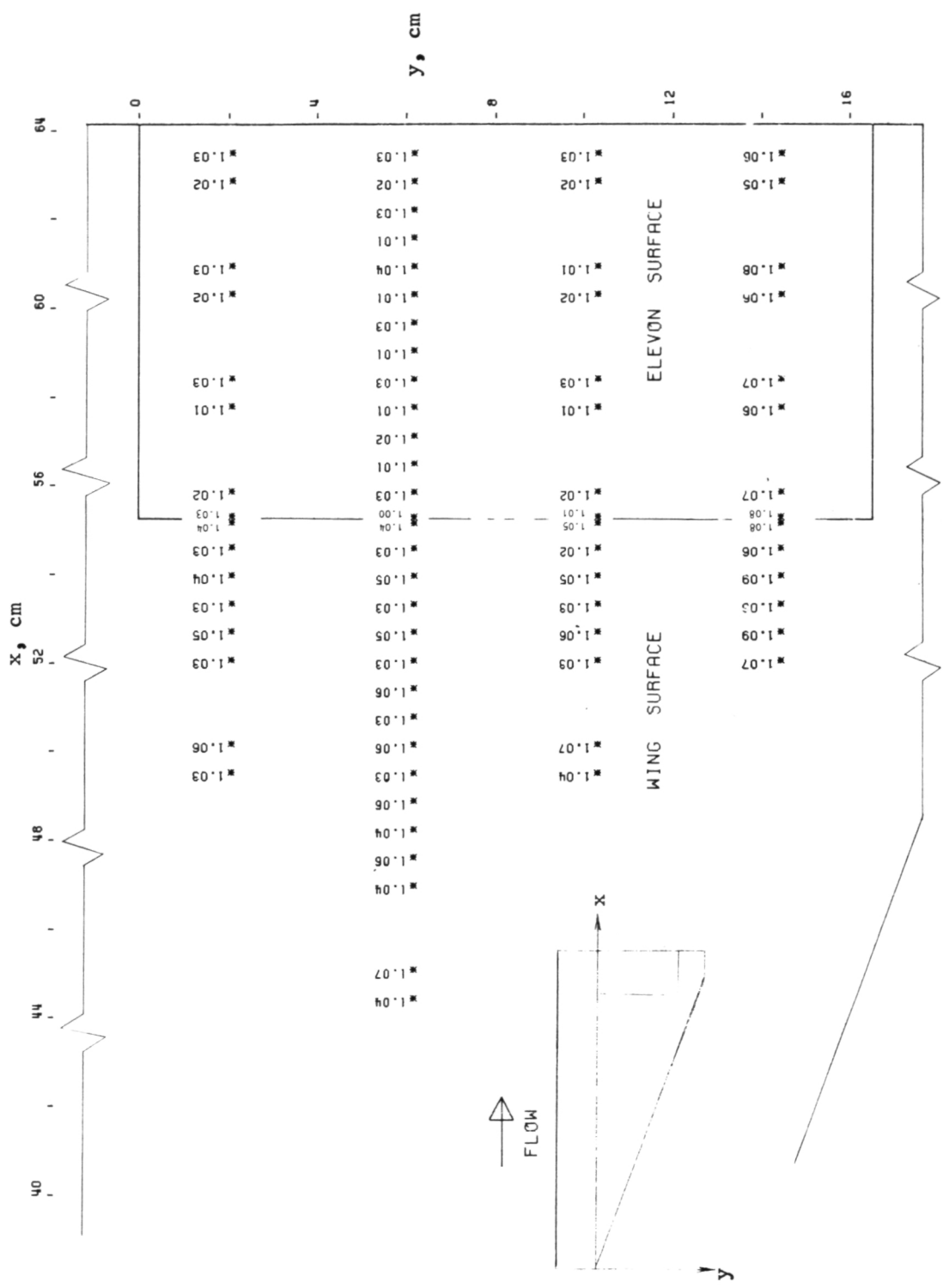


Figure 61.— Pressure-ratio (P) distribution on wing and elevon surfaces for $\Lambda = 70^\circ$ and $\epsilon = 0^\circ$.

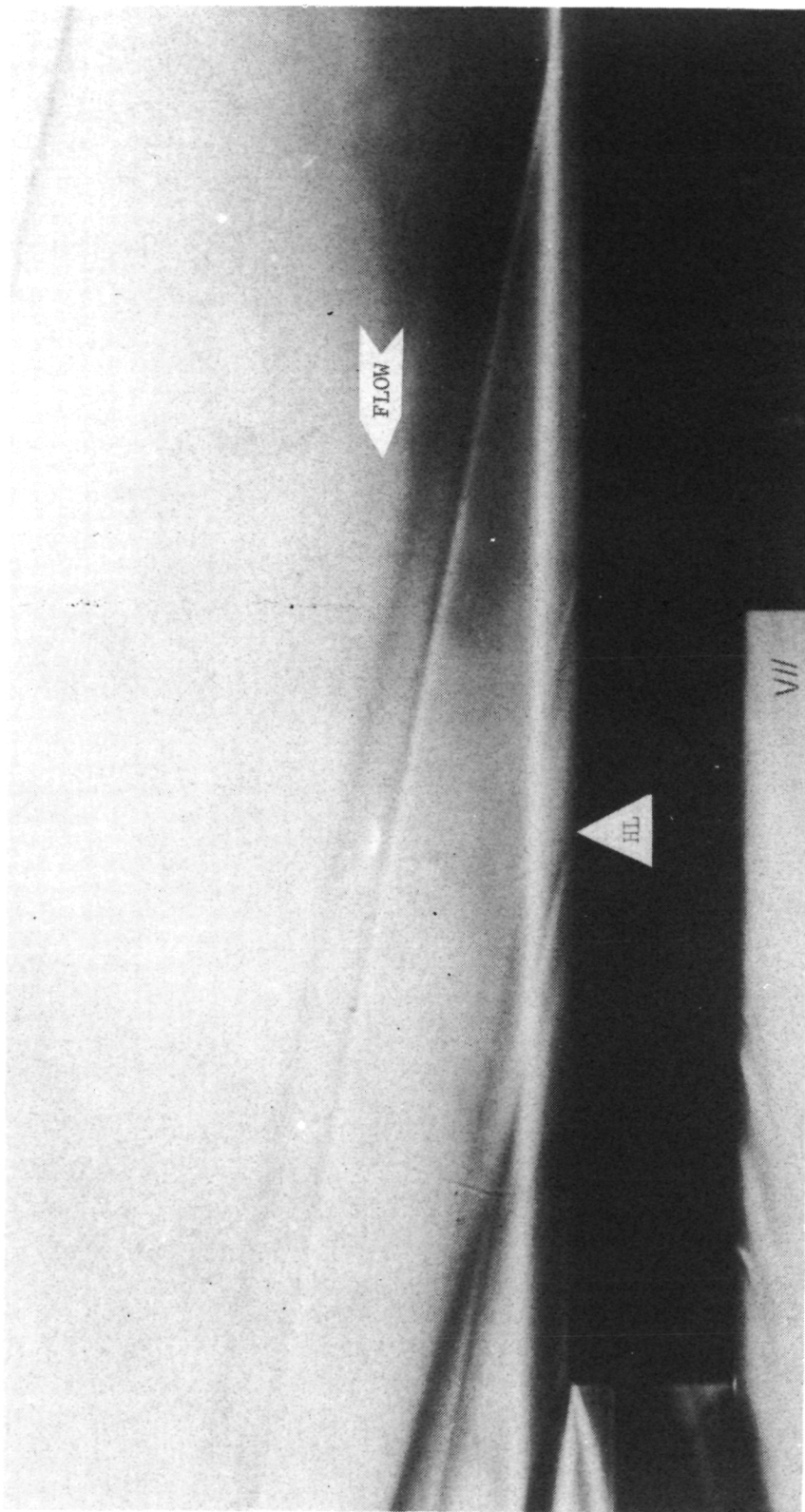


Figure 62.- Schlieren flow photograph for $\Lambda = 70^\circ$ and $\epsilon = 0^\circ$.

L-77-129

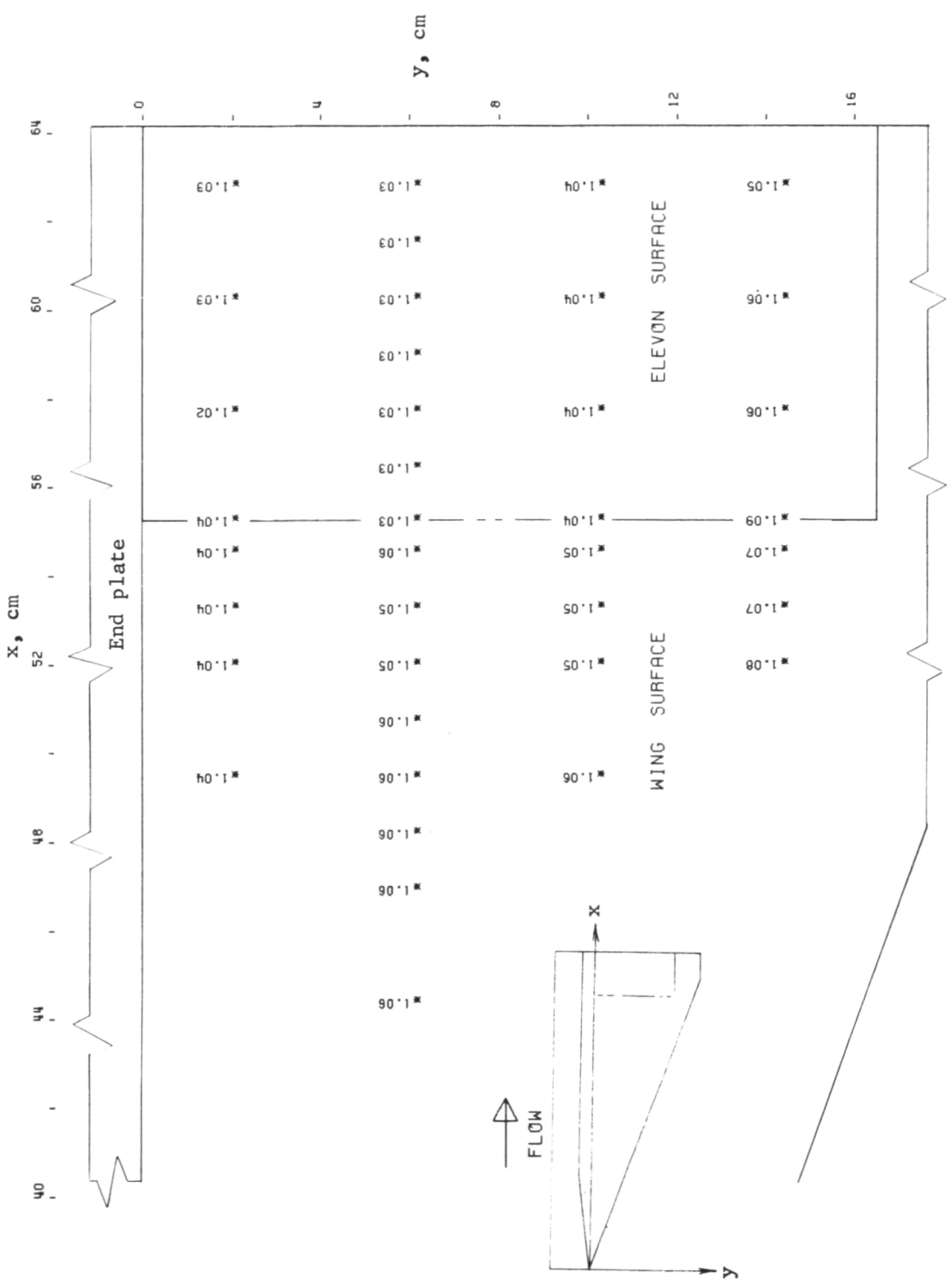


Figure 63.- Pressure-ratio (P) distribution on wing and elevon surfaces for $\Lambda = 70^\circ$, $\varepsilon = 0^\circ$, and end plate attached.

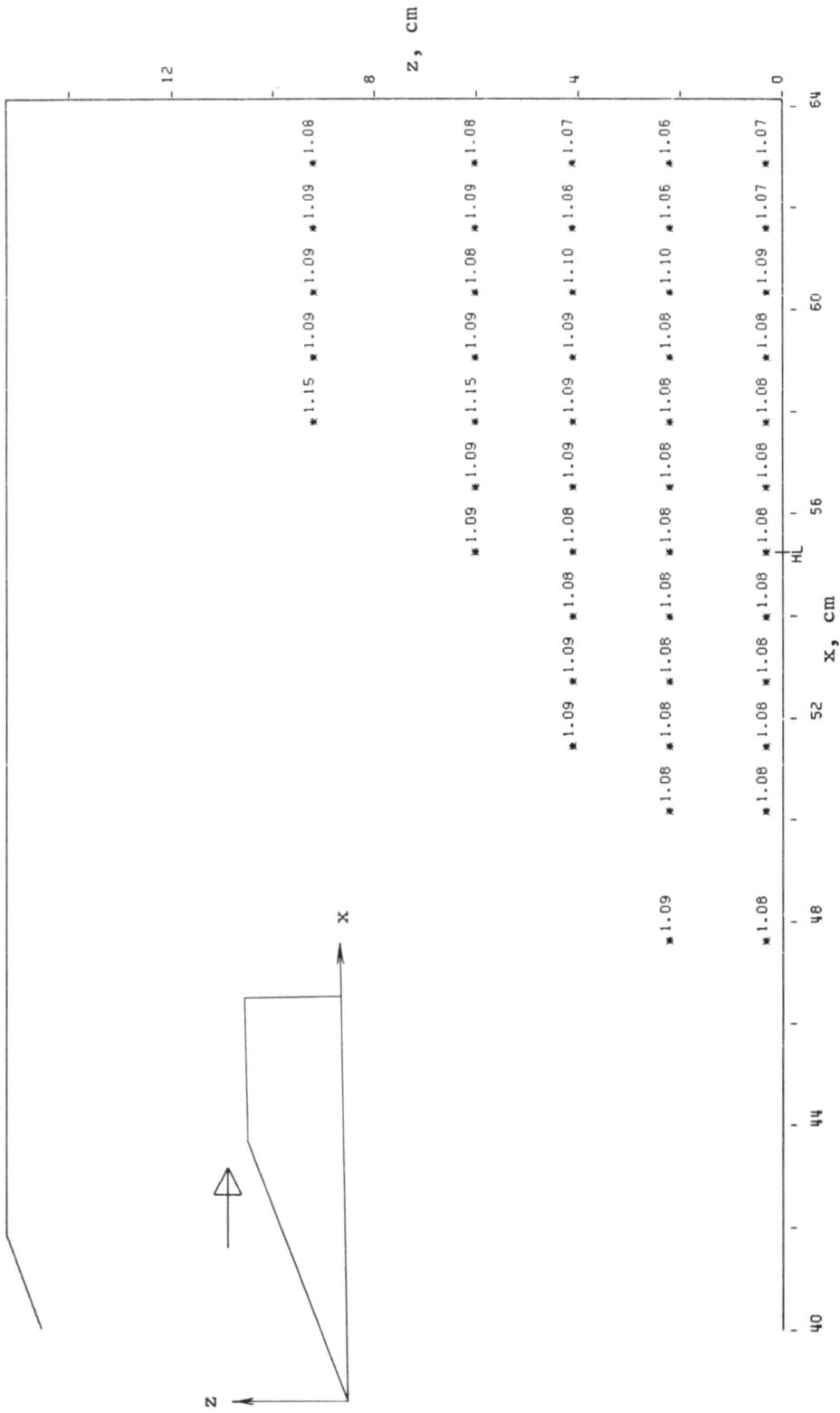


Figure 64.- Pressure-ratio (P) distribution on end-plate surface for $\Lambda = 70^\circ$ and $\epsilon = 0^\circ$.

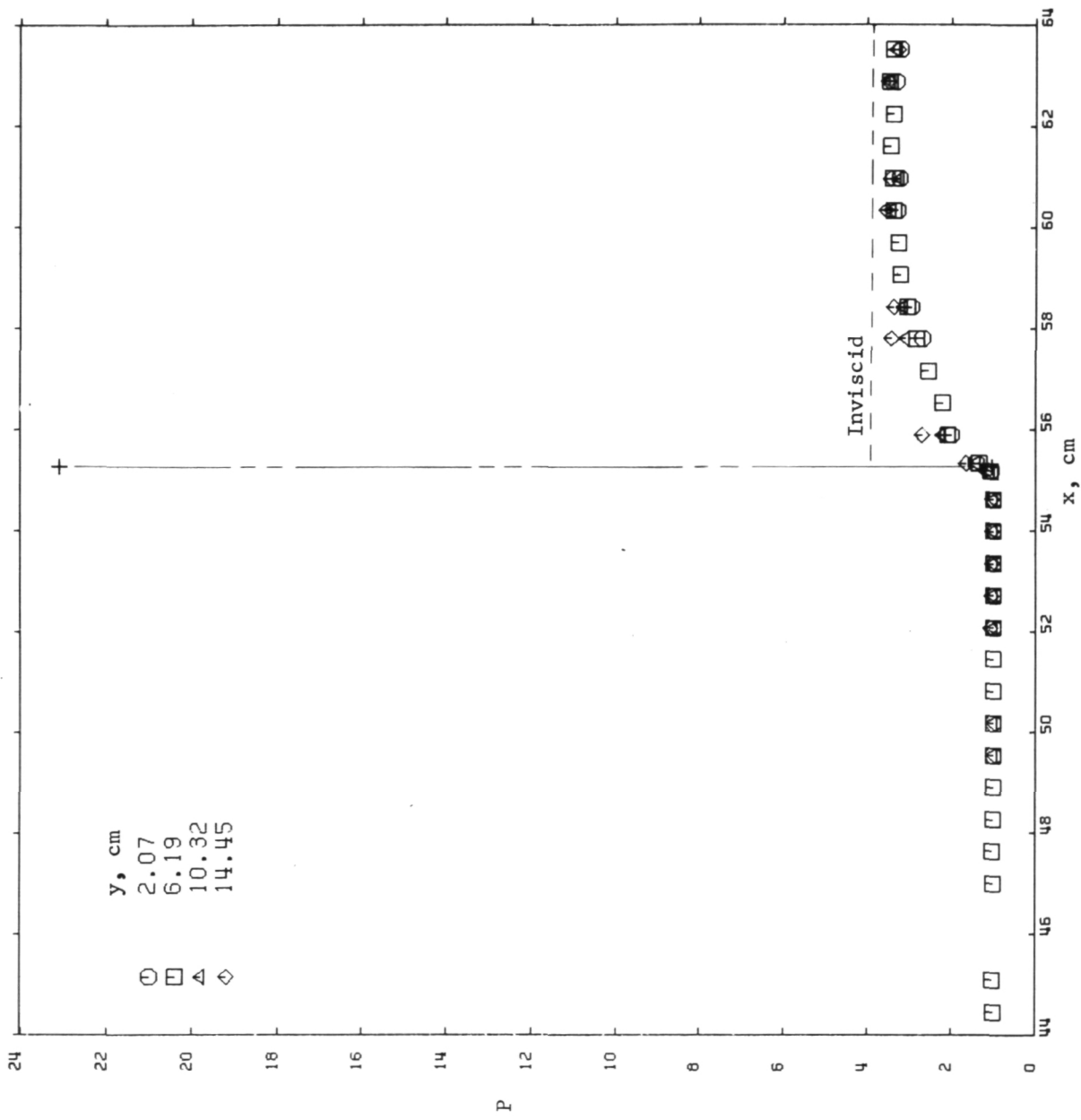


Figure 65.— Streamwise pressure-ratio distributions on wing and elevon surfaces for $\Lambda = 70^\circ$ and $\epsilon = 10^\circ$.

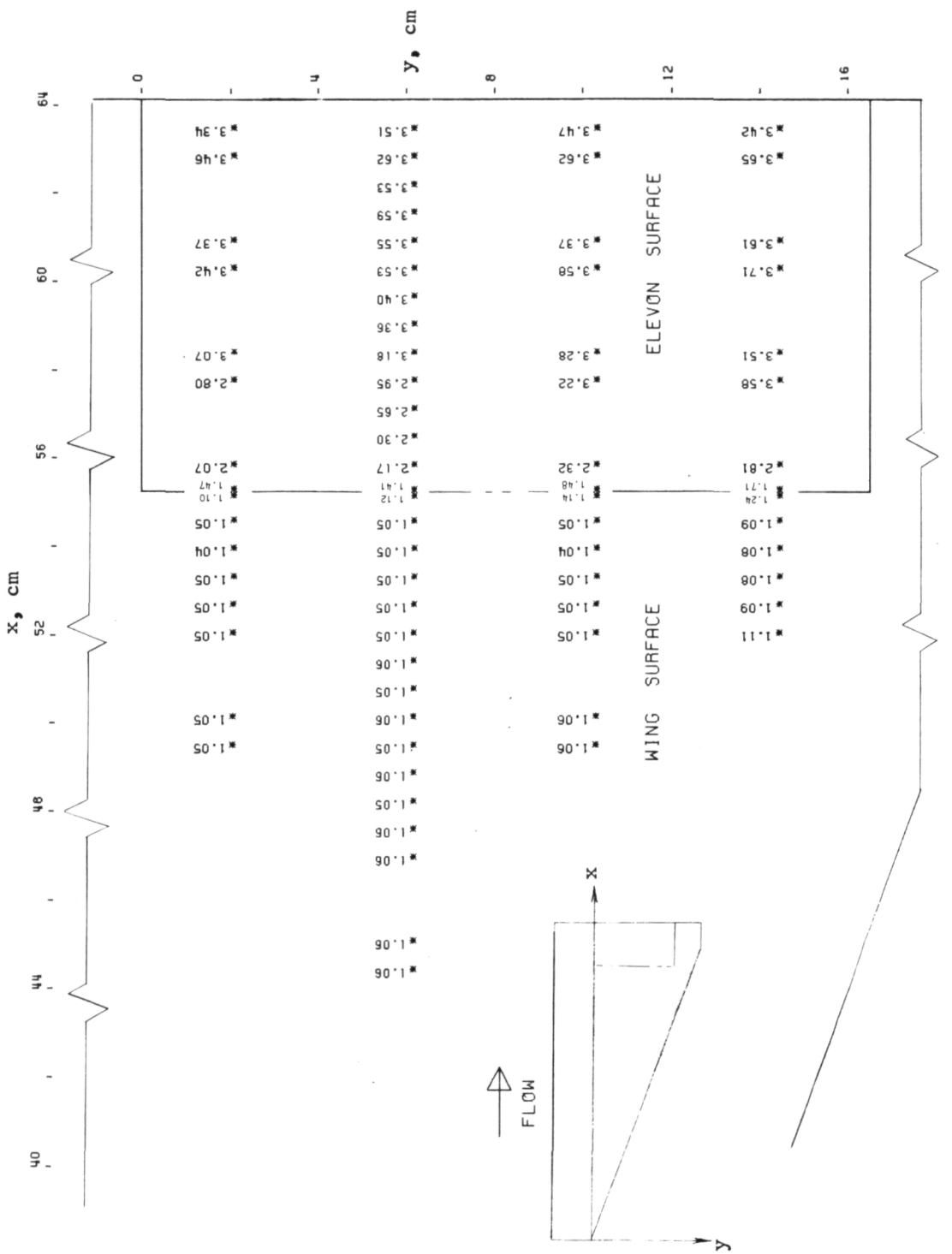
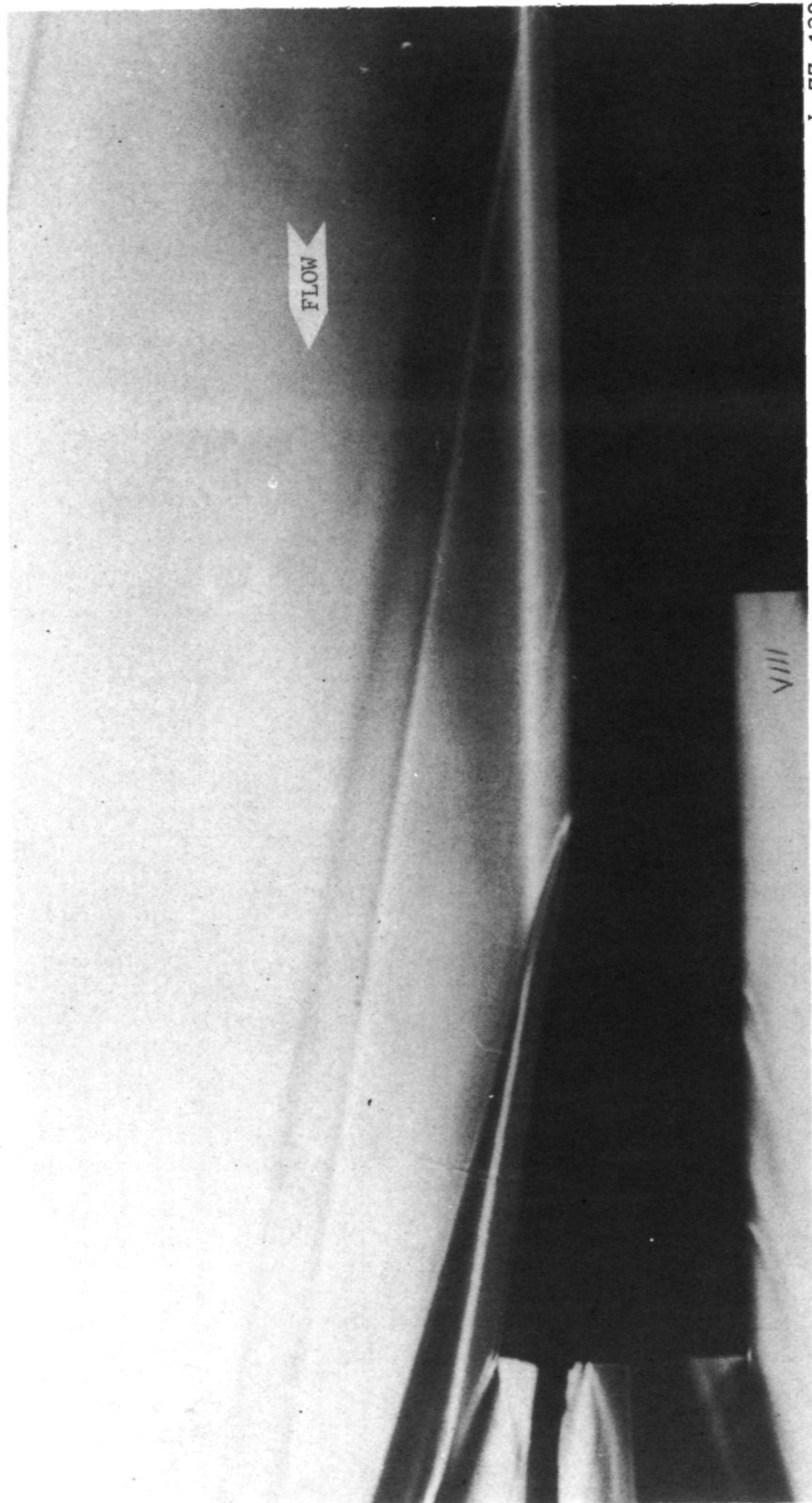


Figure 66.— Pressure-ratio (P) distribution on wing and elevon surfaces
for $\Lambda = 70^\circ$ and $\epsilon = 10^\circ$.

L-77-130

Figure 67.- Schlieren flow photograph for $\Lambda = 70^\circ$ and $\epsilon = 10^\circ$.



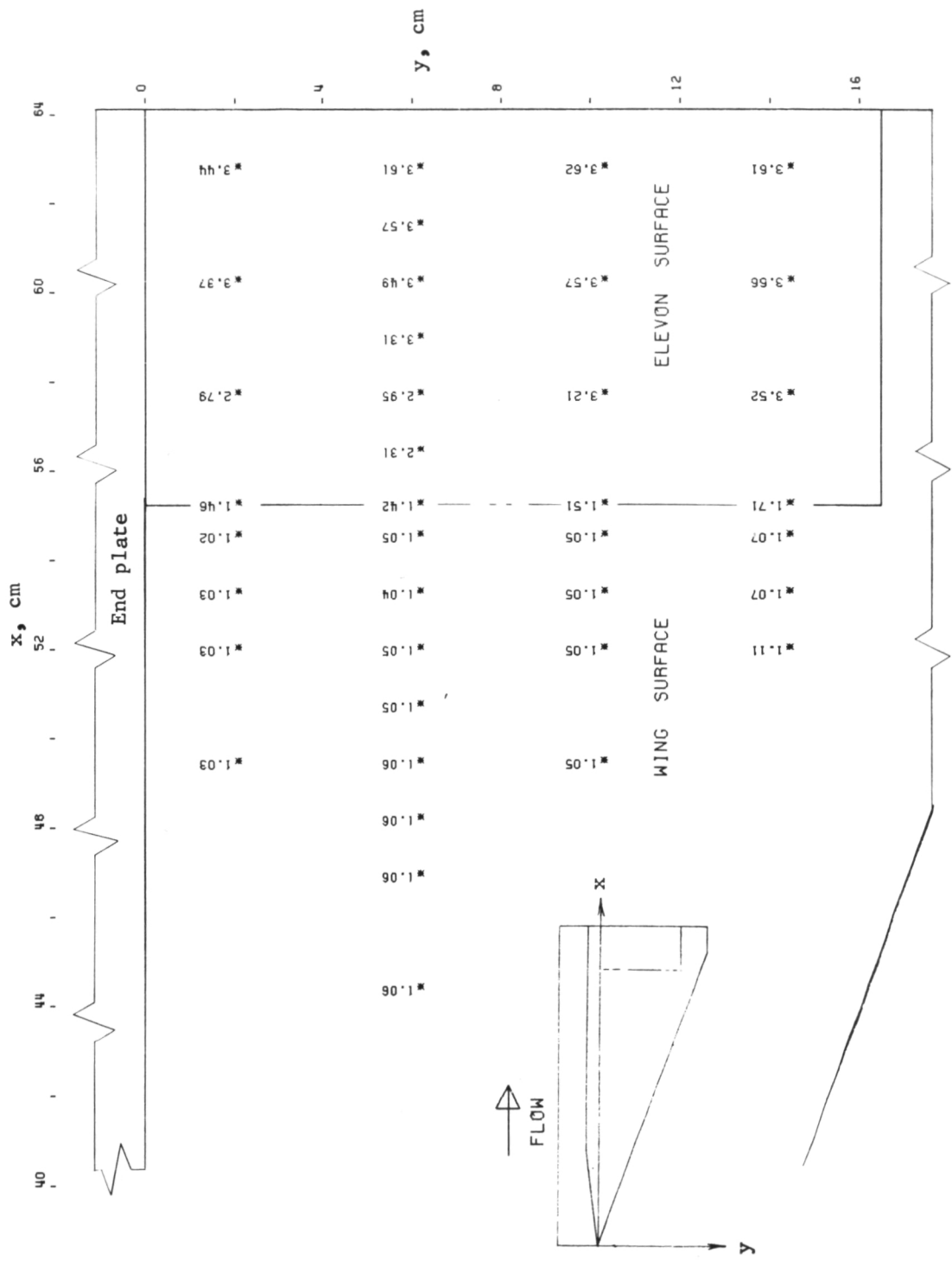


Figure 68.- Pressure-ratio (P) distribution on wing and elevon surfaces for $\Lambda = 70^\circ$, $\epsilon = 10^\circ$, and end plate attached.

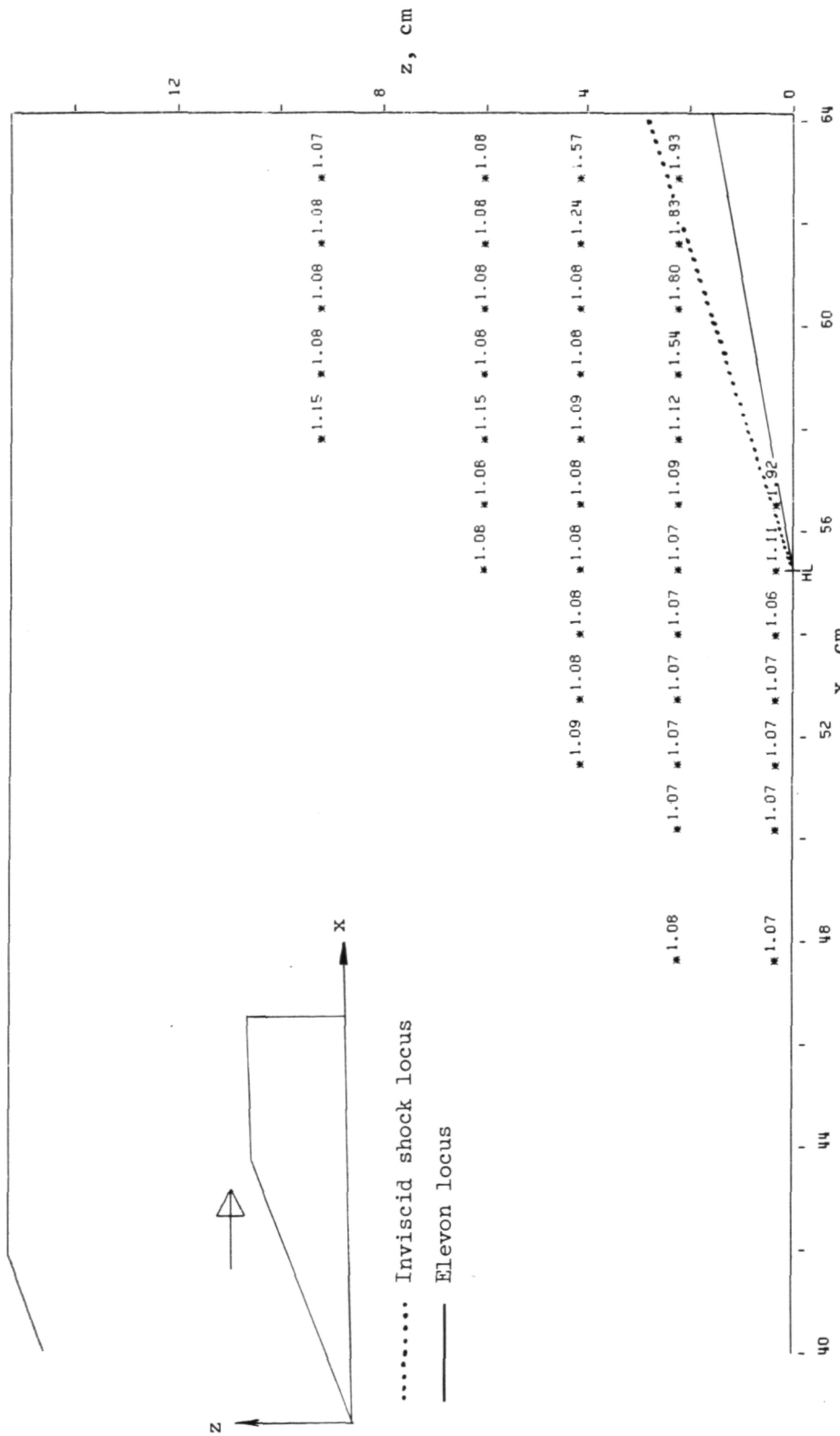
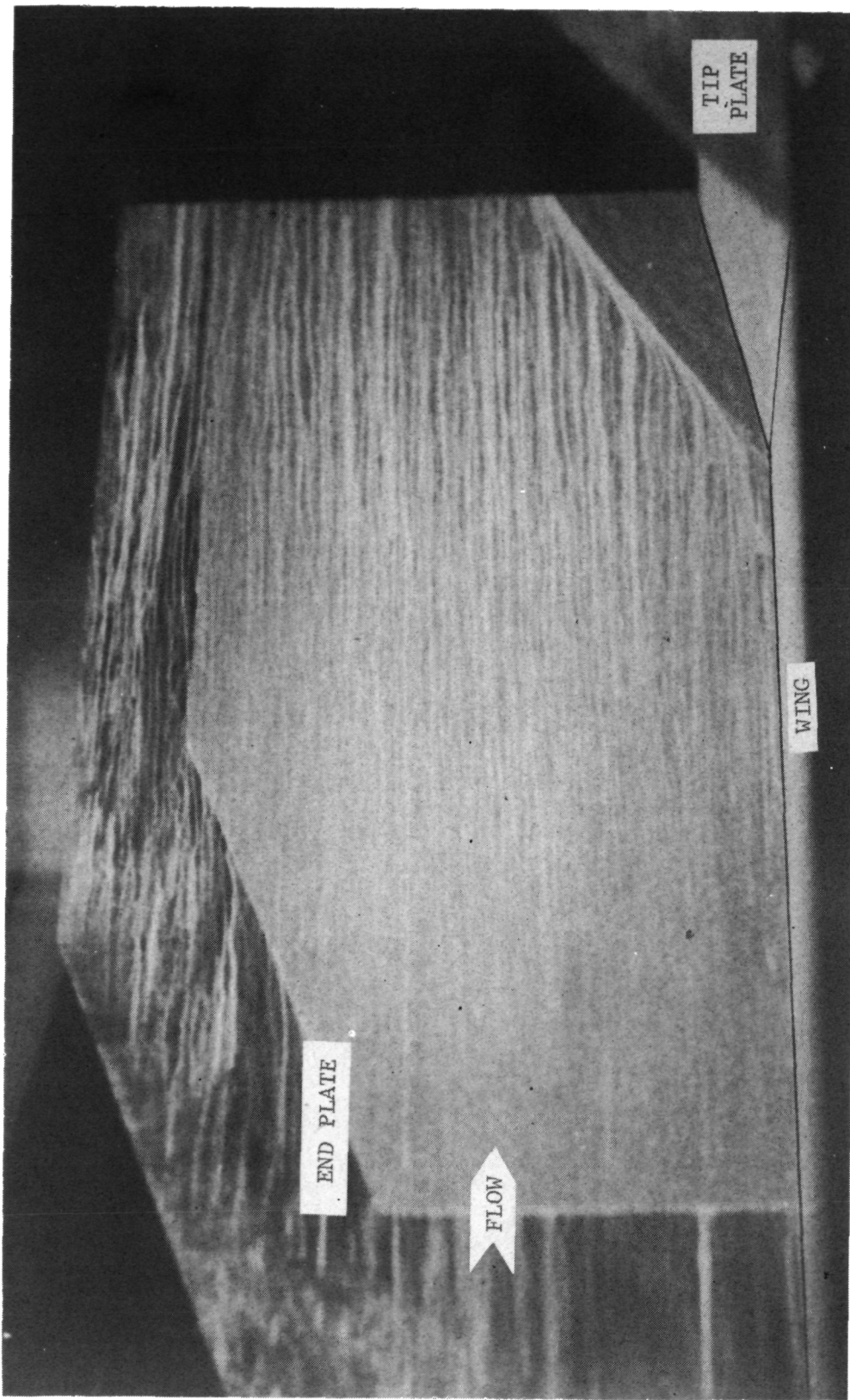


Figure 69.- Pressure-ratio (P) distribution on end-plate surface for $\Lambda = 70^\circ$ and $\epsilon = 100$.



L-77-131

Figure 70.- Frame from surface-oil-flow motion picture for $\Lambda = 70^\circ$,
 $\epsilon = 10^\circ$, end plate attached, and tip plate attached.

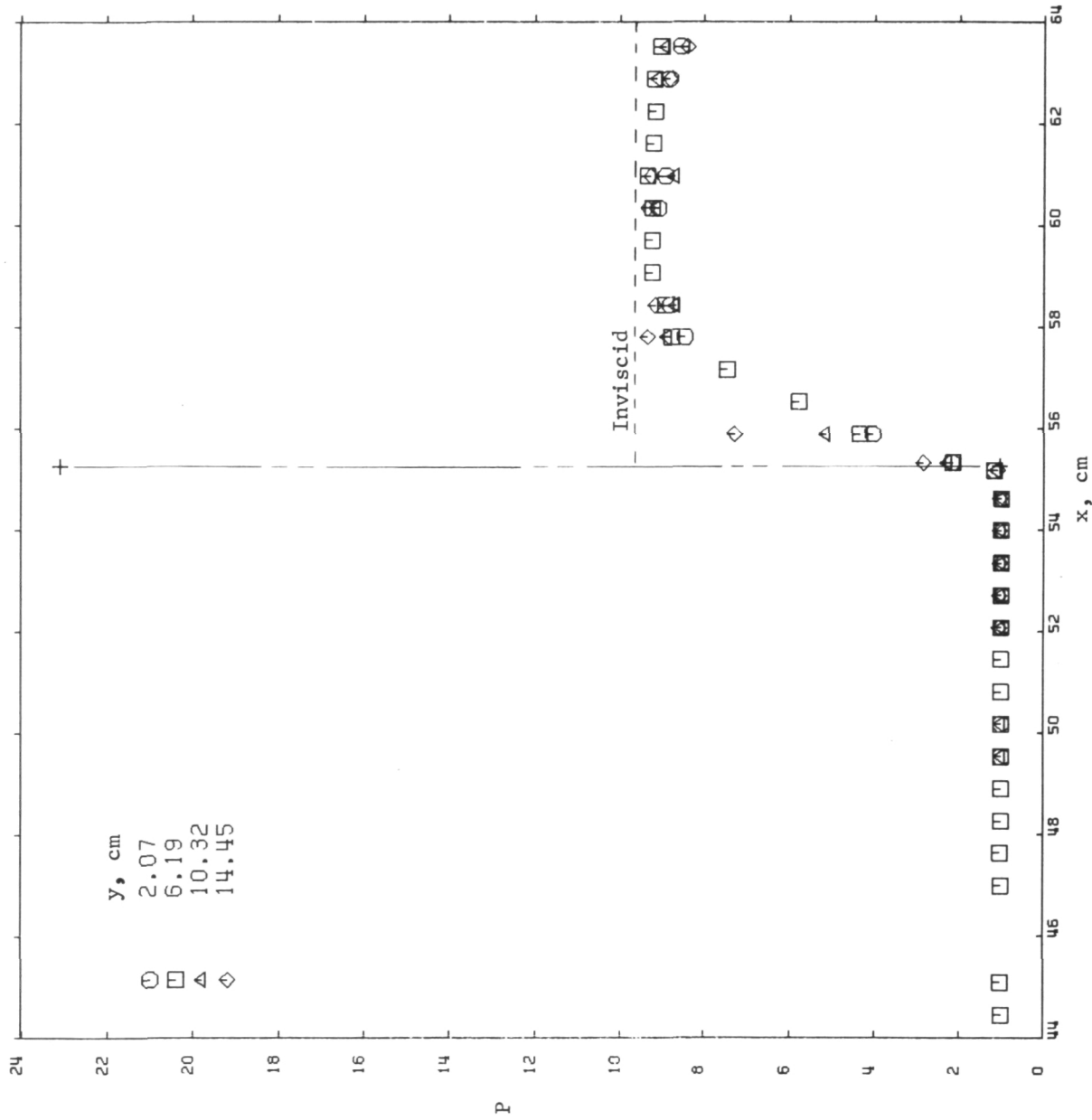


Figure 71.— Streamwise pressure-ratio distributions on wing and elevon surfaces for $\Lambda = 70^\circ$ and $\epsilon = 20^\circ$.

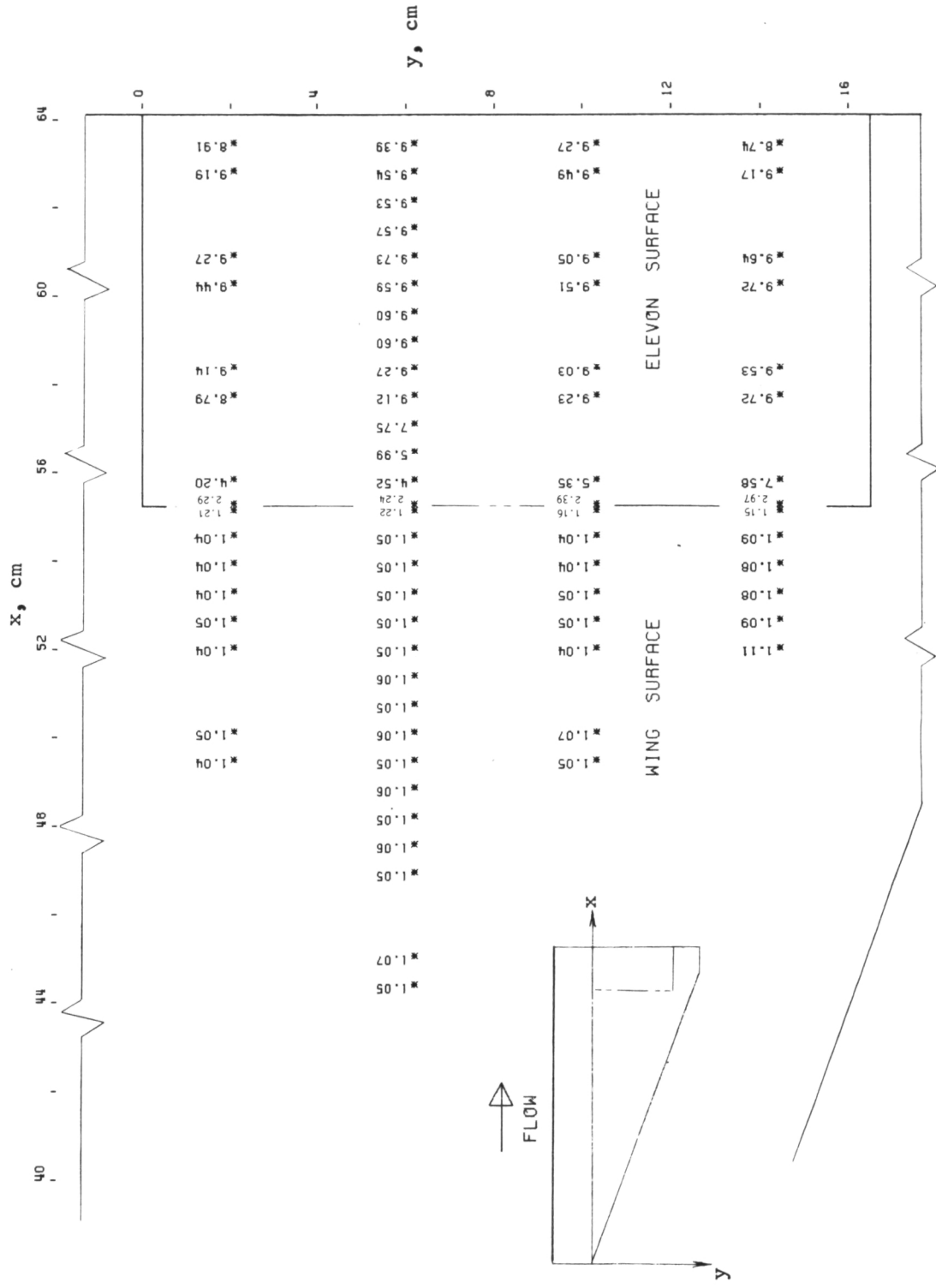


Figure 72.— Pressure-ratio (P) distribution on wing and elevon surfaces for $\Lambda = 70^\circ$ and $\epsilon = 20^\circ$.

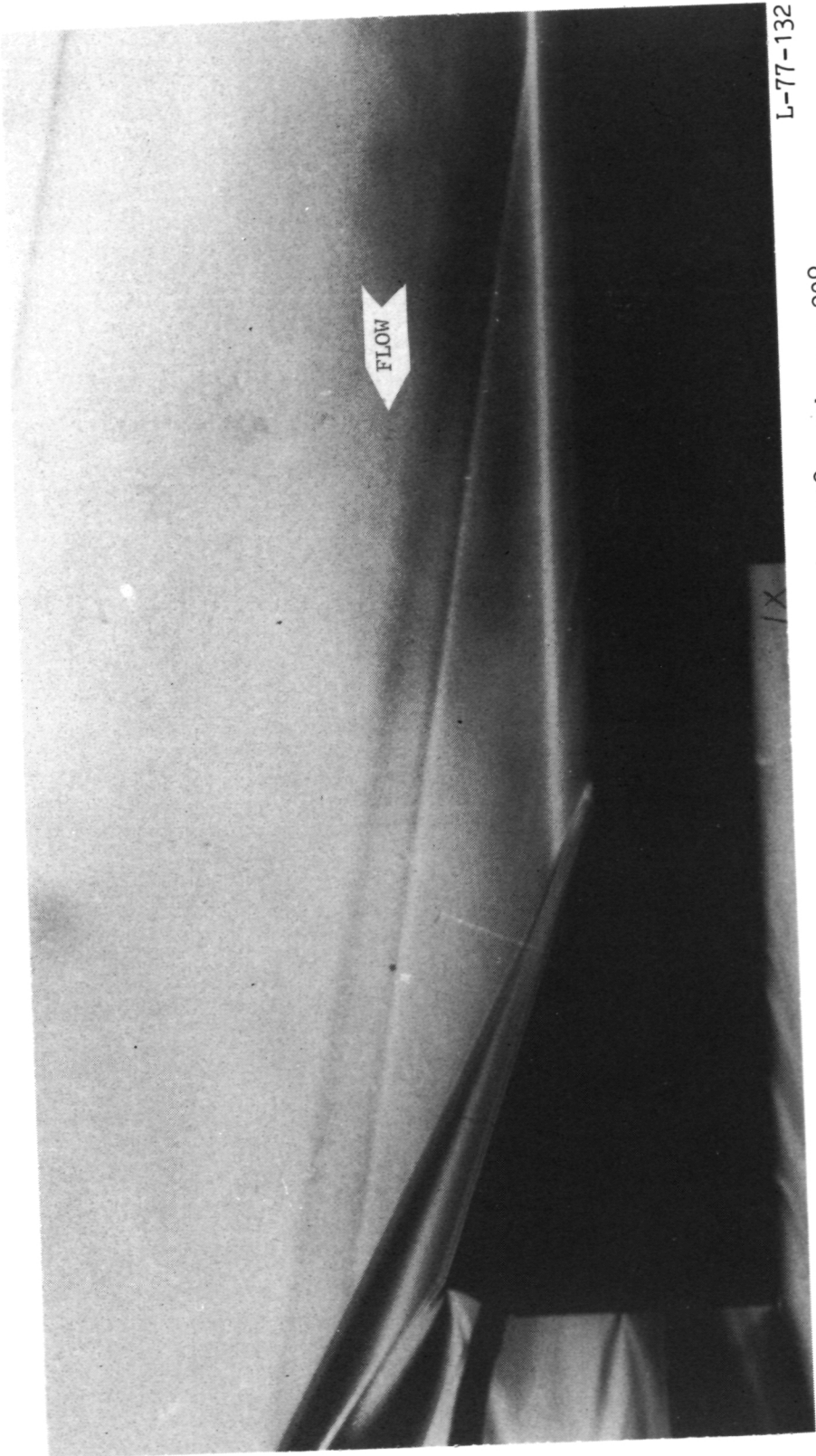


Figure 73.- Schlieren flow photograph for $\Lambda = 70^\circ$ and $\epsilon = 20^\circ$.

L-77-132

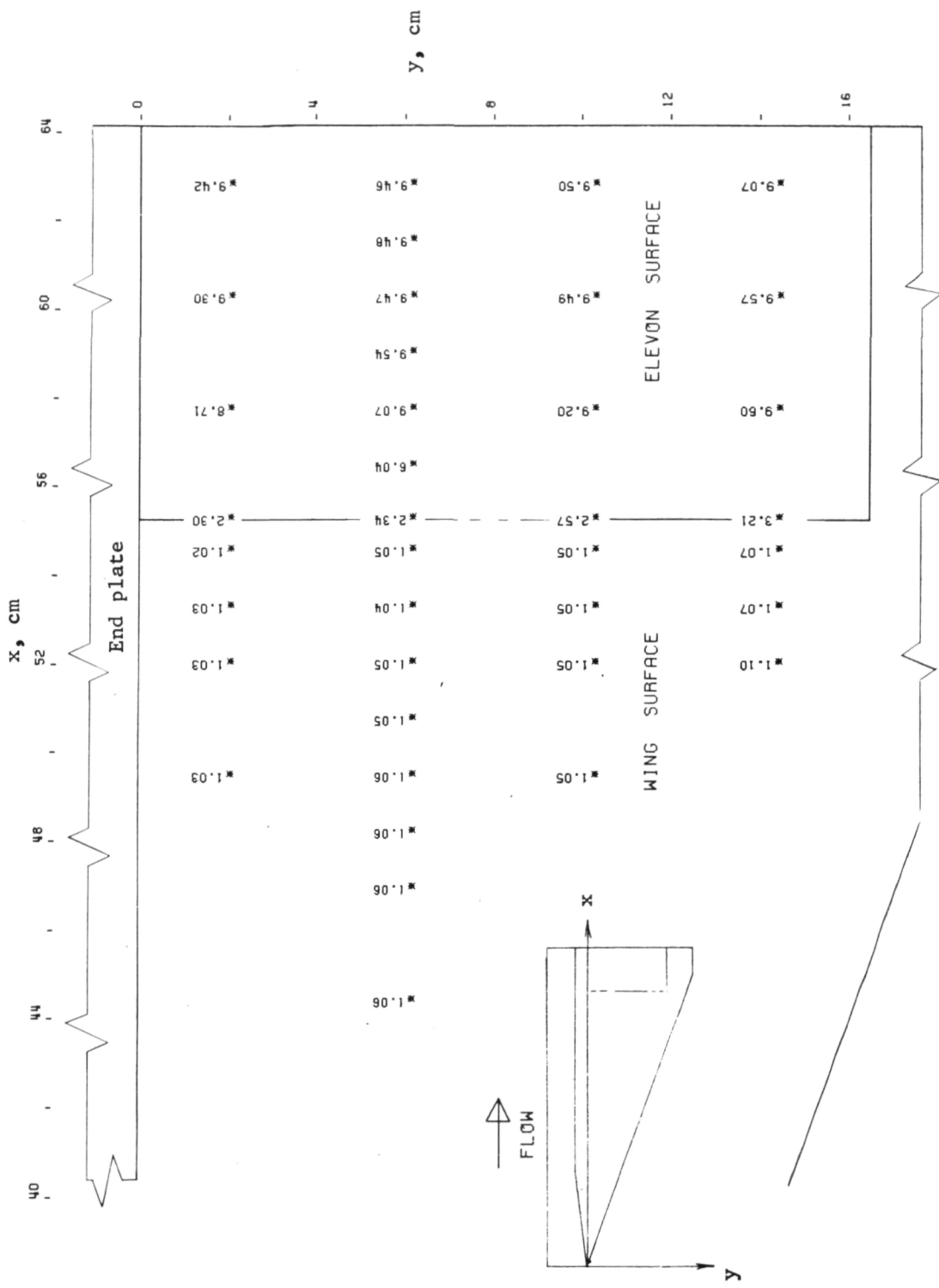


Figure 74.— Pressure-ratio (P) distribution on wing and elevon surfaces for $\Lambda = 70^\circ$, $\epsilon = 20^\circ$, and end plate attached.

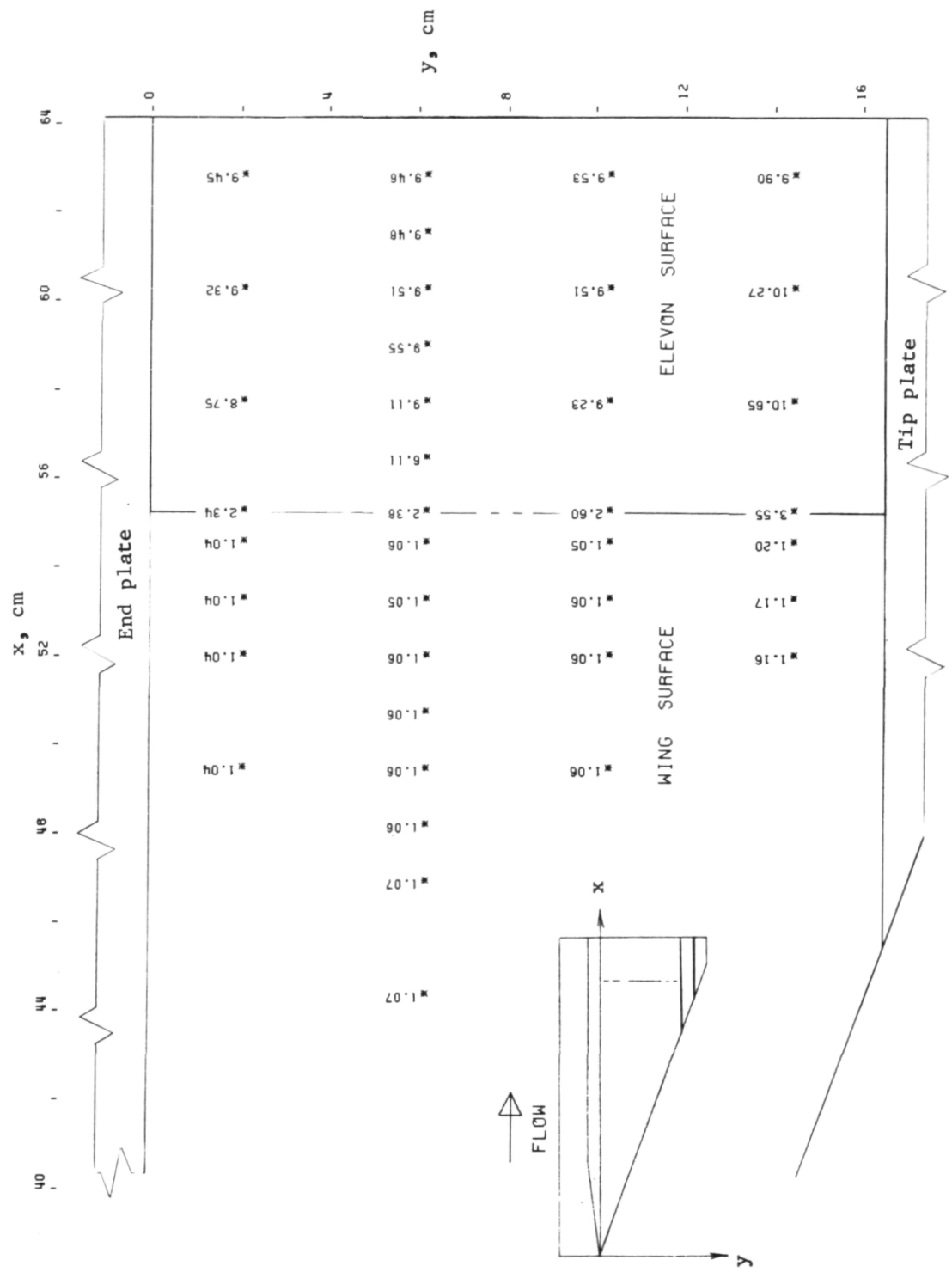


Figure 75.- Pressure-ratio (P) distribution on wing and elevon surfaces for $\Lambda = 70^\circ$, $\epsilon = 20^\circ$, end plate attached, and tip plate attached.

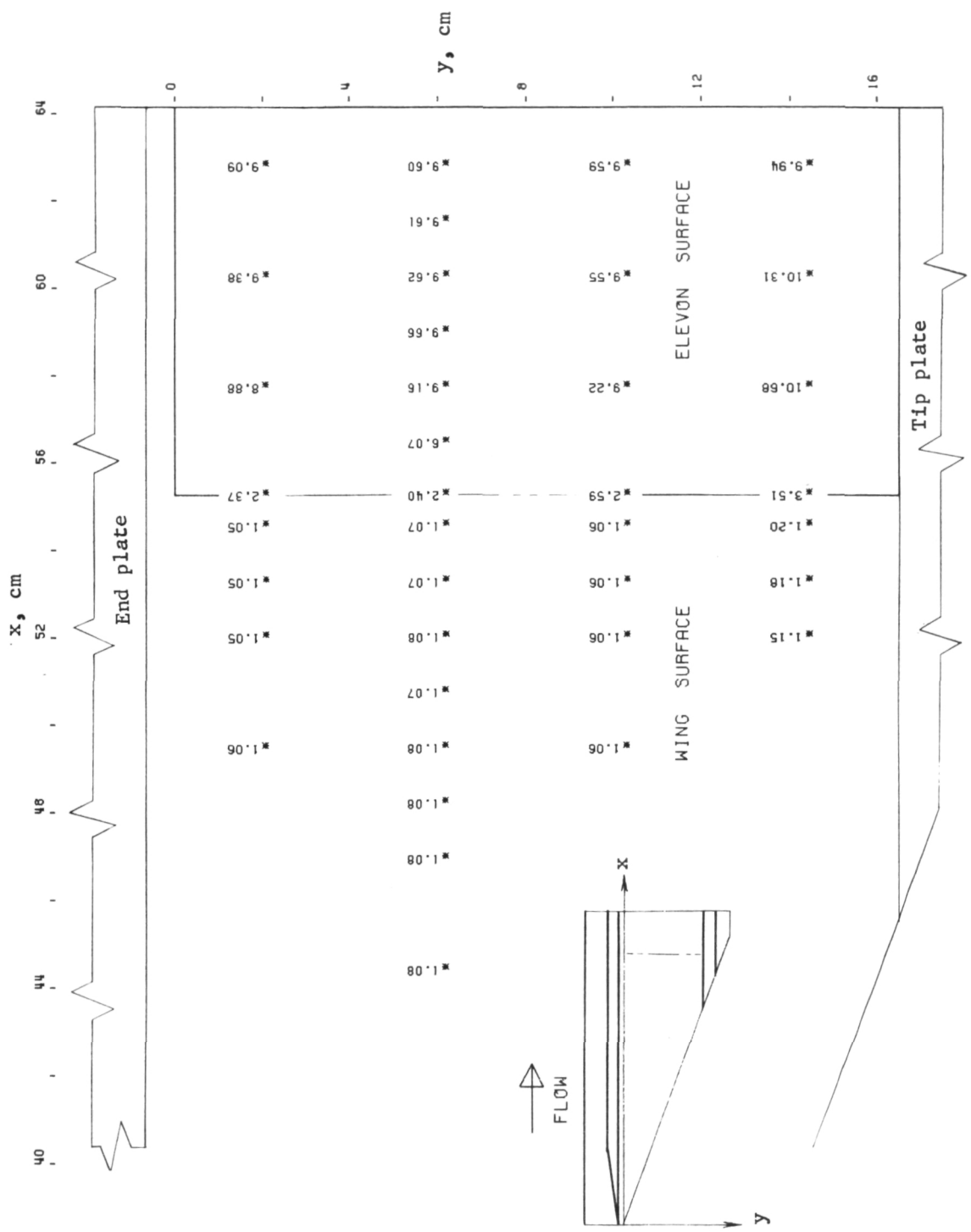


Figure 76.- Pressure-ratio (P) distribution on wing and elevon surfaces for $\Lambda = 70^\circ$, $\epsilon = 20^\circ$, end plate attached 0.64 cm away from inboard edge of elevon, and tip plate attached.

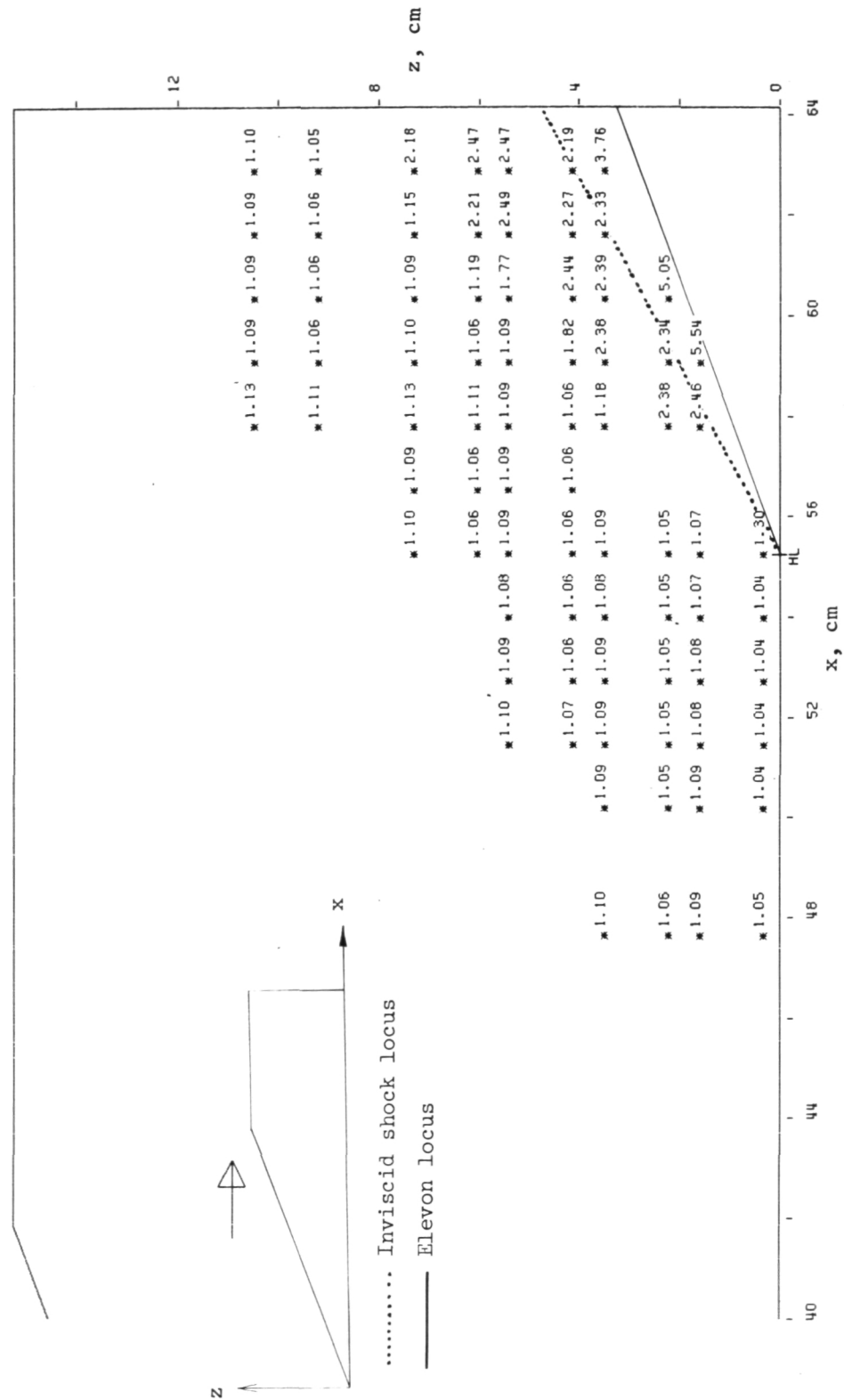


Figure 77.- Pressure-ratio (P) distribution on end-plate surface for $\Lambda = 70^\circ$ and $\epsilon = 20^\circ$.

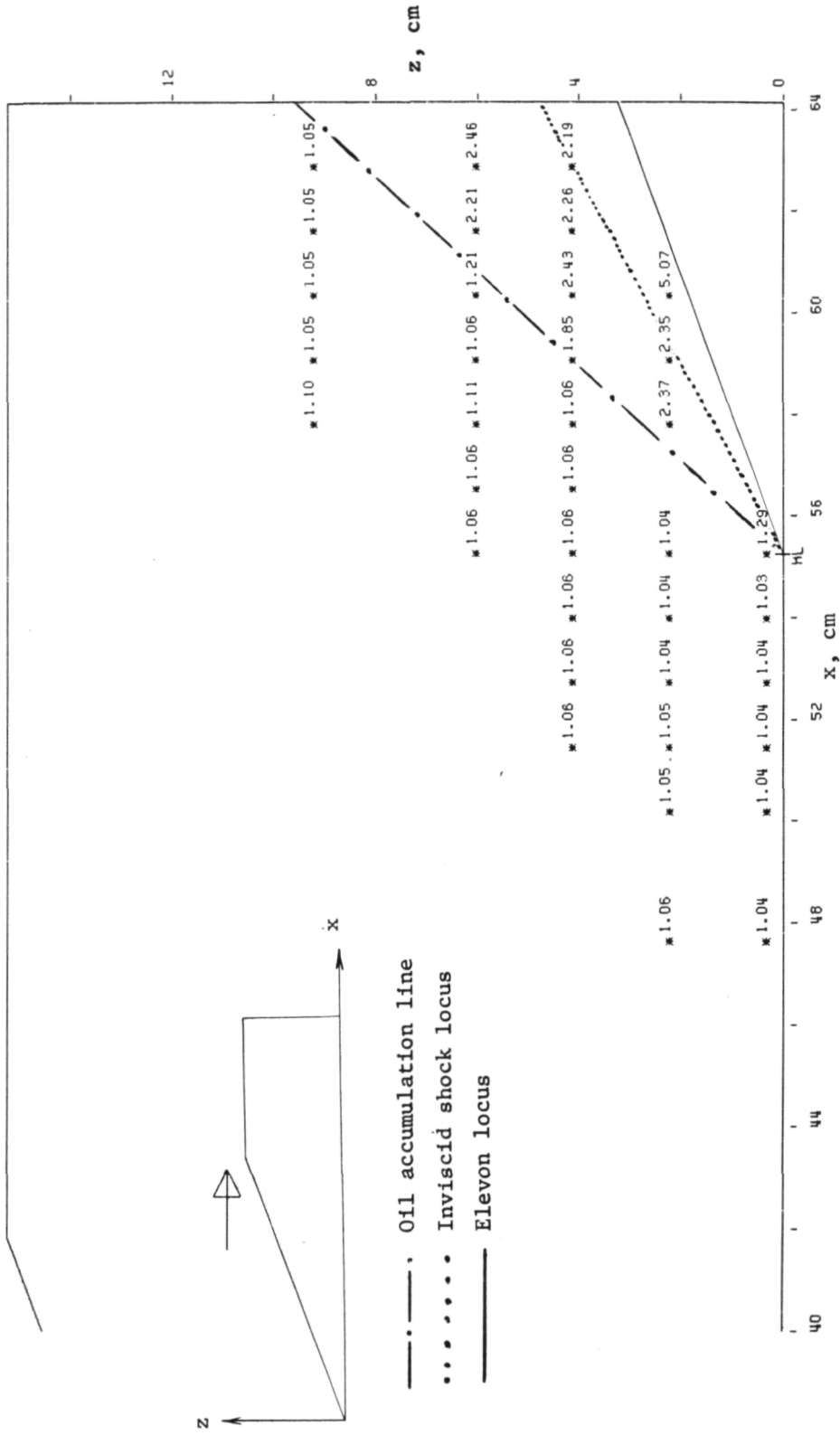


Figure 78.- Pressure-ratio (P) distribution on end-plate surface for $\Lambda = 70^\circ$, $\epsilon = 20^\circ$, and tip plate attached.

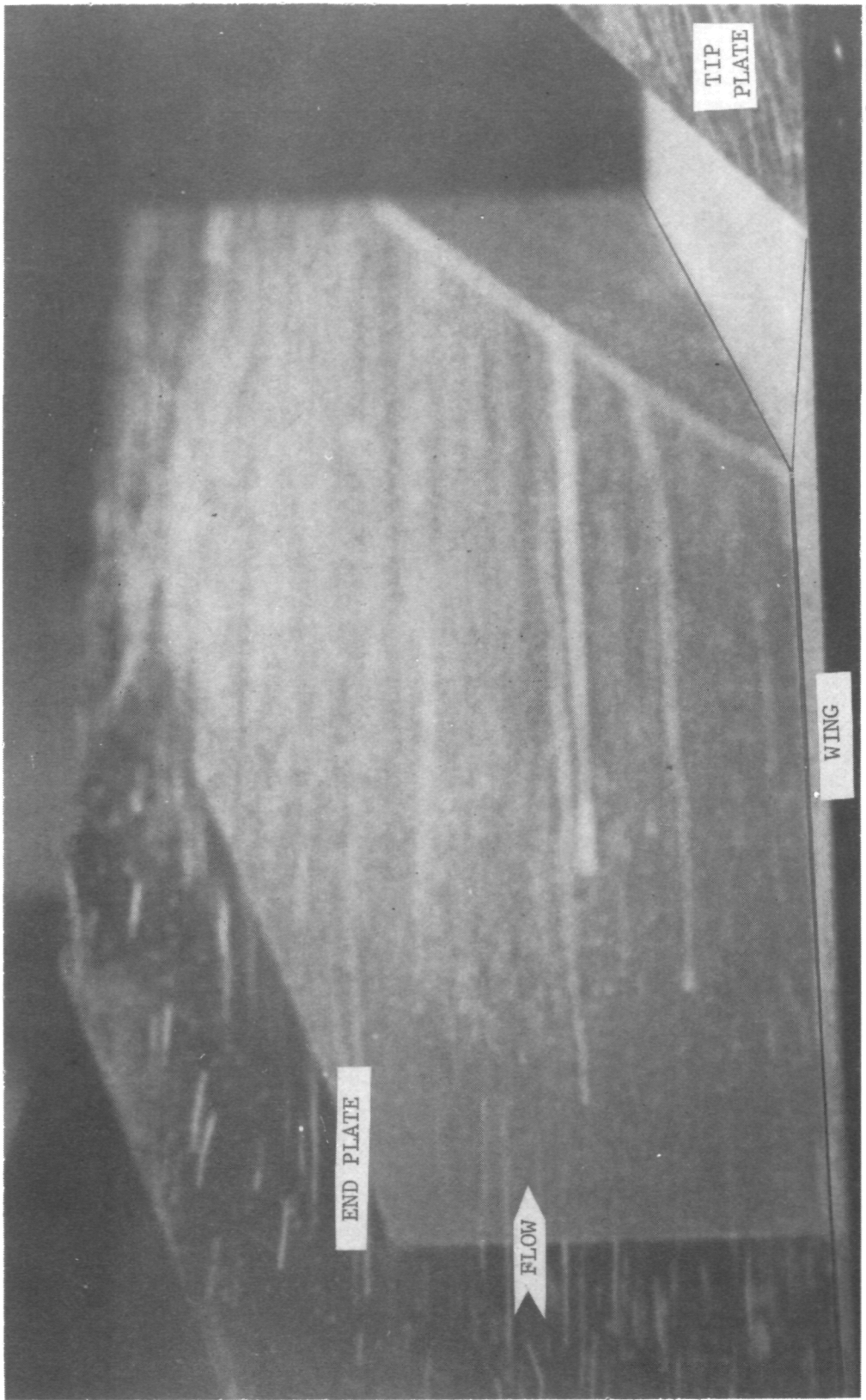


Figure 79.- Frame from surface-oil-flow motion picture for $\Lambda = 70^\circ$, $\epsilon = 20^\circ$, end plate attached, and tip plate attached. L-77-133

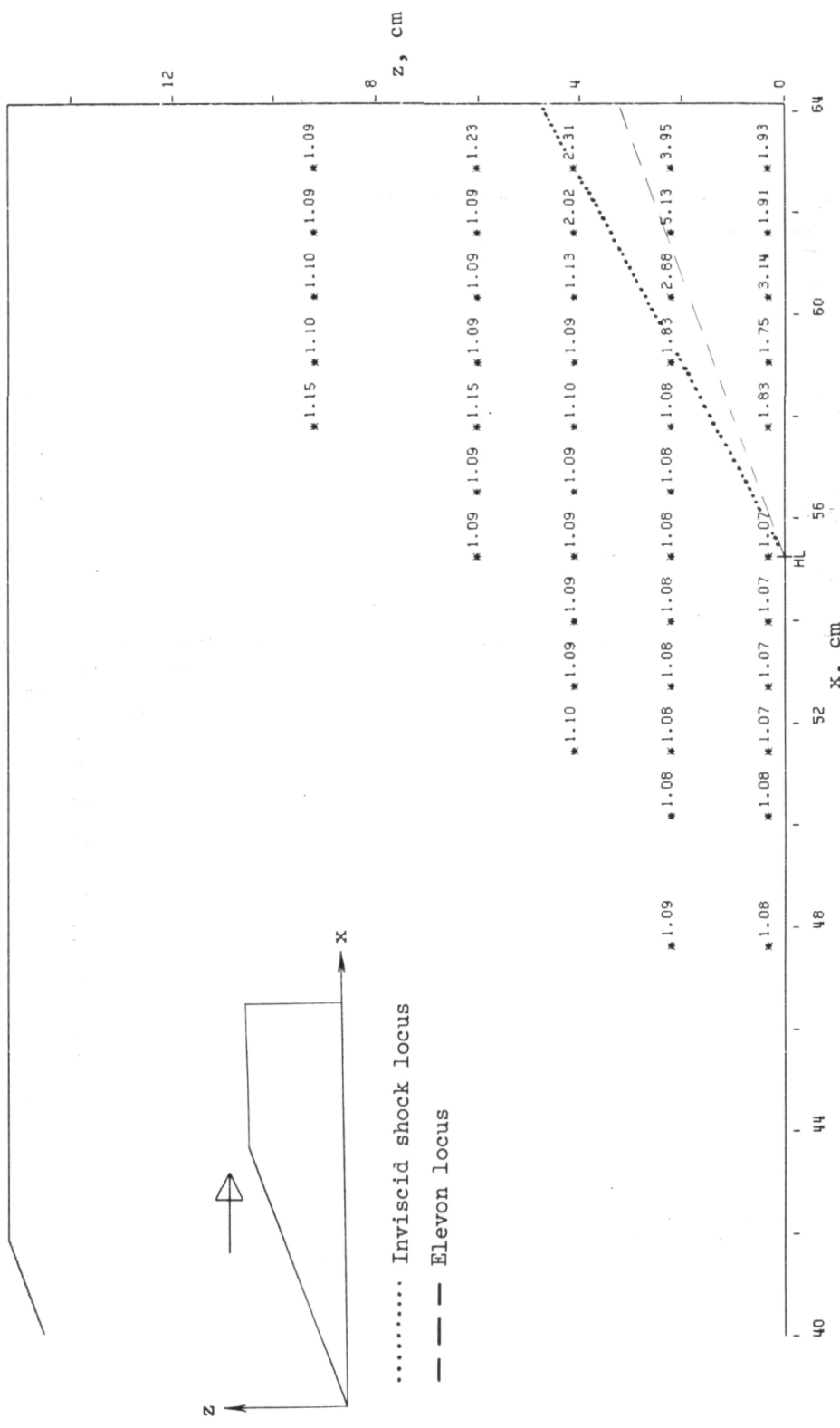


Figure 80.- Pressure-ratio (P) distribution on end-plate surface for $\Lambda = 70^\circ$, $\epsilon = 20^\circ$, 0.64-cm gap between end plate and elevon, and tip plate attached.

24

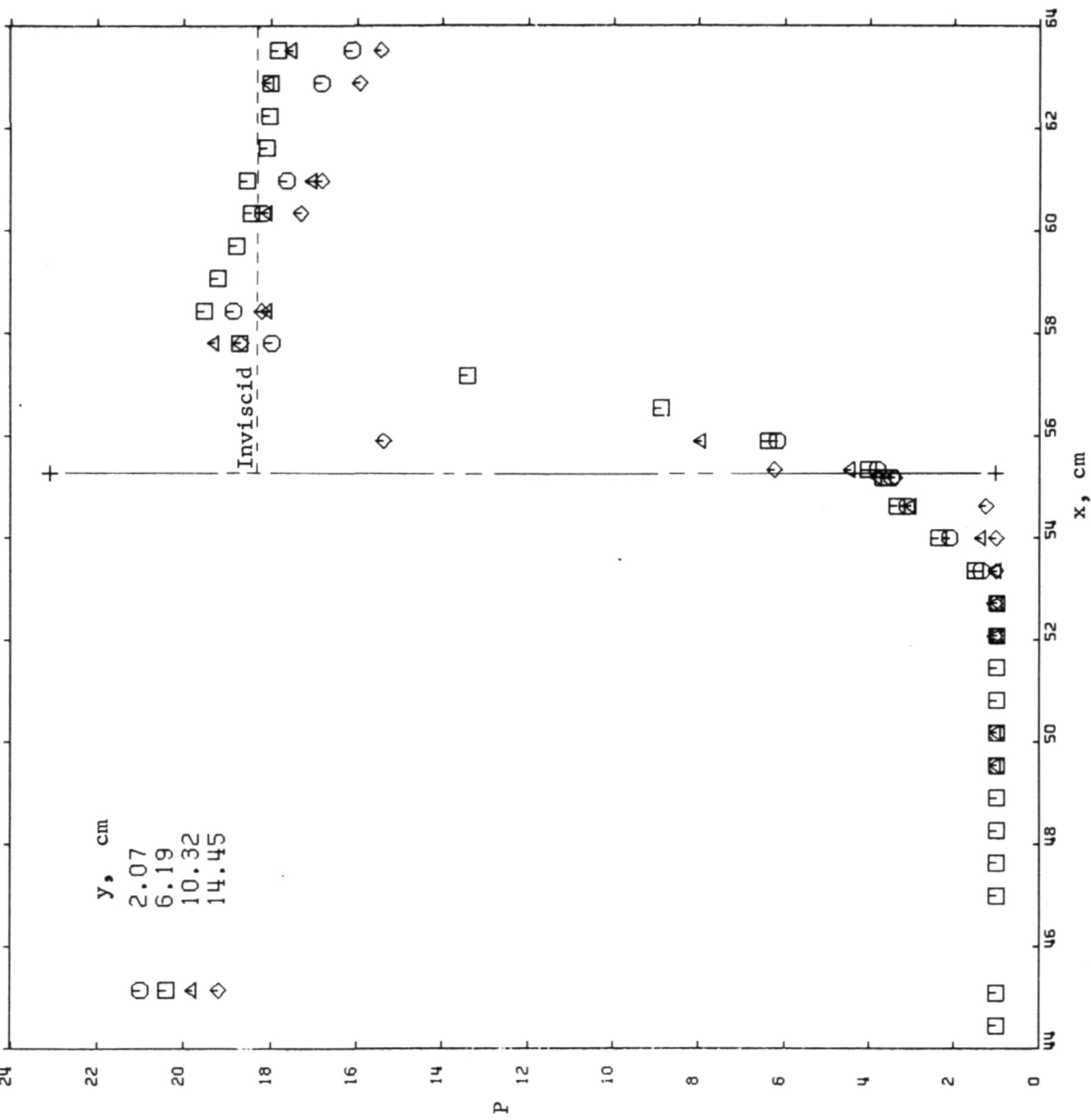


Figure 81.— Streamwise pressure-ratio distributions on wing and elevon surfaces for $\Lambda = 70^\circ$ and $\epsilon = 30^\circ$.

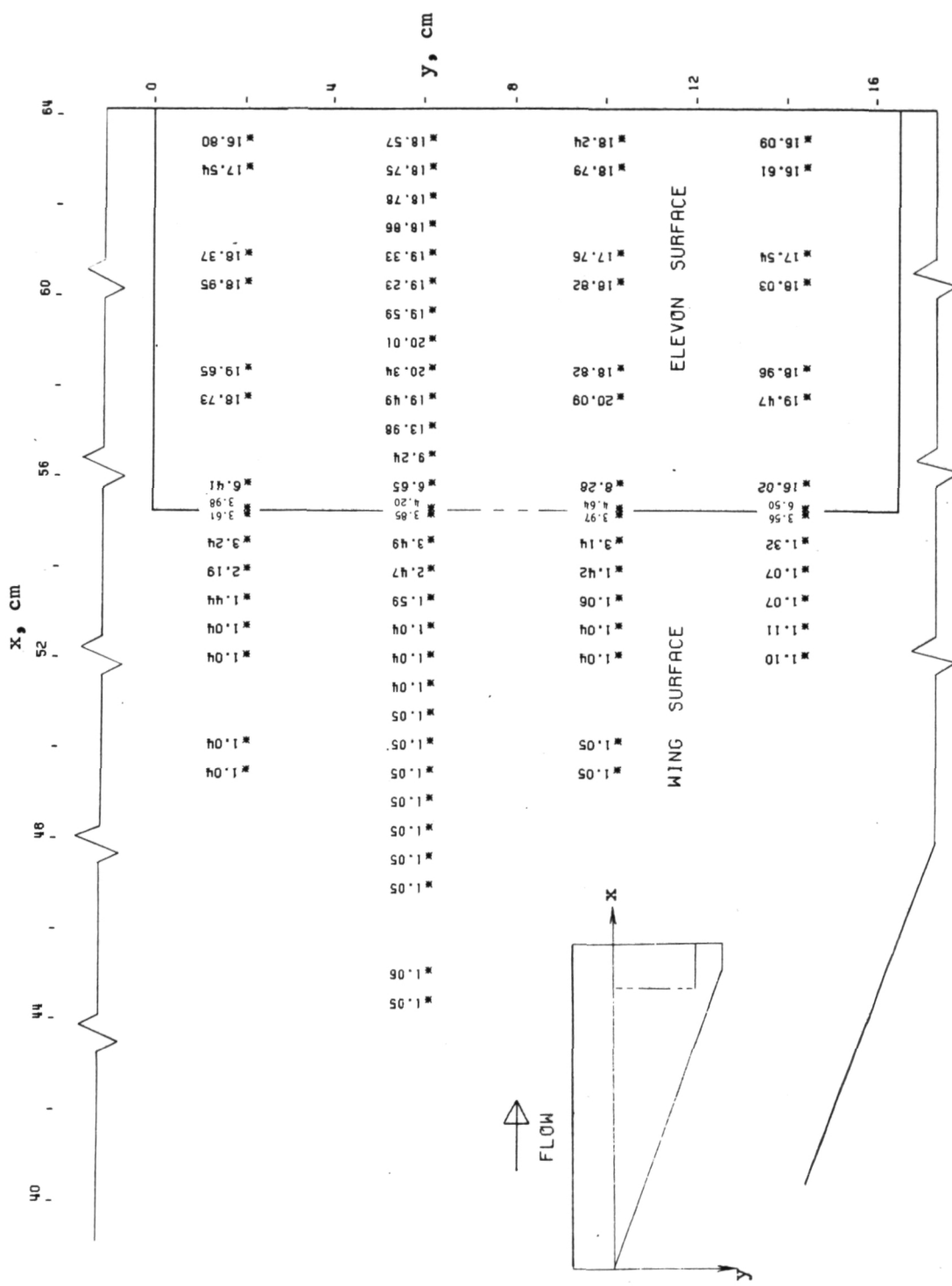
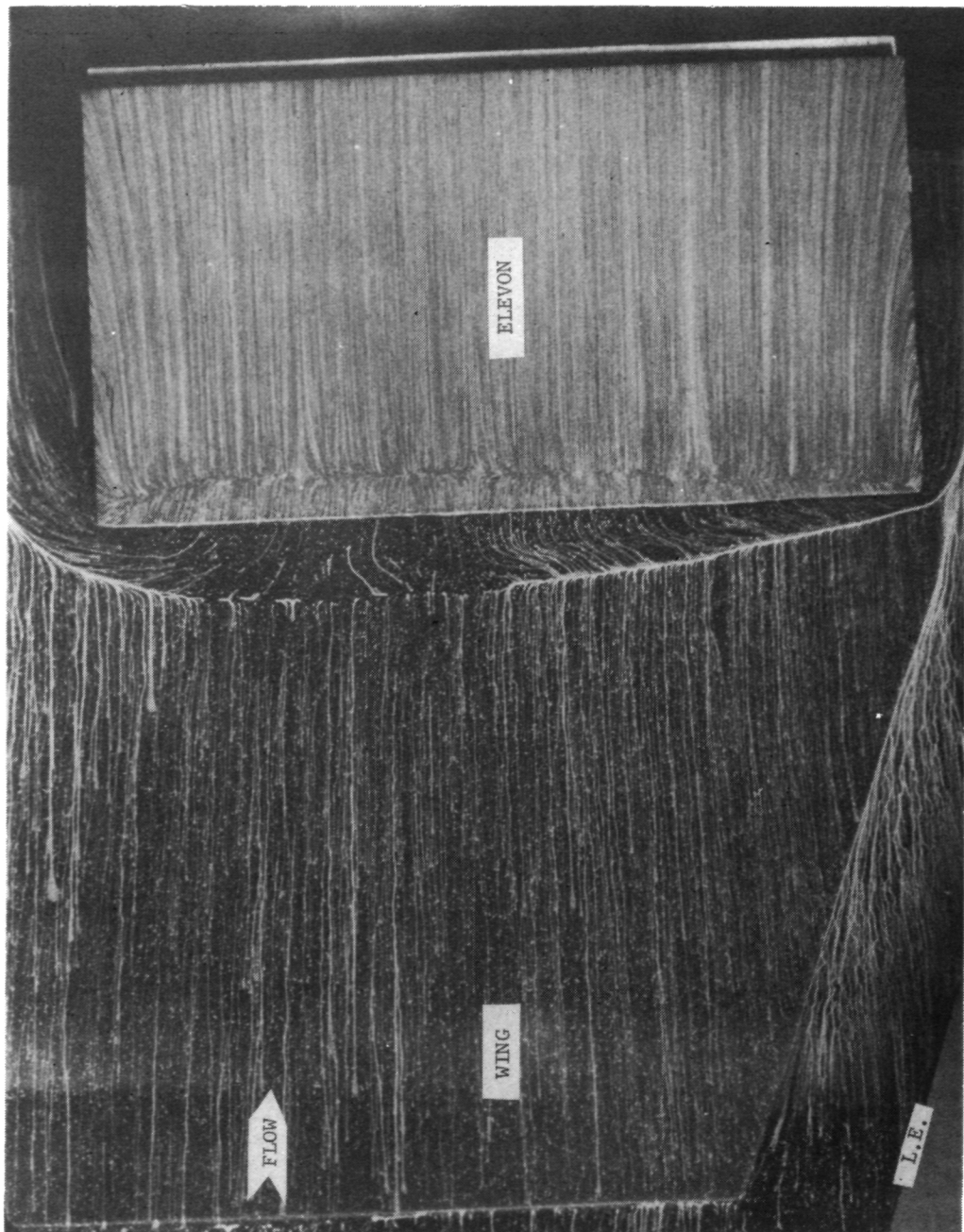


Figure 82.— Pressure-ratio distribution (P) distribution on wing and elevon surfaces for $\Lambda = 70^\circ$ and $\epsilon = 30^\circ$.

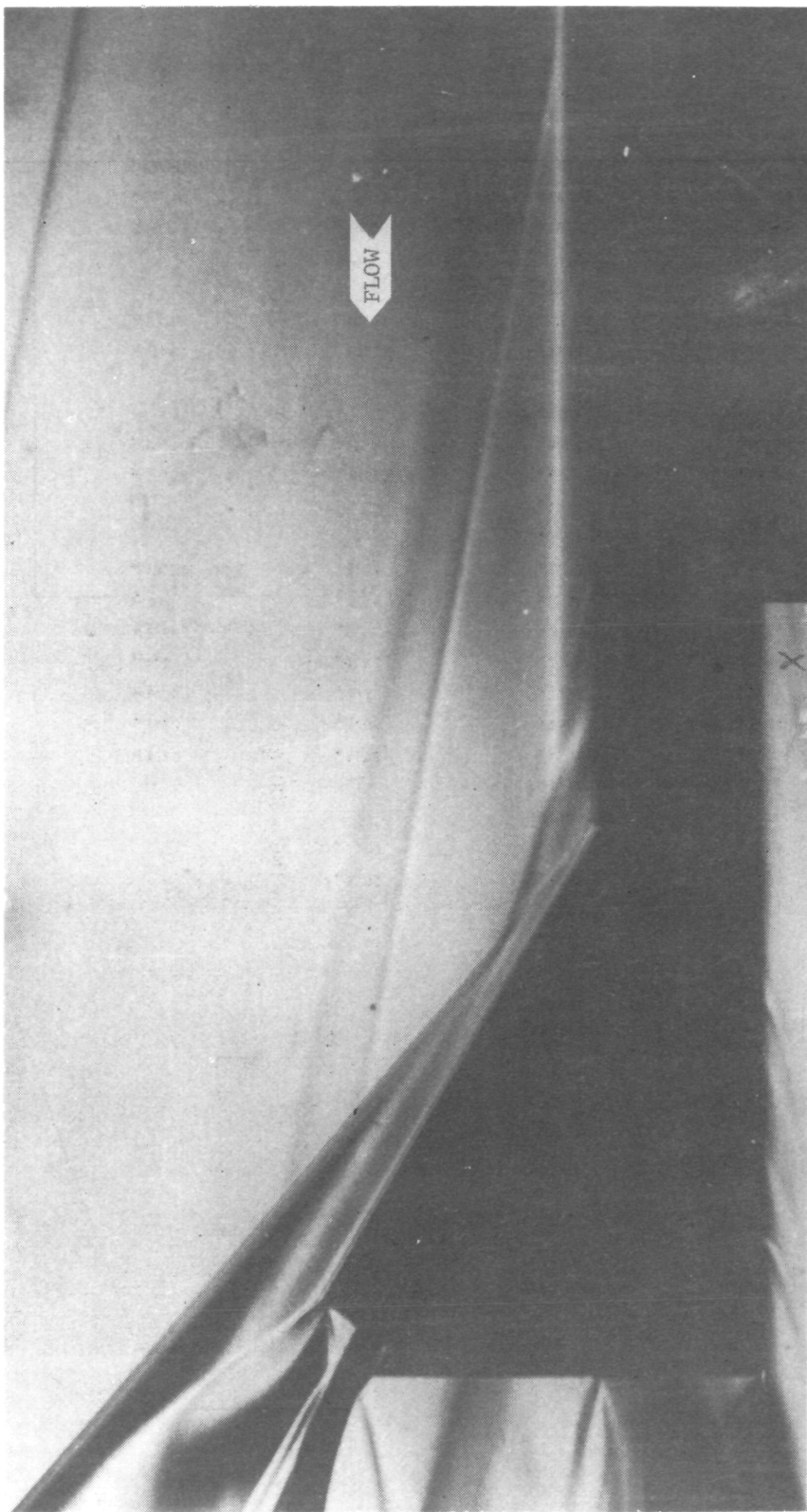
L-77-134

Figure 83.- Frame from surface-oil-flow motion picture for
 $\Lambda = 70^\circ$ and $\epsilon = 30^\circ$.



L-77-135

Figure 84.- Schlieren flow photograph for $\Lambda = 70^\circ$ and $\epsilon = 30^\circ$.



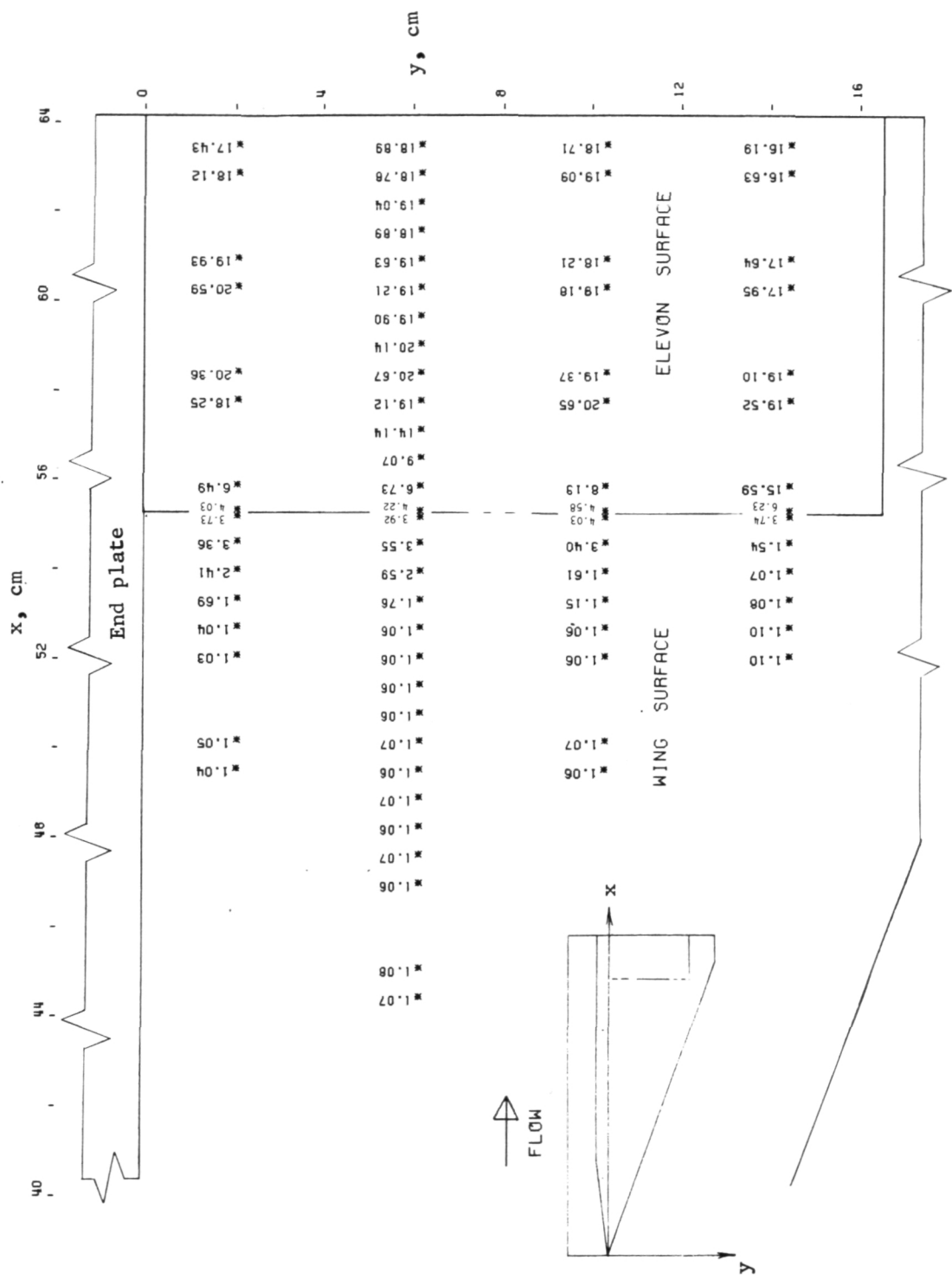
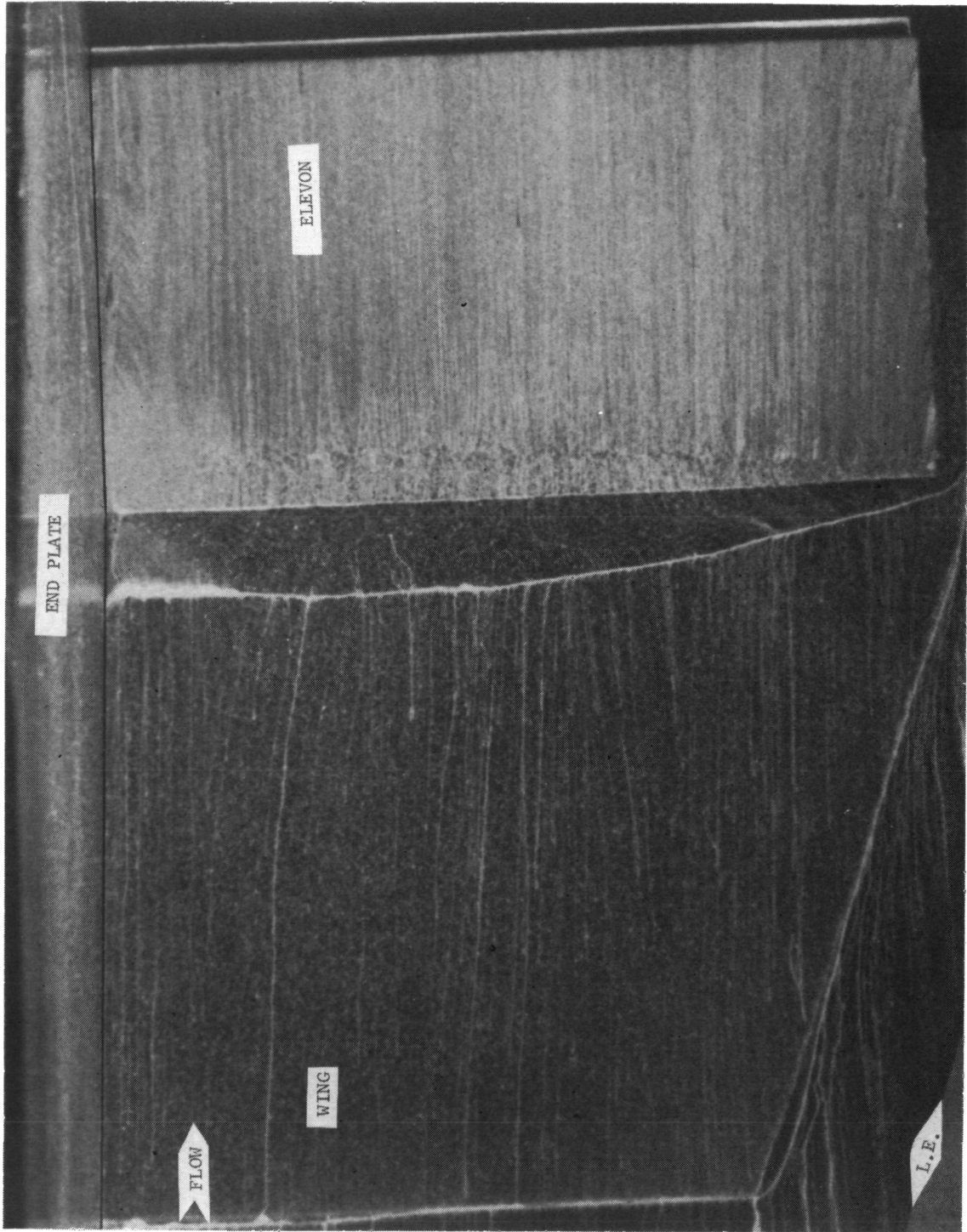


Figure 85.- Pressure-ratio (P) distribution on wing and elevon surfaces for $\Lambda = 70^\circ$, $\epsilon = 30^\circ$, and end plate attached.



L-77-136

Figure 86.- Frame from surface-oil-flow motion picture for $\Lambda = 70^\circ$,
 $\epsilon = 30^\circ$, and end plate attached.

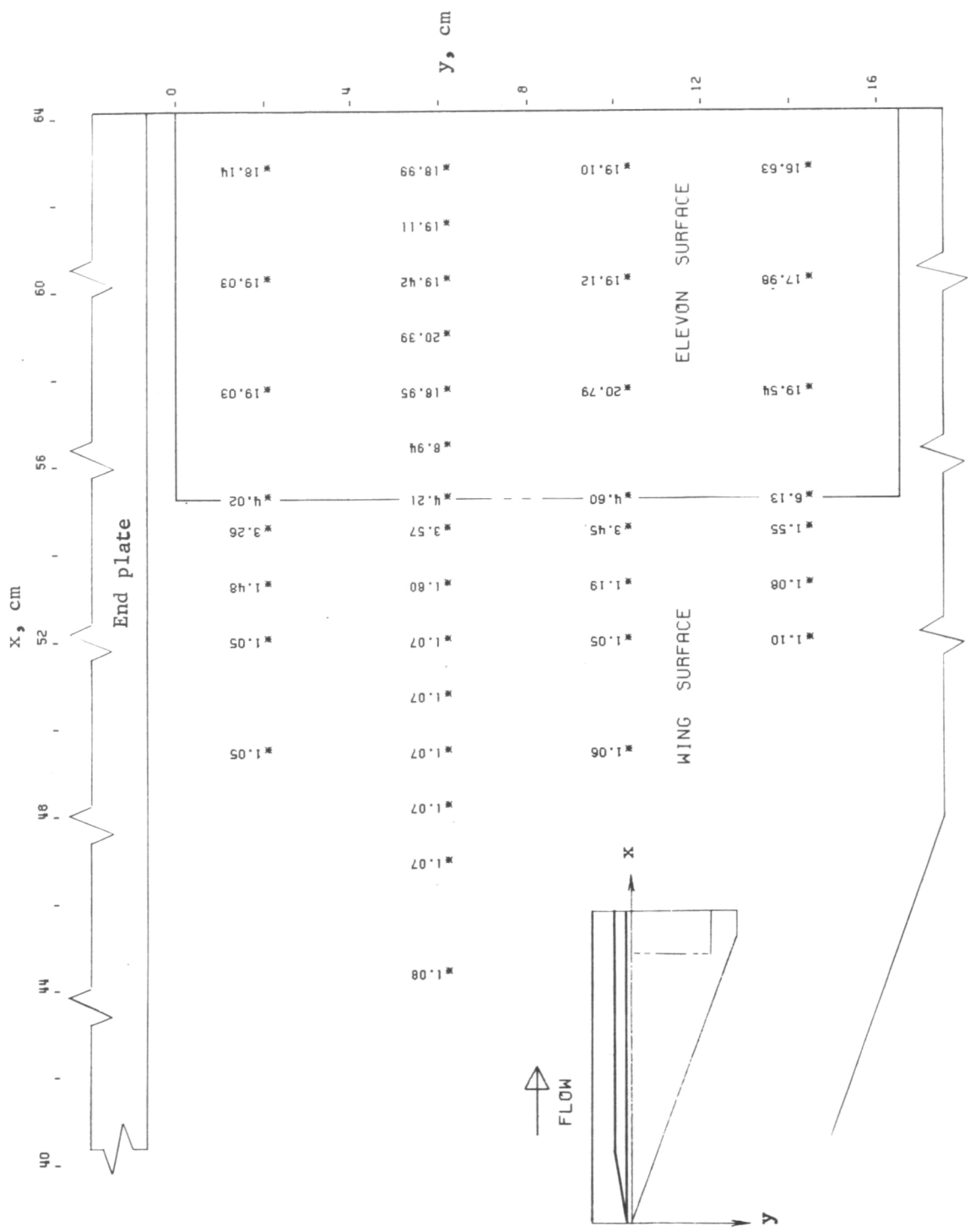


Figure 87.— Pressure-ratio (P) distribution on wing and elevon surfaces for $\Lambda = 70^\circ$, $\epsilon = 30^\circ$, and end plate attached 0.64 cm away from inboard edge of elevon.

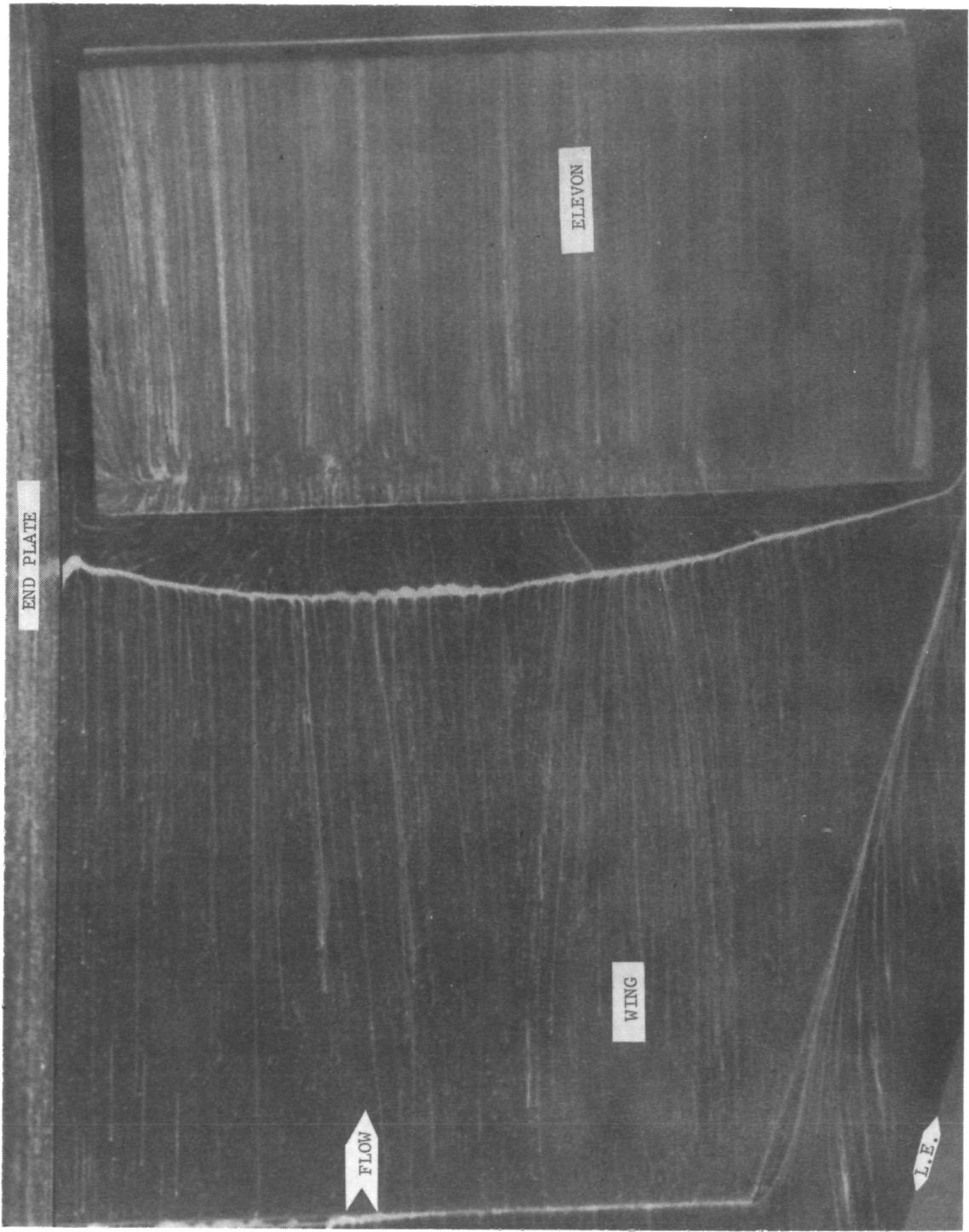


Figure 88.- Frame from surface-oil-flow motion picture for $\Lambda = 70^\circ$, $\epsilon = 30^\circ$, and end plate attached with 0.64-cm gap between end plate and elevon. L-77-137

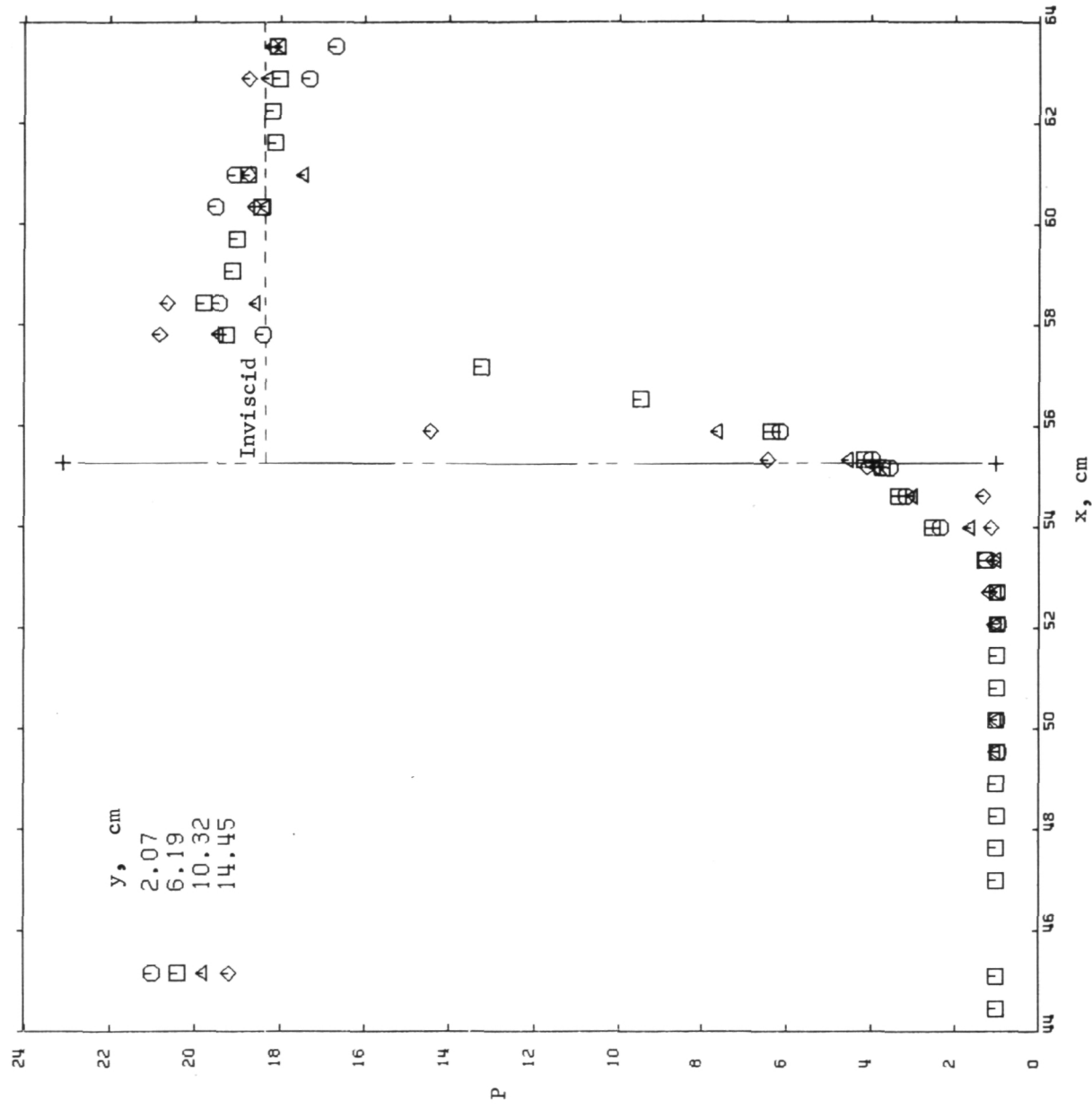


Figure 89.- Streamwise pressure-ratio distributions on wing and elevon surfaces for $\Lambda = 70^\circ$, $\epsilon = 30^\circ$, end plate attached, and tip plate attached.

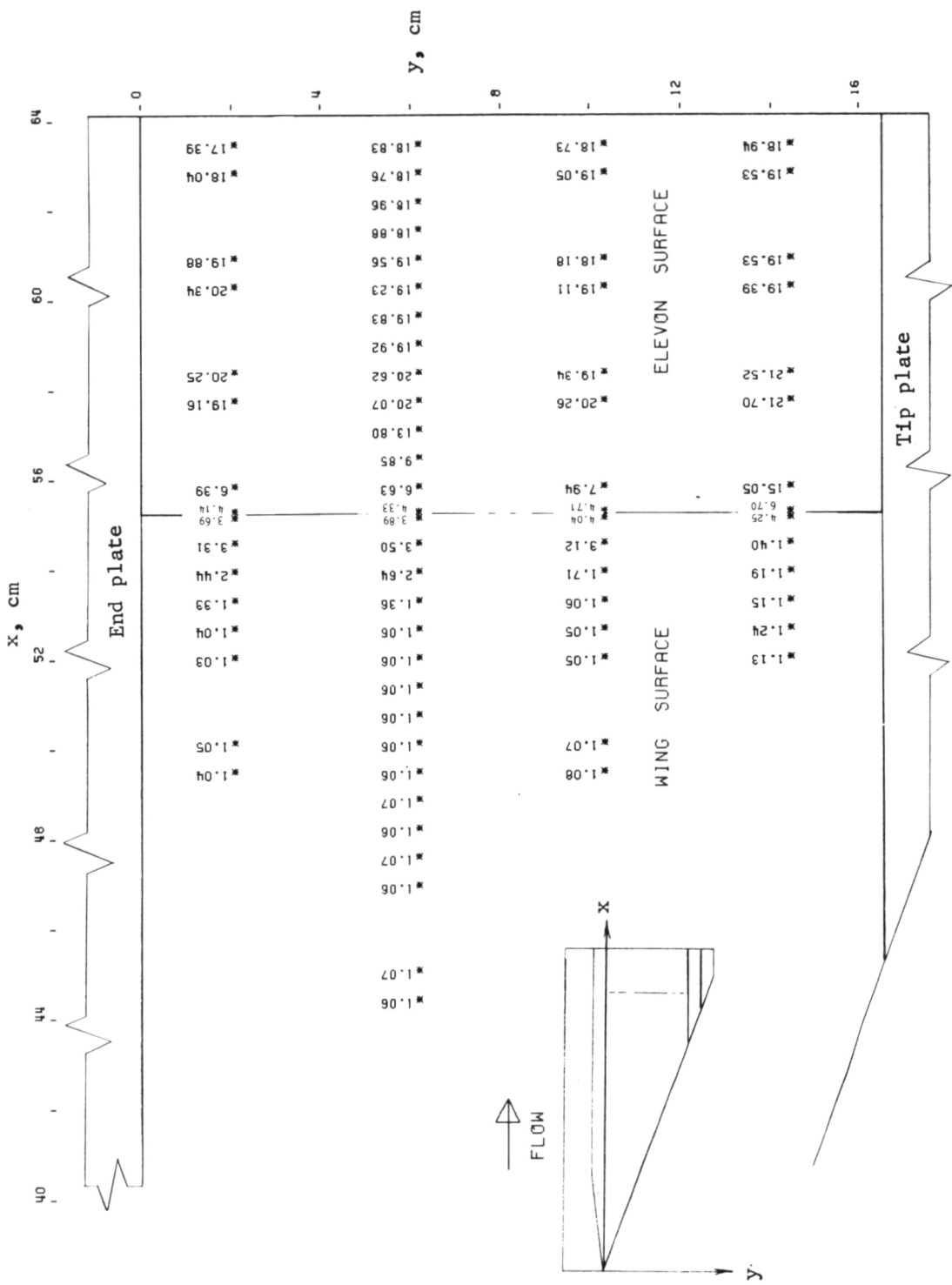


Figure 90.—Pressure-ratio (P) distribution on wing and elevon surfaces for $\Lambda = 70^\circ$, $\epsilon = 30^\circ$, end plate attached, and tip plate attached.

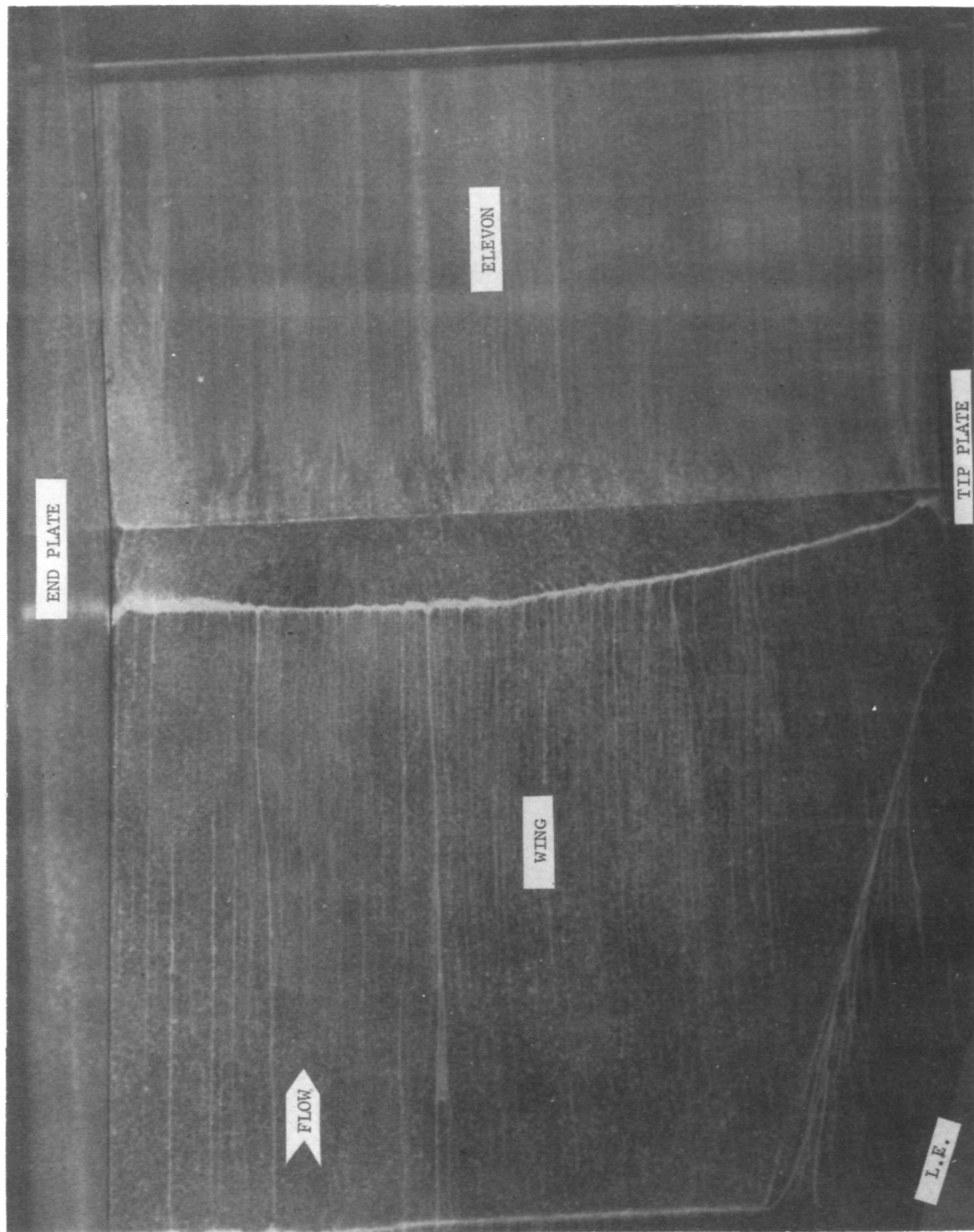


Figure 91.- Frame from surface-oil-flow motion picture for $\Lambda = 70^\circ$,
 $\epsilon = 30^\circ$, end plate attached, and tip plate attached.
L-77-138

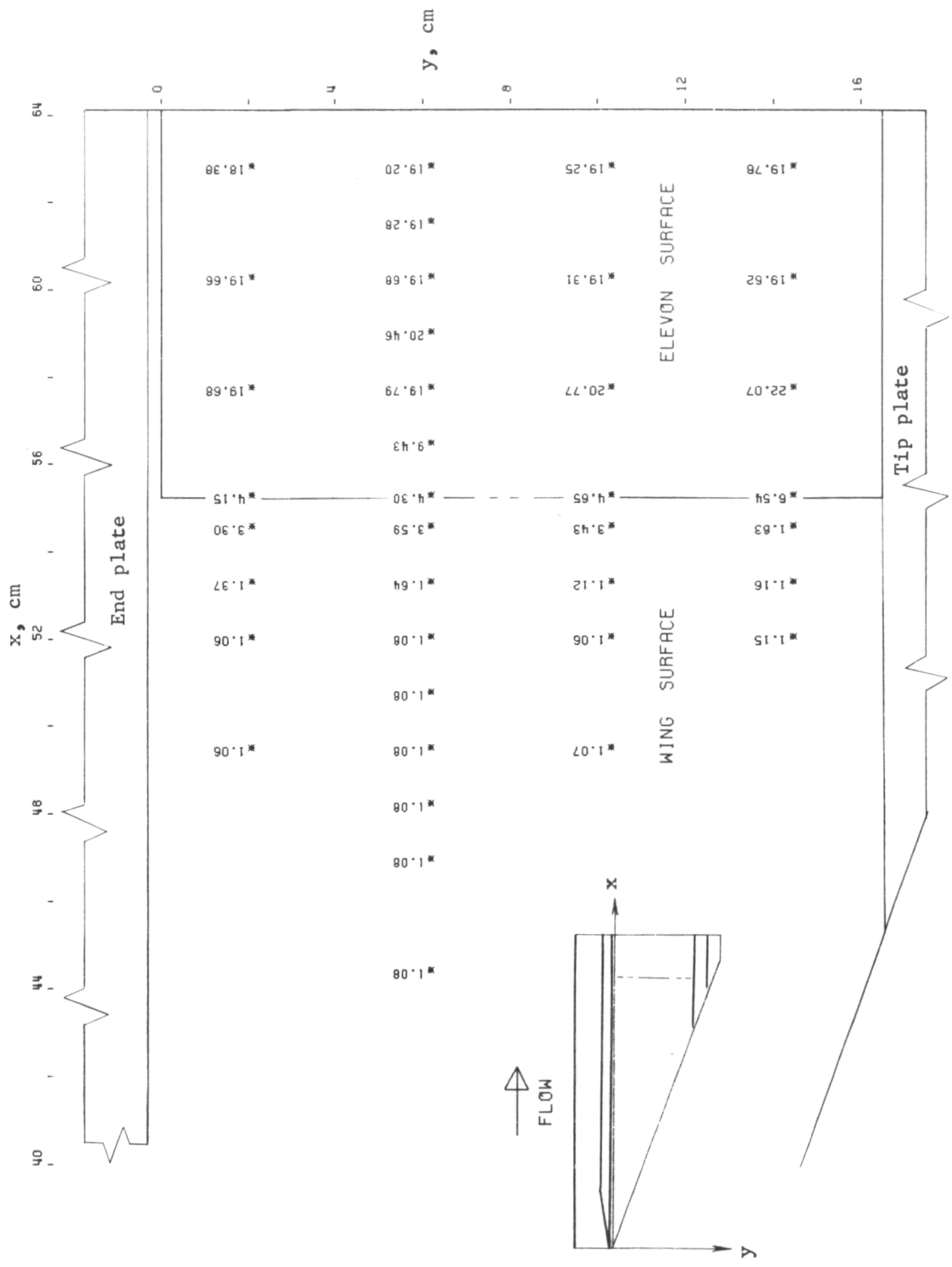


Figure 92.— Pressure-ratio (P) distribution on wing and elevon surfaces for $\Lambda = 70^\circ$, $\epsilon = 30^\circ$, end plate attached 0.32 cm away from inboard edge of elevon, and tip plate attached.

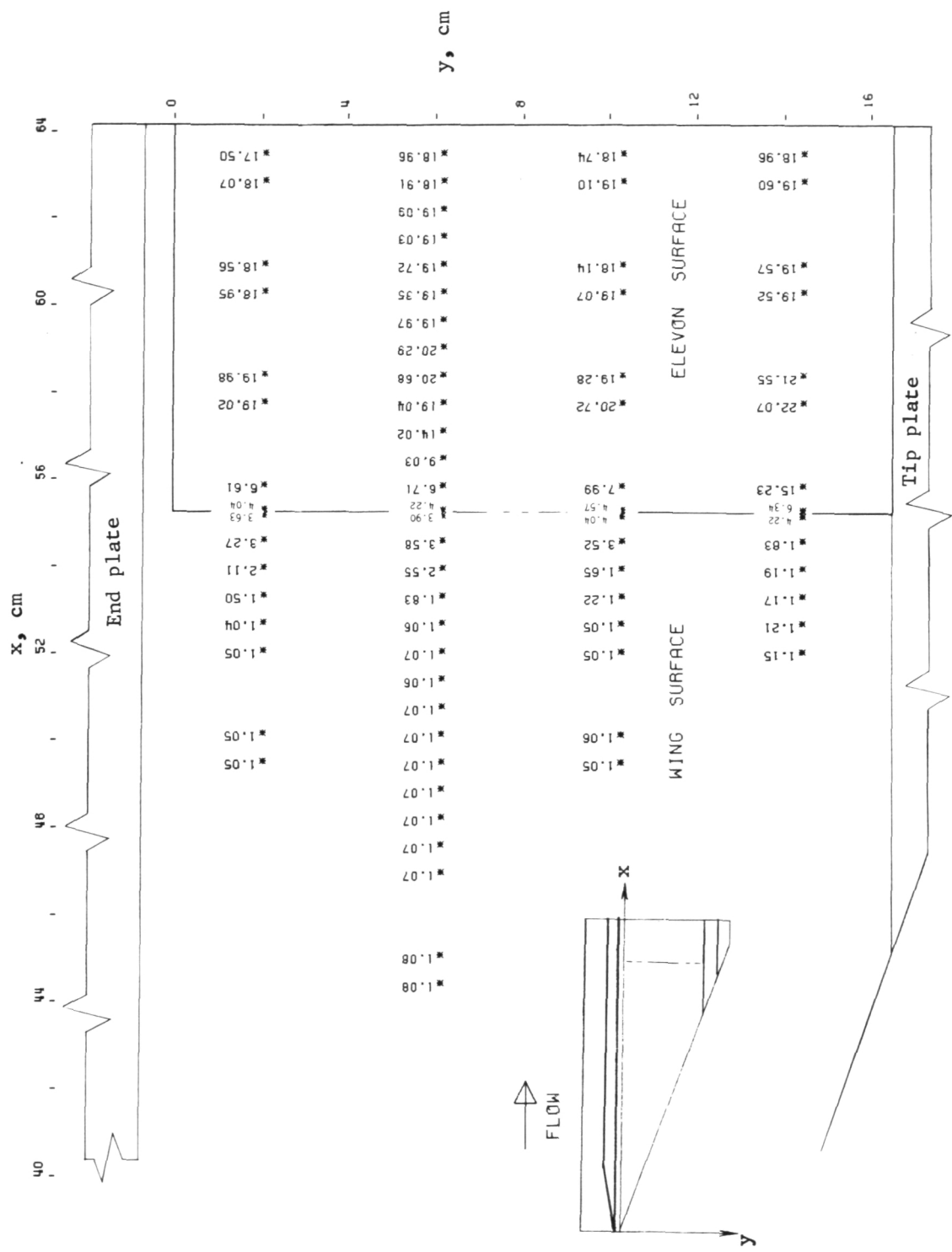


Figure 93.— Pressure-ratio (P) distribution on wing and elevon surfaces for $\Lambda = 70^\circ$, $\epsilon = 30^\circ$, end plate attached 0.64 cm away from inboard edge of elevon, and tip plate attached.



Figure 94.— Pressure-ratio (P) distribution on wing and elevon surfaces for $\Lambda = 70^\circ$, $\epsilon = 30^\circ$, end plate attached 0.95 cm away from inboard edge of elevon, and tip plate attached.



Figure 95.— Pressure-ratio (P) distribution on wing and elevon surfaces for $\Lambda = 70^\circ$, $\epsilon = 30^\circ$, end plate attached 1.27 cm away from inboard edge of elevon, and tip plate attached.

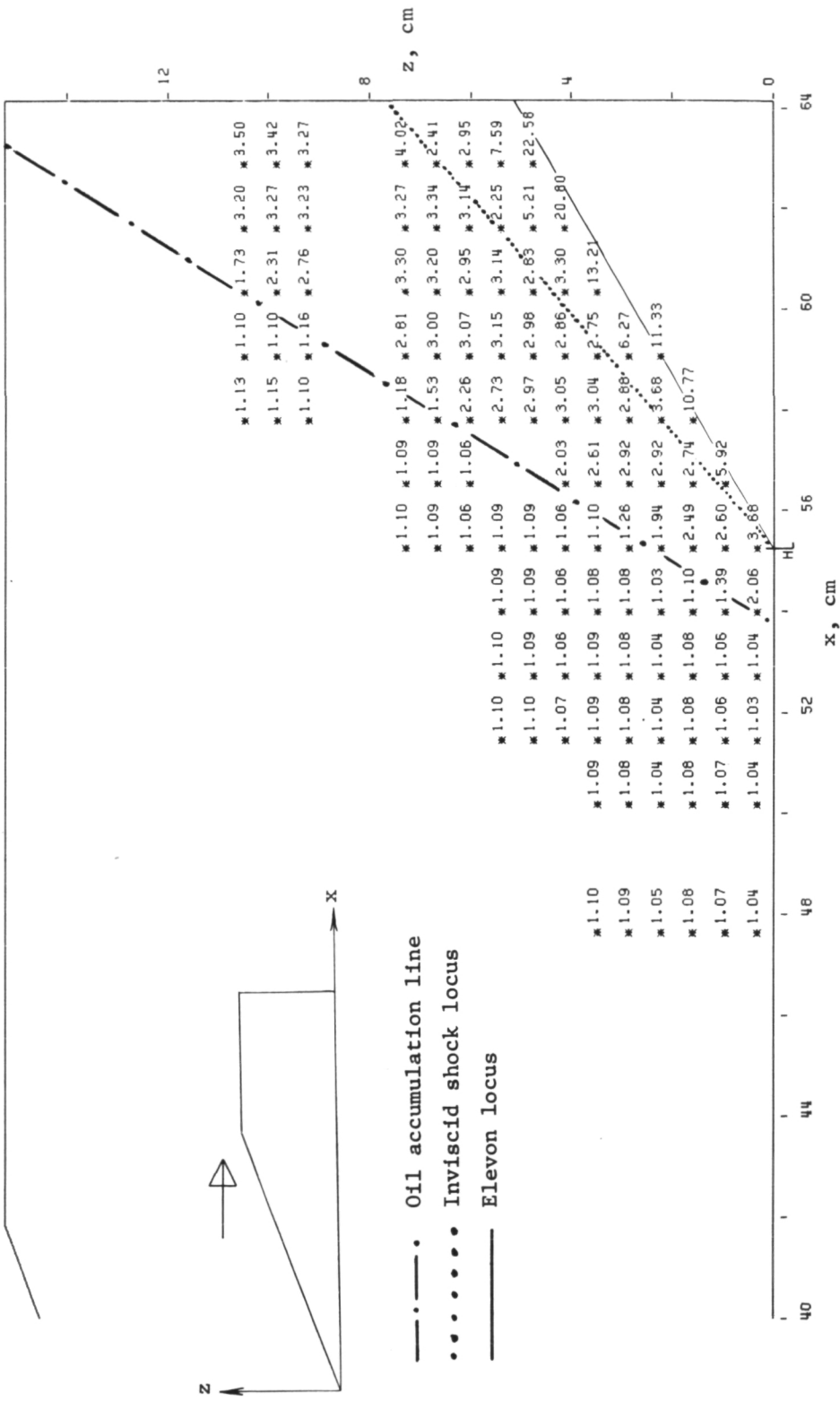
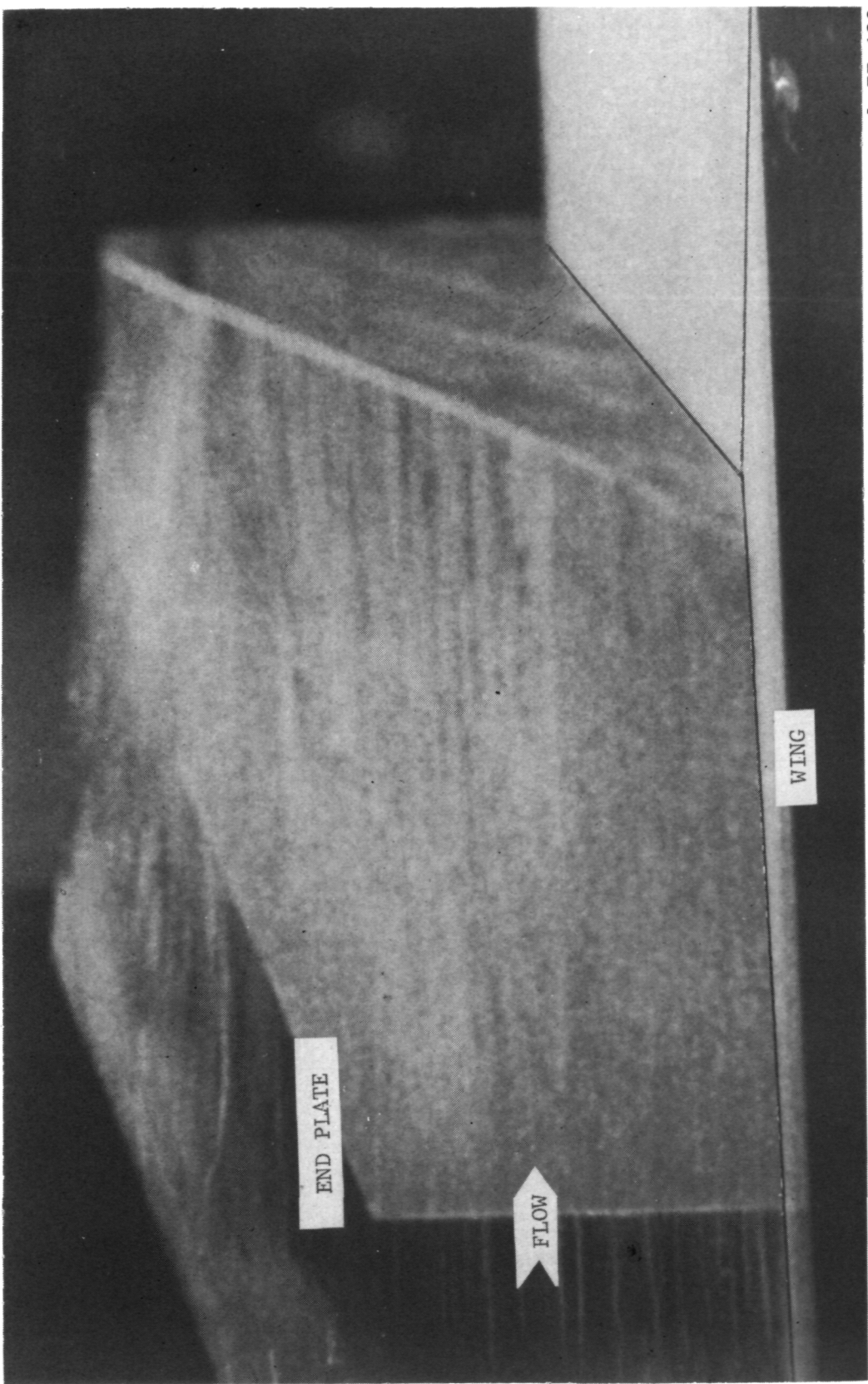


Figure 96.— Pressure-ratio (P) distribution on end-plate surface for $\Lambda = 70^\circ$ and $\epsilon = 30^\circ$.

L-77-139

Figure 97.- Frame from surface-oil-flow motion picture for $\Lambda = 70^\circ$,
 $\epsilon = 30^\circ$, and end plate attached.



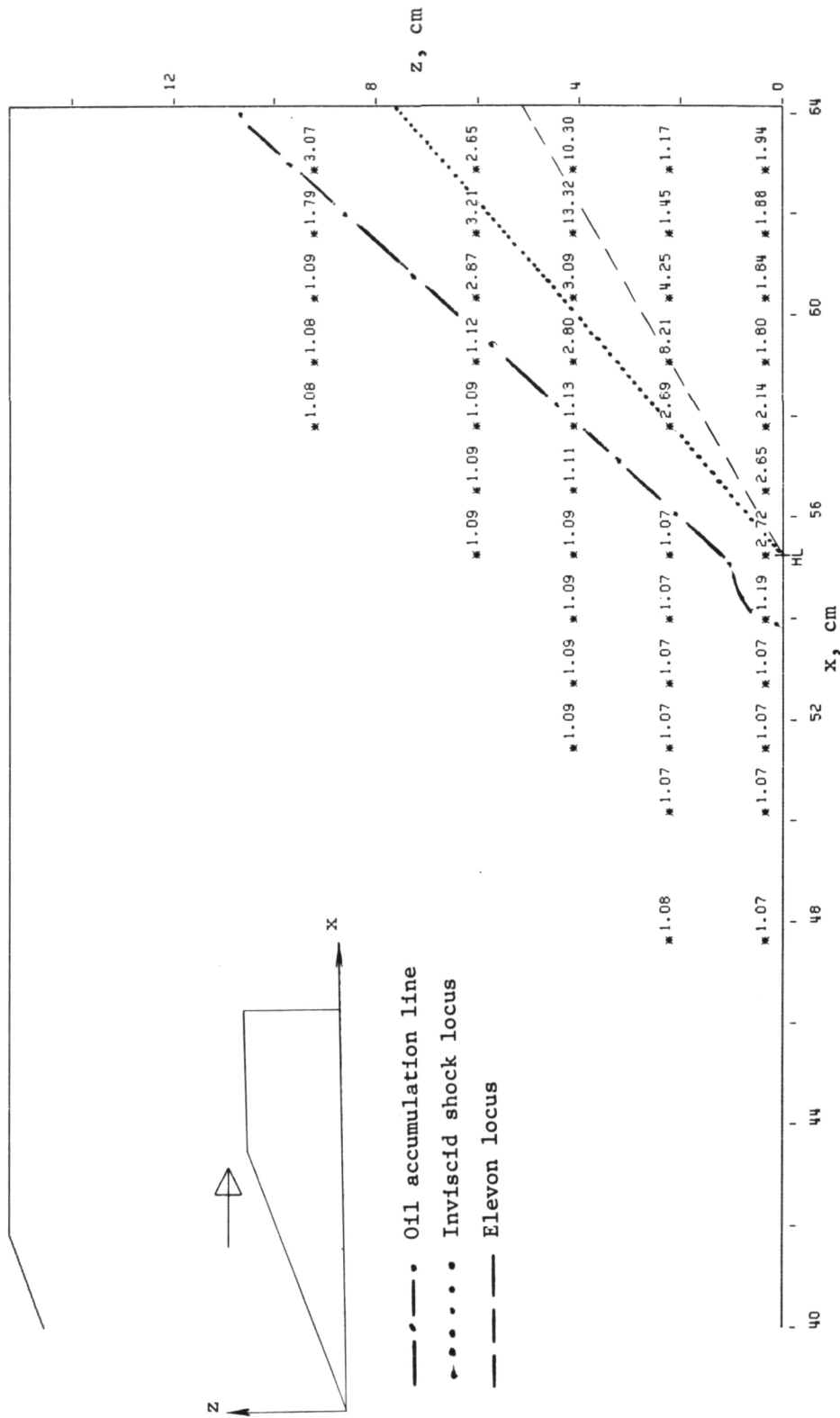


Figure 98.- Pressure-ratio (P) distribution on end-plate surface for $\Lambda = 70^\circ$, $\epsilon = 30^\circ$, and 0.64-cm gap between end plate and elevon.

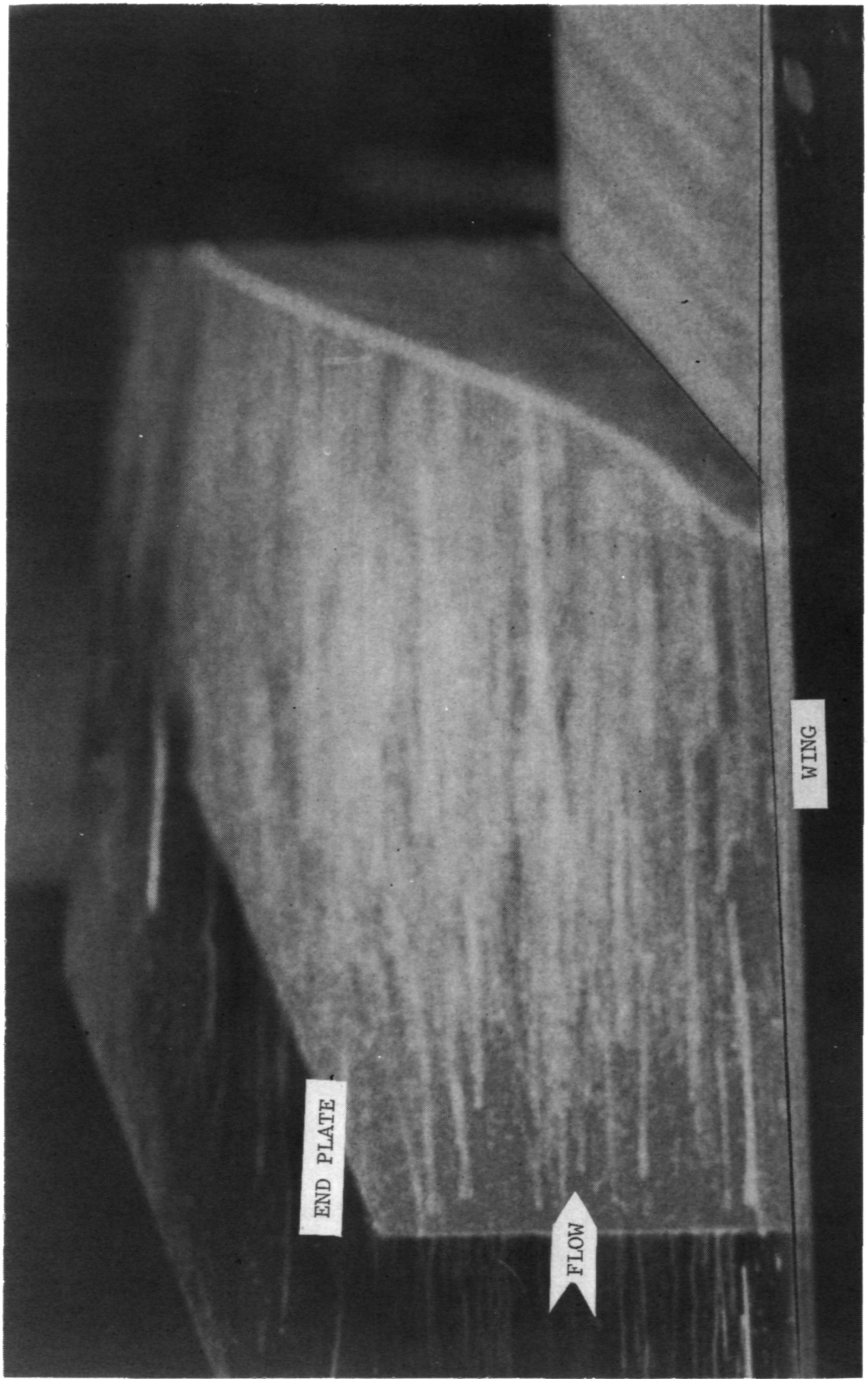


Figure 99.— Frame from surface-oil-flow motion picture for $\Lambda = 70^\circ$, $\epsilon = 30^\circ$, and end plate attached with 0.64-cm gap between end plate and elevon. L-77-140

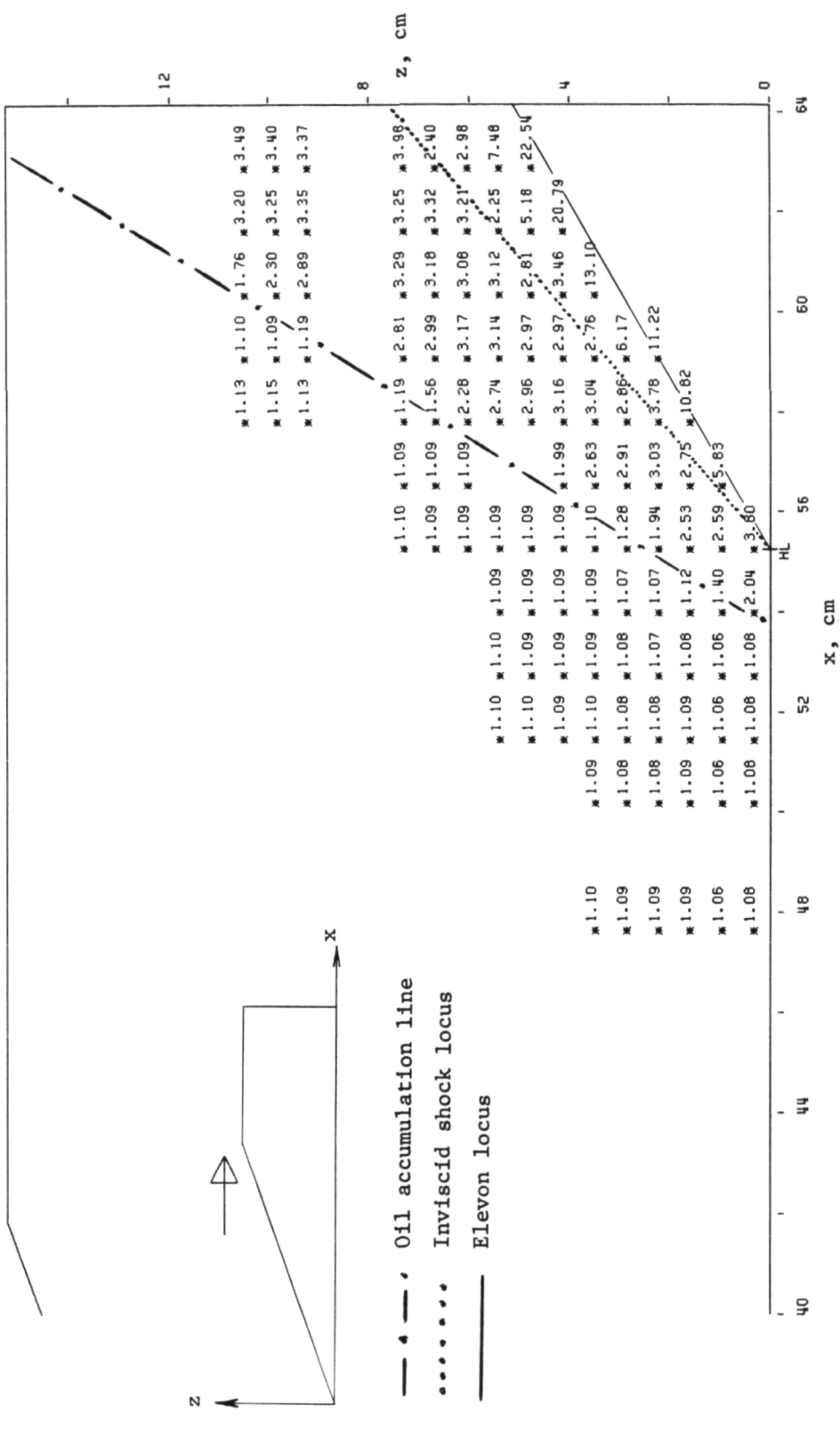
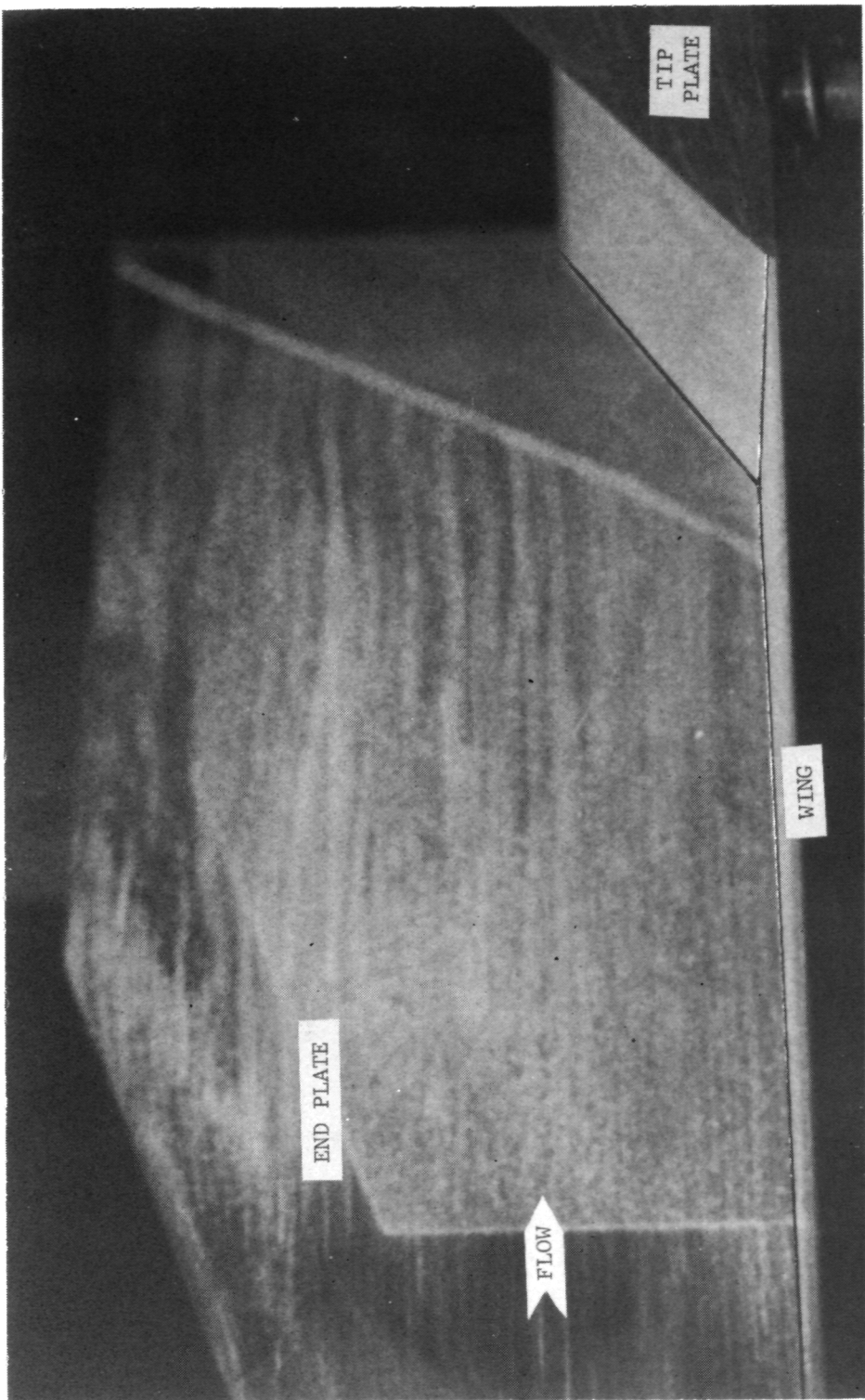


Figure 100.— Pressure-ratio (P) distribution on end-plate surface for $\Lambda = 70^\circ$, $\epsilon = 30^\circ$, and tip plate attached.

L-77-141

Figure 101.- Frame from surface-oil-flow motion picture for $\Lambda = 70^\circ$, $\epsilon = 30^\circ$, end plate attached, and tip plate attached.



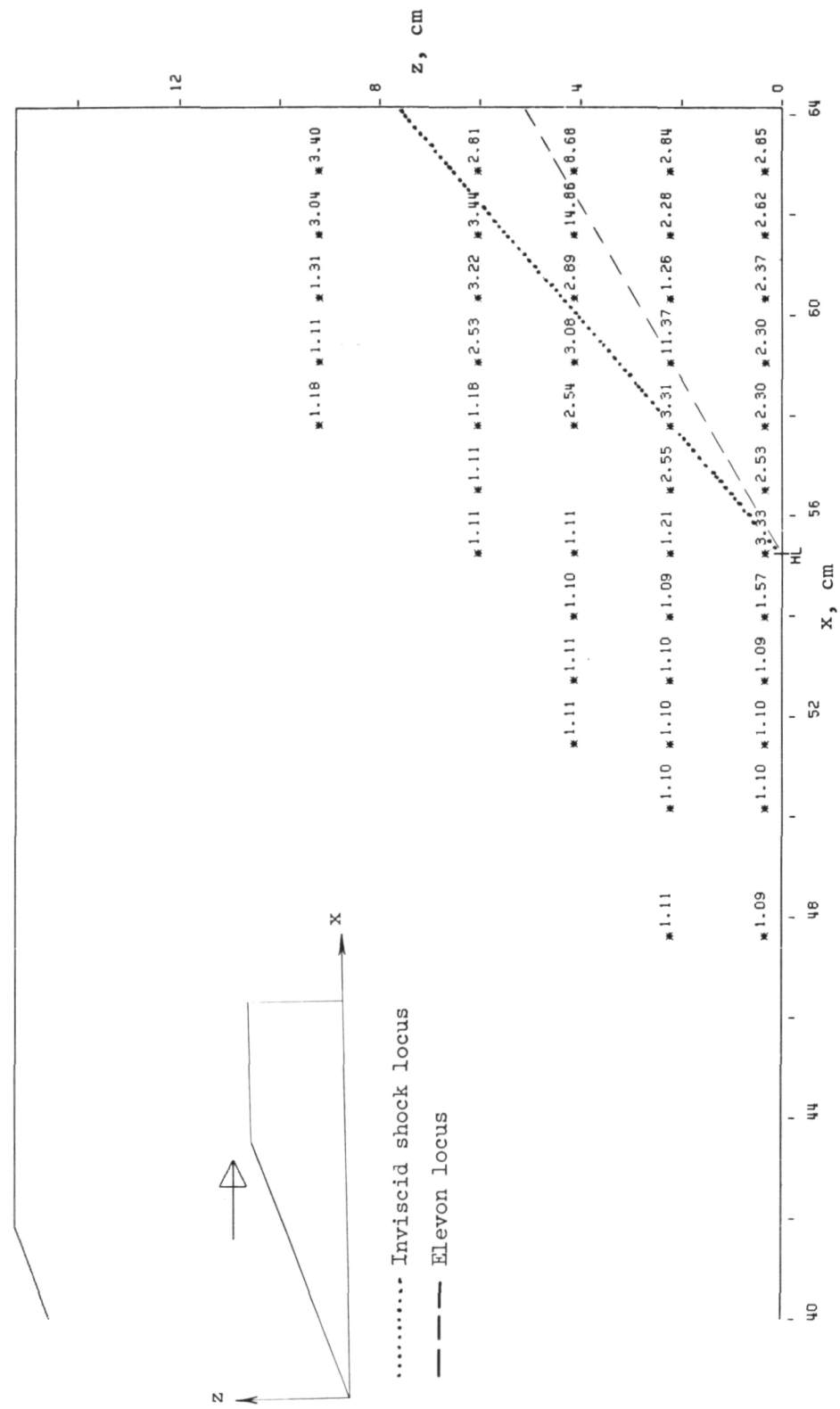


Figure 102.— Pressure-ratio (P) distribution on end-plate surface for $\Lambda = 70^\circ$, $\epsilon = 30^\circ$, 0.32-cm gap between end plate and elevon, and tip plate attached.

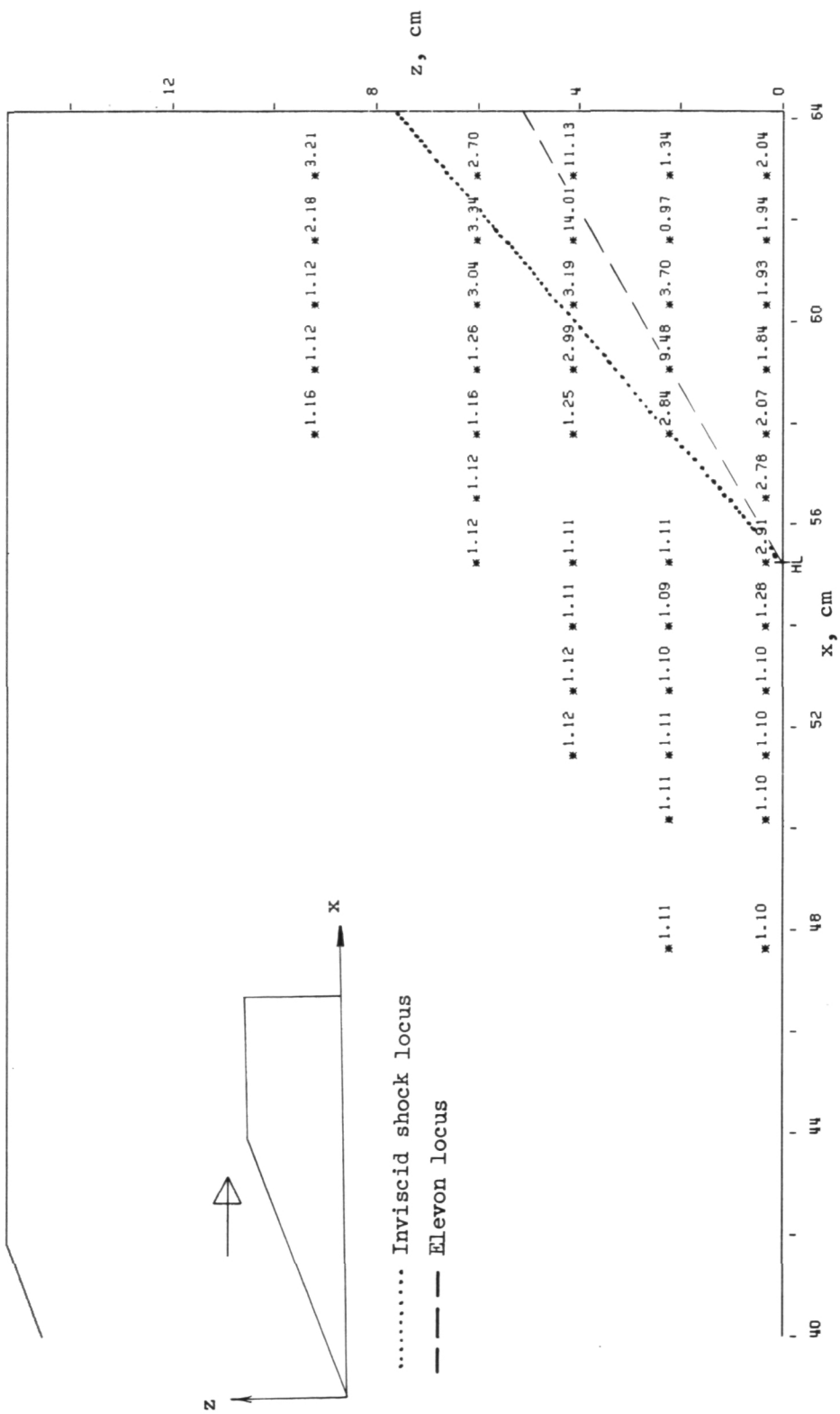


Figure 103.— Pressure-ratio (P) distribution on end-plate surface for $\Lambda = 70^\circ$, $\epsilon = 30^\circ$, 0.64-cm gap between end plate elevon, and tip plate attached.

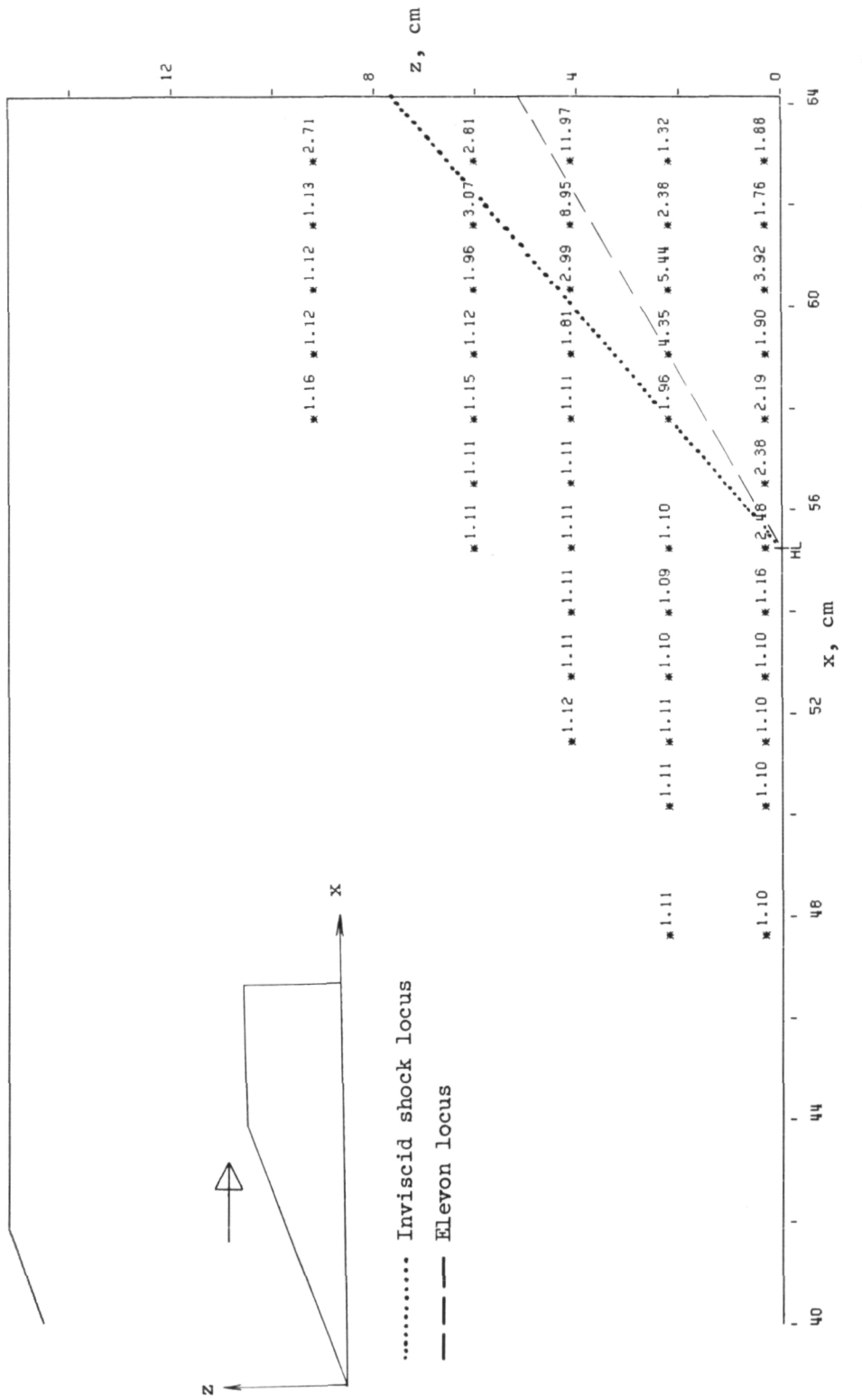


Figure 104.— Pressure-ratio (P) distribution on end-plate surface for $\Lambda = 70^\circ$, $\epsilon = 30^\circ$, 0.95-cm gap between end plate and elevon, and tip plate attached.

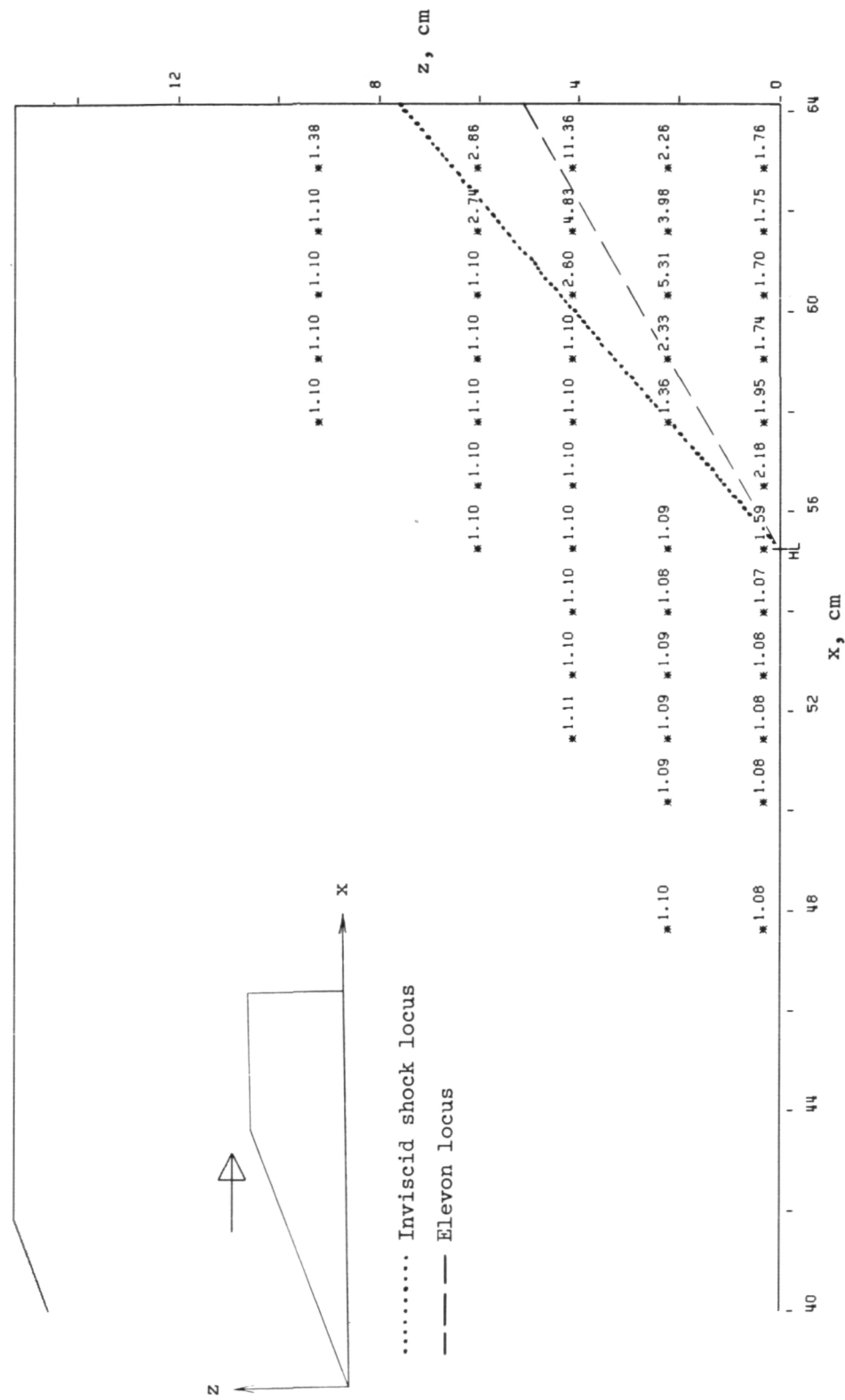


Figure 105.— Pressure-ratio (P) distribution on end-plate surface for $\Lambda = 70^\circ$, $\epsilon = 30^\circ$, 1.27-cm gap between end plate and elevon, and tip plate attached.

NATIONAL AERONAUTICS AND SPACE ADMINISTRATION
WASHINGTON, D.C. 20546

OFFICIAL BUSINESS
PENALTY FOR PRIVATE USE \$300

SPECIAL FOURTH-CLASS RATE
BOOK

POSTAGE AND FEES PAID
NATIONAL AERONAUTICS AND
SPACE ADMINISTRATION
451



POSTMASTER : If Undeliverable (Section 158
Postal Manual) Do Not Return

"The aeronautical and space activities of the United States shall be conducted so as to contribute . . . to the expansion of human knowledge of phenomena in the atmosphere and space. The Administration shall provide for the widest practicable and appropriate dissemination of information concerning its activities and the results thereof."

—NATIONAL AERONAUTICS AND SPACE ACT OF 1958

NASA SCIENTIFIC AND TECHNICAL PUBLICATIONS

TECHNICAL REPORTS: Scientific and technical information considered important, complete, and a lasting contribution to existing knowledge.

TECHNICAL NOTES: Information less broad in scope but nevertheless of importance as a contribution to existing knowledge.

TECHNICAL MEMORANDUMS: Information receiving limited distribution because of preliminary data, security classification, or other reasons. Also includes conference proceedings with either limited or unlimited distribution.

CONTRACTOR REPORTS: Scientific and technical information generated under a NASA contract or grant and considered an important contribution to existing knowledge.

TECHNICAL TRANSLATIONS: Information published in a foreign language considered to merit NASA distribution in English.

SPECIAL PUBLICATIONS: Information derived from or of value to NASA activities. Publications include final reports of major projects, monographs, data compilations, handbooks, sourcebooks, and special bibliographies.

TECHNOLOGY UTILIZATION PUBLICATIONS: Information on technology used by NASA that may be of particular interest in commercial and other non-aerospace applications. Publications include Tech Briefs, Technology Utilization Reports and Technology Surveys.

Details on the availability of these publications may be obtained from:

SCIENTIFIC AND TECHNICAL INFORMATION OFFICE

NATIONAL AERONAUTICS AND SPACE ADMINISTRATION

Washington, D.C. 20546